Mass Transport in Ag-alloyed PbTe Compounds for Thermoelectric Applications

Meir-Haim Dahan

Mass Transport in Ag-alloyed PbTe Compounds for Thermoelectric Applications

Research Thesis In Partial Fulfillment of the Requirements for the Degree of Master of Science in Materials Engineering

Meir-Haim Dahan

Submitted to the Senate of
the Technion - Israel Institute of Technology

Tamuz 5780, July 2020

This research was performed under the supervision of Assoc. Prof. Yaron Amouyal at the Department of Materials Science and Engineering, Technion – Israel Institute of Technology.

I would like to express my gratitude to the generous financial support from the Irwin and Joan Jacobs Graduate School and the Department of Materials Science and Engineering at the Technion. Support from the Asher Space Research Institute (ASRI) and the Russell Berrie Nanotechnology Institute (RBNI) at the Technion is acknowledged, as well.

I would like to thank the current and the former fellow group members for their help and advice: Amram Azulay, Gil Solomon, Dr. Chhatrasal Gayner, Dr. Yuriy Natanzon, Jacob Rubin, Aleksandra Uzhanskaia, Ohad Shkury, Michal Keret-Kleiner, Keren Stein-Kassuto, Dr. Andrei Baranovskiy, Ariel Sheskin, Yoav H. Jurkevitch and Shim'on Sukholuski.

I would like to express my gratitude to Dr. Maria Koifman for her kind helping with the XRD analysis.

Finally, I would like to thank my wife, Moran Dahan, for the support and concern. Words will only diminish the help I received.

1 Table of Contents

List of figures

List of figures

List of figures

List of figures

List of figures

List of symbols and abbreviations

APT	Atom probe tomography
DFT	Density functional theory
ELF	Electron localization function
EPMA	Electron probe microanalysis
GGA	Generalized gradient approximation
GofF	Goodness of fitting
HT	High temperature
HTST	Harmonic transition state theory
HP	Hot-press
K-S	Kohn-Sham
LT	Low temperature
MFP	Mean free path
PAW	Projected augmented wave
PBEsol	Perdew-Burke-Ernzerhof-solid
PF	Power factor
QQ-HTST	Quasi-quantum harmonic transition state theory
RTG	Radioisotope thermoelectric generator
SEM	Scanning electron microscopy
SOC	Spin-orbit coupling
TE	Thermoelectric
TEG	Thermoelectric generator
TEM	Transmission electron microscopy
TST	Transition state theory
VASP	Vienna ab-initio software package
WSS	Weighted sum of squares
XRD	X-ray diffraction
zT	Thermoelectric figure-of-merit

α	Thermal diffusivity
D	Pre-exponential diffusion coefficient
φ	electron orbitals
γ	Surface energy
κ	Thermal conductivity
μ	Chemical potential
ρ	Density
σ	Electrical conductivity
ψ	Wavefunction
a	Lattice parameter
C_p	Constant pressure heat capacity ($\mathrm{J \cdot kg^{-1} \cdot K^{-1}}$)
d	Inter-atomic plane distance
E	Energy
E_g	Bandgap
G	Gibbs free energy
n	Electron charge density
T	Temperature
S	Seebeck coefficient
V	Unit-cell volume
e	Electron charge
$\hbar$	Reduced Planck constant
k_B	Boltzmann constant

<u>Subscripts</u>

e	Electron
p	phonon
l	lattice
M	Migration

XC	Exchange-correlation
TS	Transition state
0	Initial state
*	Critical value

2 Abstract

Thermoelectric (TE) devices attract extensive interest due to their ability to convert heat into electrical energy. Among all TE properties, the thermal conductivity (κ) determines the conversion efficiency of TE devices, and can be described as a sum of two components, namely the lattice and electronic contributions, defined as κ_p and κ_e, respectively. Formation of second phases, as well as other nanometer-size features, plays a significant role in determination of the TE transport properties due to chiefly reduction of κ_p by phonon scattering, as well as variation of the Seebeck coefficient, S, and the electrical conductivity, σ. PbTe-based compounds establish an important class of TE materials due to their high melting point (1190 K) and relatively high zT at the mid-temperature range (600-800 K). The Pb-Te-Ag system is of prime interest due to its potential of forming Ag-rich precipitates dispersed in the PbTe-matrix. Investigation of the microstructure evolution of this system enabled us to predict the applicability regime of this system in service temperatures, and this involves both thermodynamic and kinetic aspects.

Herein, we apply first-principles calculations to evaluate the diffusion coefficients of silver atoms in a lead-telluride matrix. We determine both the activation energy for diffusion and the pre-exponential diffusion coefficient for the interstitial mechanism using the *transition state theory* (TST) to be $1.08 \cdot 10^{-5}$ $cm^2 \cdot s^{-1}$ and 52.9 $kJ \cdot mole^{-1}$, respectively. These values are compared with experimental data, and indicate that the characteristic times required for significant microstructure evolution in these compounds can be as short as 15 min. under service temperature (380 °C).

We synthesize materials applying vacuum melting and homogenization, followed by milling. We preform homogenization at 700 °C and aging heat treatments at 380 °C for duration up to 100 h to control nucleation and growth of Ag-rich phases. We track the microstructure evolution of Ag-doped PbTe alloys for different aging times at 380 °C using x-ray diffraction (XRD), and investigate the microstructure evolution rate, showing significant changes taking place during ca. 1 h.

Some of the powders are hot-pressed to create bulk samples. In-situ heating experiments were performed to measure the thermal conductivity using laser flash analysis (LFA) technique, and electronic transport coefficients employing a dedicated

four-point probe system equipped with micro heating segments. We found that in the first few hours of the in-situ experiments, there were rapid changes for all samples in both electronic properties (Seebeck coefficient and electrical conductivity) and thermal conductivity.

This study provides us with predictive information on the thermal stability of PbTe-based compounds, thereby evaluating the kinetics of phase transformations in these compounds, and is useful to further improve our ability to control nucleation and growth of Ag-rich precipitates in PbTe.

3 Introduction

The emerging global need for energy production, conservation, and management has intensified interest in more effective renewable sources, including solar, wind, biomass, and others. Another potential source of renewable power is electricity from heat sources using TE materials. TE generators (TEGs) are solid-state devices that directly convert thermal energy into electrical energy and vice versa. This process is based on the Seebeck effect, which is the appearance of electrical voltage due to temperature gradient across a material.

Application of TE devices in daily life strongly depends on their thermodynamic conversion efficiency, which is determined by the TE figure of merit (zT). Better TE performance, which means an increased zT, is manifested in a large Seebeck coefficient, high electrical conductivity, and low thermal conductivity. These three requirements are usually contradictory, which makes the development of TE materials a grand challenge from the point of view of material science. Furthermore, these properties are highly sensitive to the finest features of microstructure.

The PbTe compound and its derivatives are an important class of TE materials due to their high melting point (1190K), low relative zT and relatively low-temperature applications (600-800K). The crystallographic structure of PbTe is rocksalt (NaCl structure). The Pb-Te-Ag system features an advantage due to its potential of forming Ag_2Te precipitates, which are expected to serve as phonon scattering centers in the PbTe matrix, thus reducing lattice thermal conductivity (κ_p). A big advantage is the fact that the growth of Ag_2Te inside the PbTe matrix can be controlled according to

the equilibrium phase diagram of the pseudo-binary PbTe– Ag_2Te system. There are many reports showing that the maximum zT values for doped PbTe can exceed 1.5.[1]

The present study focuses on the Ag-doped PbTe system, which has the potential of forming Ag-rich precipitates dispersed in a PbTe-based solid solution. The Ag_2Te precipitates are expected to serve as phonon-scattering centers, thereby reducing lattice thermal conductivity and increasing its zT value. The degradation rate of a TE power generator based on such compounds led us to investigate in this work the implications for thermal stability and performance degradation of TE devices, based on nanostructured compounds. The goals of this research are to quantitatively evaluate diffusion coefficients of Ag-atoms in PbTe for the temperature range of 300 through 800 K and to estimate the kinetics of Ag_2Te precipitates evolution, applying computational and experimental methods. This will help us determine the effects on TE transport coefficients. The present research is based on previous M.Sc. studies conducted by Mr. Ariel Sheskin and Mr. Tom Grossfeld at the *Thermoelectric Materials Research Group*, Technion, and introduces further progress.

4 Literature review

4.1 Basics of Thermoelectricity

4.1.1 The Thermoelectric Effect

In 1822 T. Seebeck observed that a circuit made from two dissimilar metals with junctions at different temperatures deflects a compass magnet. [2] Today, the Seebeck effect is realized as generation of open-circuit electric potential (voltage) due to temperature difference; it drives an electric current in a closed circuit.

During the 19th century, other TE effects were observed. In 1834, production of heat flux by electric current was observed by J. Peltier, which was later denoted as the Peltier effect. In 1851, Thomson detected the release or absorption of heat when an electric current passes through a circuit composed of a single material subjected to temperature gradient; this effect is known as the Thomson effect. [3,4]

In 1909, E. Altenkirch[5,6] was the first to use the constant property model to derive the maximum efficiency of a TE generator (TEG), and later (1911) he described

the performance of a TE cooler. A significant progress was made during the 1930's, since the discovery of semiconducting materials, in which Seebeck coefficients greater than 100 μV/K were obtained. In 1949 A. Ioffe developed the modern theory of thermoelectricity using the concept of the '*figure of merit*' zT, by incorporating several parameters into a single parameter expressing the efficiency of TE devices. Ioffe was also one of the pioneers to employ doping to reduce lattice thermal conductivity by creating point defects.[7] The industrial applicability of TE materials is their ability to convert temperature difference into electricity and vice versa, as green energy conversion. Such materials can be utilized to convert waste heat into useful electricity, for example, in spacecrafts, in manufacturing industries, or in the automotive industry.

TEGs have become widely utilized for radioisotope power systems in space applications using radioisotope thermoelectric generators (RTGs).[8] For example, space exploration missions require safe, reliable, long-life power systems to provide electricity to spacecrafts with no need to replace batteries. A proven capable source of power is the RTG. RTGs are devices that generate electrical power by converting the

$(\boldsymbol{a})$ $(\boldsymbol{b})$

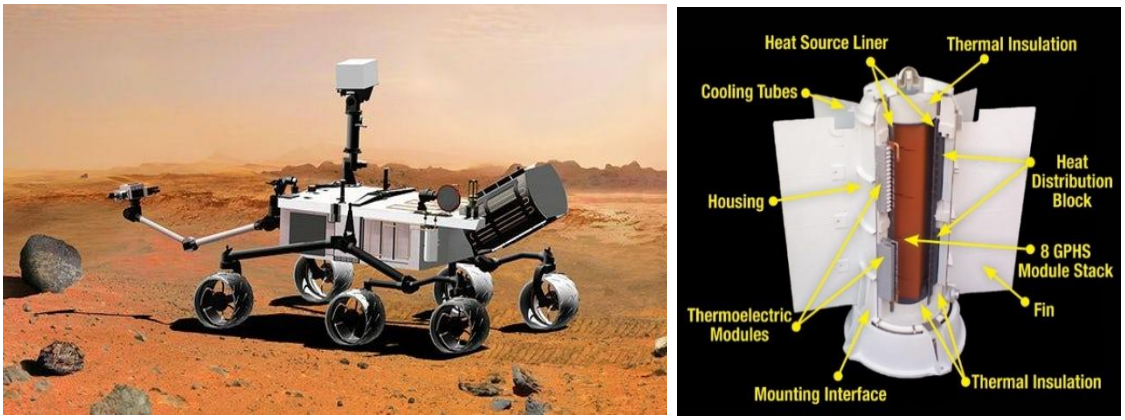

Figure 1 - (a). The Mars land rover, *Curiosity*, powered by a radioactive thermoelectric generator (RTG, the dark cylinder on rear). (b). A typical structure of an RTG.

heat released from the nuclear decay of radioactive isotopes (typically plutonium-238) into electricity using an adjacent TE.

RTGs have been successfully used to power several space missions; some of them have been operating for more than three decades in the inter-stellar space. [9] Historically, TE technology has only occupied niche areas for space applications.

Recent materials advances as well as the increasing awareness to energy and environmental conservation have rekindled prospects for automotive and other applications of TE materials. [9]

4.1.1.1 The Seebeck effect

Charge carriers in metals or semiconductors can carry both heat and charge, resulting in the TE effect. When a TE material is subjected to a temperature gradient, the charge carriers at the hot side gain higher electrostatic potential than those at the cold side. This generates an electrostatic field, or voltage, which is referred to as the Seebeck effect.

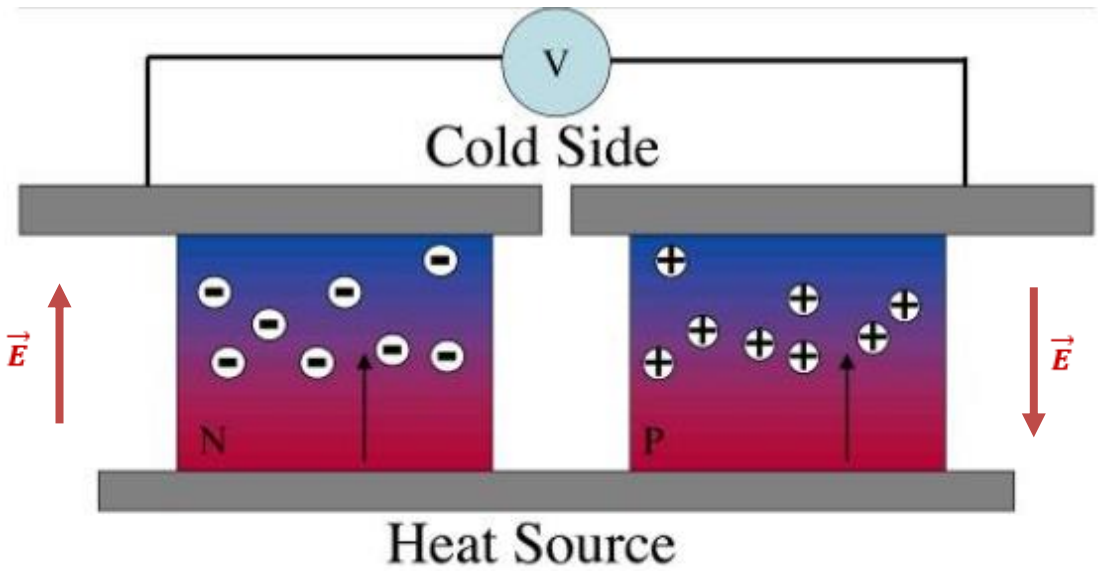

Figure 2 – TE device converts heat flux into electrical energy from a temperature gradient. The difference in sign is determined by the Seebeck coefficient for n-type and p-type semiconductors.

The ratio of the voltage generated by this process to the temperature difference is defined as the Seebeck coefficient, or *thermopower*, is expressed as:

$$S \equiv \frac{\Delta V}{\Delta T} \qquad (1)$$

The Seebeck coefficient also can be represented as an integral of electron energy states over the conductivity:[10]

$$S = -\frac{k_B}{e}\int\left(\frac{E-E_f}{k_BT}\right)\frac{\sigma(E)}{\sigma}\frac{\partial f_0(E)}{\partial E}\,dE \qquad (2)$$

where k_B is the Boltzmann constant, $f_0(E)$ is the Fermi distribution function, σ is the electrical conductivity ($\sigma = en\mu_e$; n and μ_e are the electron density and mobility, respectively), E_f is the Fermi energy, and e is an elementary unit charge. Considering the different signs of $E-E_f$ for n-type and p-type materials, the sign of the Seebeck coefficient determines the polarity of the TE material. Positive Seebeck coefficients indicate p-type semiconductors, and negative values indicate n-type semiconductors.

4.1.1.2 The Peltier effect

In the Peltier effect heat is absorbed or released while current passes through the material. In such case, charge carriers carry heat, as well. As a result, one side of the conductor will be heated while the other side will be cooled. Similarly, when electric current passes between two dissimilar materials, heat can be released or absorbed at this junction, depending on the differences between the Fermi energies of both materials. The rate of Peltier heat generation is expressed by:

$$\dot{Q} = \Pi I \qquad (3)$$

where Π is the Peltier constant and I is the current.

4.1.2 Thermoelectric material properties

Both thermal and electronic transport properties of TE materials are essential, as they dictate the device conversion efficiency. In the following section, we will present a brief description of the most relevant properties.

4.1.2.1 Thermal conductivity

Thermal conductivity is defined as the rate at which heat is transferred by conduction across a unit cross-section area of a material for a given temperature gradient. Thermal conduction can occur through two main mechanisms, conduction through the lattice vibrations (phonons) or through electrons. Metals are considered good thermal conductors, in which free electrons carry the major part in of heat. Conversely, non-metallic solids transfer heat by phonons mainly. The heat produced per unit time, $\dot{q}$, is proportional to the thermal gradient, as described by Fourier's law:

$$\dot{q} = -\kappa \frac{dT}{dx} \tag{4}$$

where κ is the thermal conductivity, and is directly related to the thermal diffusivity, α, and to the volumetric heat capacity, C_p, as follows

$$\kappa = \alpha \rho C_p \tag{5}$$

All of these properties are temperature-dependent.

The thermal conductivity can be described as a sum of two components: the lattice and electronic contributions, defined as κ_p and κ_e, respectively.

$$\kappa = \kappa_e + \kappa_p \tag{6}$$

The electronic contribution to the total thermal conductivity is linearly proportional to the electrical conductivity and to the temperature, which is expressed by the Wiedemann-Franz rule:[11]

$$\kappa_e = L_0 \sigma T \tag{7}$$

L_0 is the Lorenz number, which is commonly approximated by $2.45 \cdot 10^{-8}$ WΩK^{-2} for either metals or semiconductors in their degenerate limit.

Significant deviations from this constant value occur for non-degenerate semiconductors, where the nearly free electron approximation is not valid. A semi-empirical expression for the Lorenz number, valid for many chalcogenide-based semiconductors, was proposed by Kim et al.:[12]

$$L = 1.5 + \exp\left(-\frac{|S|}{116}\right) \tag{8}$$

Here, L is given in the units of 10^{-8} WΩK^{-2} and S in μV/K. As shown by Kim et al., this relation is accurate within 20% for PbTe and PbSe.

4.1.2.2 Figure of Merit and Thermoelectric Efficiency

The conversion efficiency of a given TE material depends on the materials' properties, and is quantified by a dimensionless TE *figure of merit*, defined as zT:

$$zT = S^2 \frac{\sigma}{\kappa} T \tag{9}$$

Optimization of zT is difficult, since S, κ, and σ are inter-related. For example, increase of the electrical conductivity by increase of the charge carrier concentration should result in increased thermal conductivity, as well. Furthermore, this leads to decrease

of S, as realized from equations 2 and 6. Since the electronic contribution to the thermal conductivity grows linearly with the electrical conductivity, it is beneficial to reduce the total thermal conductivity by treating its lattice component individually, thereby increasing *zT*. To summarize, optimization of zT requires fine-tuning of several material properties.

4.2 PbTe-based compounds

4.2.1 Pure PbTe

TE materials are classified into several groups based on their operating temperature range. The lead telluride compound, PbTe, is a mid-temperature (600-800 K)[13] TE material. It has a high melting temperature (1190 K) and good chemical stability. Its maximum operating temperature is 900 K. A Pb-Te binary phase diagram is presented in Figure 3.

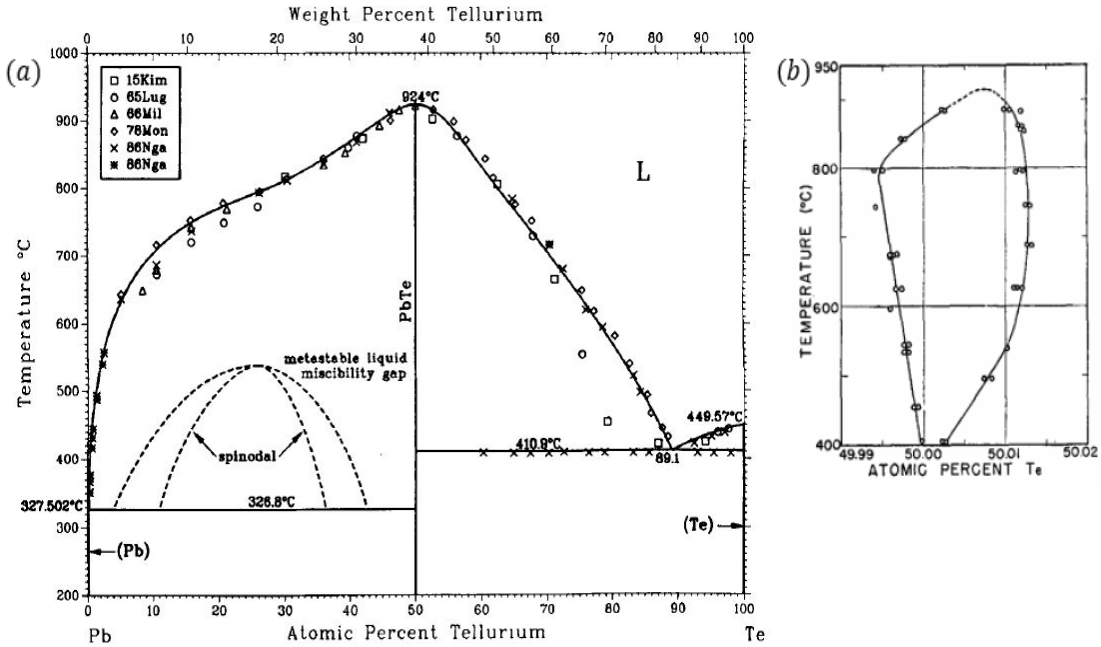

Figure 3 – (a) A binary phase diagram of the lead-telluride system. (b) A zoomed-in chart of the PbTe region around the 50 at. % Te concentration, showing a stable single-phase region for different temperatures.[14]

PbTe crystallizes in the NaCl crystal structure (rocksalt) with Pb atoms occupying the cationic and Te occupying the anionic sites. The maximum *zT* values of PbTe have been reported to range between 0.8 and 1.0 at ~ 650 K and the TE properties

of PbTe have been thoroughly investigated.[15] Thus, PbTe is one of the most widely used TE materials for space application.[9] Table I displays some of the relevant physical properties of PbTe.[16–18]

Table I – Physical properties of PbTe.

Property	Symbol	Value
Debye temperature	$\theta_D\ [K]$	136
Charge carrier concentration	$n\ \left[\frac{1}{cm^3}\right]$	$2.6 \cdot 10^{18}$
Charge carrier mobility	$\mu\ \left[\frac{cm^2}{V \cdot s}\right]$	383
Lattice constant	$a\ [A]$	6.454
Density	$\rho\left[\frac{g}{cm^3}\right]$	8.24
Grüneisen parameter	γ	1.96
Longitudinal sound velocity	$v_L\ \left[\frac{m}{s}\right]$	3596
Transverse sound velocity	$v_S\ \left[\frac{m}{s}\right]$	1610
Average sound velocity	$v_A\ \left[\frac{m}{s}\right]$	1770
Young's modulus	$E[GPa]$	27.7

The ratio of the lattice thermal conductivity to the total thermal conductivity is also an important property of PbTe. The lattice thermal conductivity is about 2.2 W/mK at room temperature, which is about 90 % of the total thermal conductivity and decreases with increasing temperature. This implies that control of thermal conductivity via second-phase nucleation is plausible.

The direct bandgap of PbTe is 0.31 eV at 300 K, [16] which is optimized for power generation applications and can be doped either n-type or p-type with appropriate dopants or anti-site defects (Te-rich PbTe is p-type, while Pb-rich PbTe is n-type); thus, the sign of Seebeck coefficient can be controlled. A common way to

control the magnitude of the Seebeck coefficient is by doping, in which Seebeck coefficients above 200 μV/K can be obtained. In the following work, we investigate the formation of Ag-rich second-phases such as Ag_2Te-precipitates in the PbTe-matrix.

4.3 Synthesis methods common to PbTe compounds

Many PbTe compounds have been studied as TE materials for many years. A variety of appropriate synthesis procedures were investigated for these alloys. Herein, we present the major ones.[19]

4.3.1 Hot-pressing

During the 1960's NASA produced PbTe thermoelements by hot-pressing (HP) of powders. The dies used for the HP process were baked out at or near the HP temperature to eliminate release of volatile impurities into the compacted powder. The top and bottom faces of the punches were coated with fine Al_2O_3 powder to ensure easy removal of the pressed pellet. The die was then heated to a temperature of 744 °C at inert argon atmosphere under pressure of 1.25 psi for 15-5 min.[20]

4.3.2 Spark plasma sintering

The pioneering works related to the spark plasma sintering (SPS) process started in 1906. SPS was developed by A. Bloxam, who was the first to use direct current resistance sintering apparatus. SPS, also known as field assisted sintering technique, is a pressure-assisted pulsed-current process, in which the powder is loaded into an electrically conducting die, and then sintered under a uniaxial pressure. SPS is one of the common methods for PbTe sintering.[21] In 2012, Biswas et al. [1] reported on a remarkable PbTe-based compound performance (zT=2.2) prepared using SPS. In their work, elemental Pb and Te were sealed in a quartz vial under Ar atmosphere and held at 975 °C for 2 h and, subsequently, quenched in water followed by homogenization heat treatment at 600 °C for 24 h. The density of the sample has 98% of the theoretical value.

4.3.3 Sol-gel process

The sol-gel method offers an advantage of low temperature preparation, higher purity, and better homogeneity, and has opened a new approach to the development of materials for nonlinear optical applications, partly PbTe-based.[22] An example for such preparation can be found at Ganguly et al.'s work.[23] In his work, nanometric PbTe gels and aerogels were prepared using a solution contains lead acetate trihydrate with oleic acid and 1-octadecene. After heating at 170°C for 30 minutes in an inert atmosphere the solution mixed with a solution of trioctylphosphine telluride and quenched in a cold-water bath. Finally, to grow the NPs they add hexane as the solvent and acetone as the anti-solvent followed by separation via centrifugation.

4.3.4 Microwave synthesis

A rapid and reliable process to synthesize nanocrystals of PbTe-based alloys is solid-state microwave synthesis. In this method, a precursor (powder containing Pb and Te) is sealed at 10^{-5} mbar in a quartz ampoule and exposed to microwave radiation in a microwave oven for a certain duration. For example, Hmood et al. exposed ingots of a $PbSe_{1-x}Te_x$ alloy to microwave radiation operating at 2.54 GHz for ca. 25 min. This technique can be used to synthesize nanocrystals of 15–100 nm size.[24]

4.3.5 Ag-alloyed PbTe

4.3.5.1 Importance of second-phase nucleation

Proper nucleation of second-phases can provide a significant effect on lattice thermal conductivity reduction when the distance between the precipitates (d) is between the mean free paths (MFPs) of the electrons (ca. 10 nm) and the phonons (100 nm on average, depending on wavelength). In such cinrcumstances, phonons are scattered, which leads to reduction of the thermal conductivity, whereas electrons are not scattered, which ideally means no reduction of electrical conductivity, Figure 4.

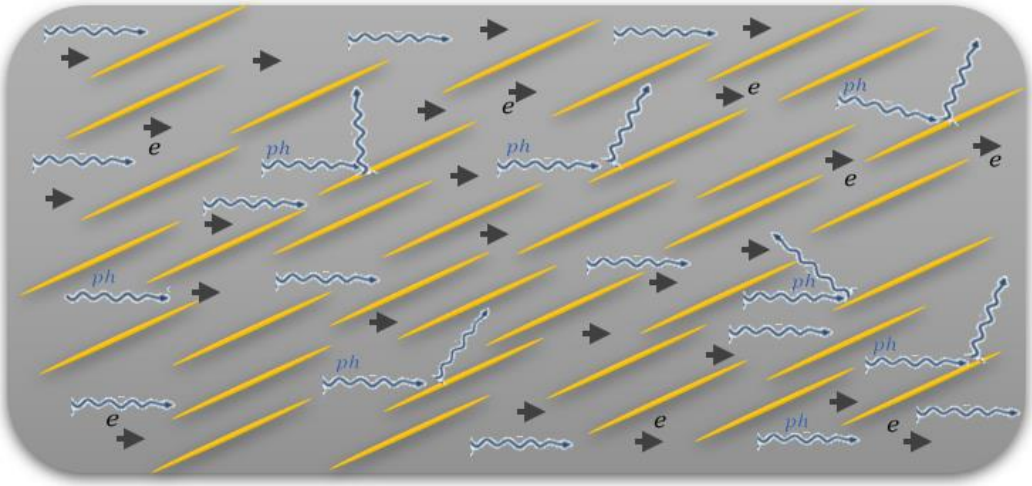

Figure 4 - The effects of Ag-rich precipitates on both charge carrier and phonon scattering. The black arrows represent electrons, and the wavy blue arrows represent phonons.

Formation of second-phases, lattice strains, as well as other nanometer-size features, plays a significant role in determination of the TE transport properties. It was also found that the key parameters determining the transport coefficients are the precipitate number density (N_v) - the number of precipitates per unit volume, and the matrix concentration.[25] In order to analyze the precipitates' evolution, Ariel Sheskin, a former member in our group, performed a combined transmission electron microscopy (TEM) and atom probe tomography (APT) analysis, and his main results are summarized in Figure 5. [26]

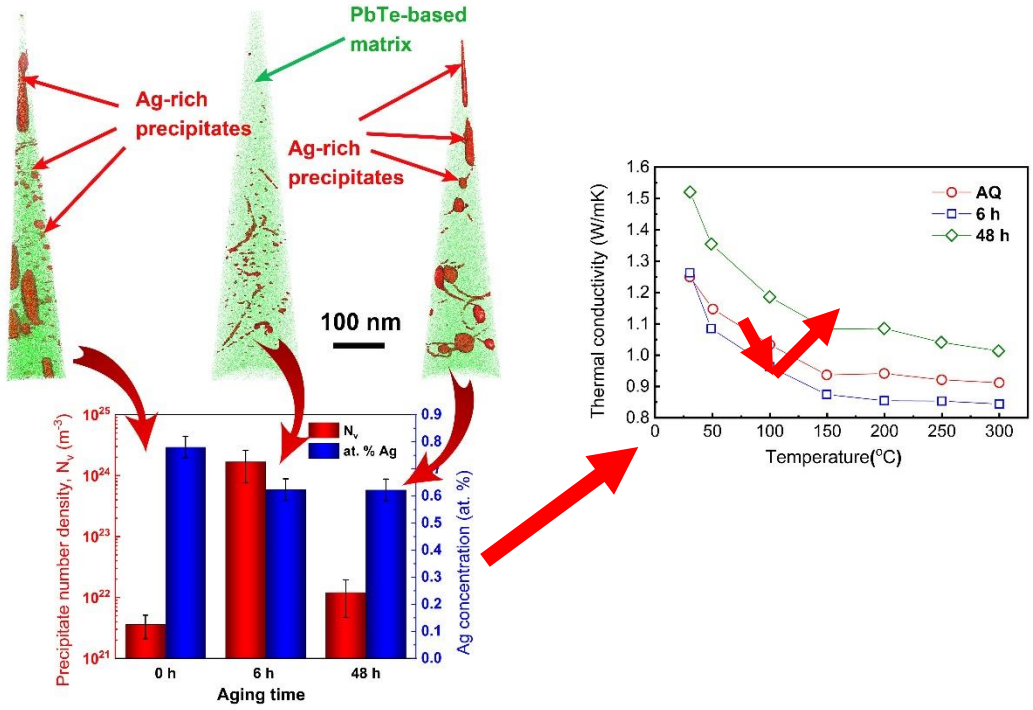

Figure 5 - Atom probe tomography (APT) reconstructions taken from an as-quenched alloy and those aged for 6 h and 48 h at 380 °C show that the precipitates' size decreased rapidly during 6 h aging and increased during the subsequent 42 h**.**

The number density, calculated from the APT data, shows an opposite behavior to the thermal conductivity. As expected, the thermal conductivity was found to decrease with the increase of the number density. The changes in the transport coefficients were attributed to the nucleation process during the first 6 h and to the coarsening process during the subsequent 42 h. Figure 5 reveals two important conclusions:

1. Microstructure evolution takes place rapidly.
2. It greatly affects the TE performance.

4.3.5.2 The Ag_2Te phase (Hessite)

In some PbTe-based systems, strong reduction of the lattice thermal conductivity has also been observed with increasing values of Ag_2Te percipitates' number density. Needle-like α-Ag_2Te precipitates, 100–200 nm long and 50–100 nm

thick, were uniformly distributed in the PbTe-matrix by fine control of the material synthesis conditions, based on the equilibrium phase diagrams.[27–31]

Despite the relatively large Ag_2Te precipitates, incorporation of Ag_2Te into the PbTe-matrix led to reduction of the lattice thermal conductivity from 0.93 down to 0.85 $Wm^{-1}K^{-1}$ for a temperature of 300 °C after 6 h aging at 380 °C, a 10% smaller thermal conductivity.[18] The second phase α-Ag_2Te is a thermodynamically stable phase. The PbTe/Ag_2Te system is described by a quasi-binary phase diagram, as shown in Figure 6.

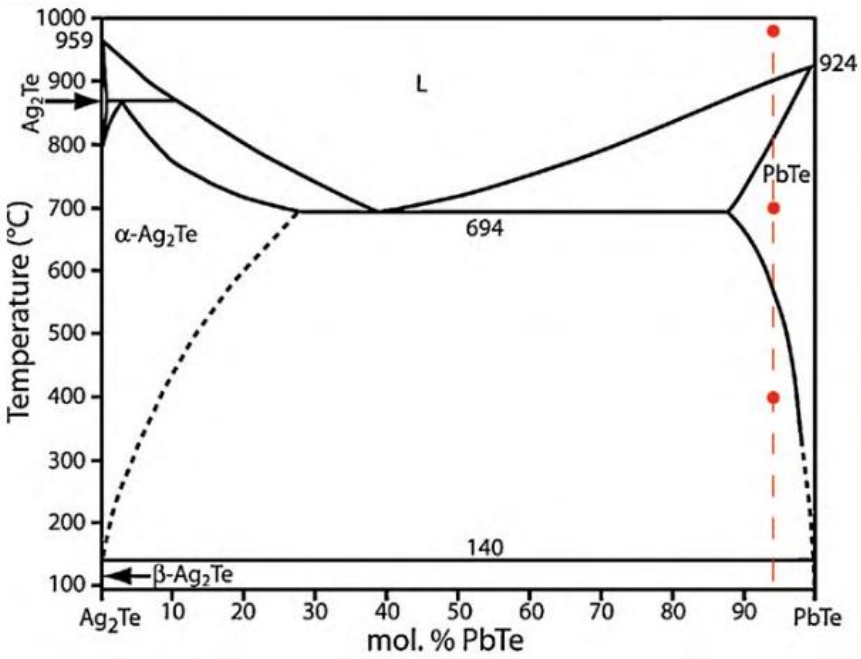

Figure 6 – A quasi-binary Ag_2Te-PbTe phase diagram. The dashed red line indicates an optional composition heat-treated at different conditions, indicated by the red dots.[29]

As shown in Figure 6, the α-Ag_2Te phase is thermodynamically favored at temperatures within the operation conditions of PbTe-based TEGs (140 -694 °C). The α-Ag_2Te phase has an FCC crystal structure (space group $Fm\bar{3}m$ and lattice parameter a = 6.63Å at 400 °C) with Te atoms residing at FCC sites; half of the Ag atoms occupy the [1/4, 1/4, 1/4] positions, and the rest occupy interstitial sites.[29,32] For temperatures below 140 °C, the α-Ag_2Te phase transforms into the monoclinic phase β-Ag_2Te with the P21/c space group with a= 8.09 Å, b= 4.48 Å, c = 8.96 Å and β= 123.2°. There are

five known stable solid phases in the Ag-Te system: Pure Ag (FCC) (Ag), Pure Te (hexagonal), Ag_2Te, $Ag_{1.9}Te$, and Ag_5Te_3. The Ag-Te phase diagram assessed based on experimental measurements, at atmospheric pressure is shown in Figure 7.

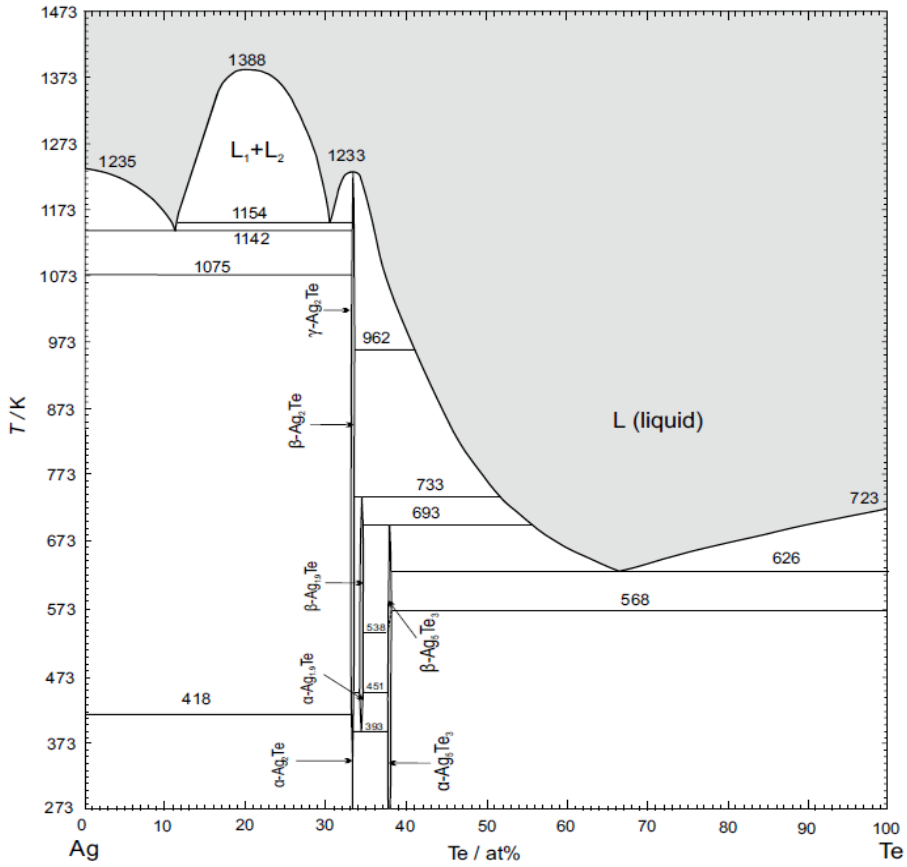

Figure 7 – Ag-Te phase diagram.[33,34]

4.3.5.3 The AgTe phase (Empressite)

In 1914, the Empressite mineral was revealed in the Empress-Josephine Mine by Prof. R. D. George of the University of Colorado.[35] The natural mineral Empressite found to correspond to the atomic ratio Ag:Te, as recorded in JCPDS 04-014-6681. Empressite is considered a rare mineral that usually coexists with Hessite (Ag_2Te) and Stützite (Ag_7Te_4).[36] Empressite is a metastable phase and, therefore, does not appear in the Ag-Te binary phase diagram. The mineral Empressite can be observed below 210 °C, as differential thermal analysis (DTA) implies, while above this temperature it decomposes into Stützite and native tellurium.[34,36] Bindi investigated this phase using in-situ x-ray single-crystal diffraction in the temperature range 25–190 °C and also concluded that AgTe remains stable with an orthorhombic crystal structure.[36]

Sheskin et al.,[28] however, identified the 1:1 Ag-Te stoichiometry after quenching of homogenized samples at 700 °C for 48 h. They found that needle-like precipitates as long as 100 nm with diameter between 10 and 100 nm exhibited an Ag/Te ratio of nearly 2:1, whereas smaller ones (1−10 nm diameter)exhibited a ratio of nearly 1:1. As a side-effect, small precipitates induce a high degree of coherency strain fields into the matrix; as the precipitates grow, they lose their coherency, which leads to strain relief. This implies that the Ag:Te spherical precipitates can be regarded as seeds for nucleation of needle-like Ag_2Te precipitates in the subsequent annealing stages.[28]

4.3.5.4 The $AgTe_3$ phase

$AgTe_3$ was first discovered using x-ray analysis by Luo et al.[37] during rapid cooling from a melt containing 20-30 at. % Ag heated at a temperature range of 650 - 750°C. Range et al.[38] described the pressure and temperature relations in $AgTe_3$ using high-pressure differential thermal analysis (HP-DTA), Figure 8.

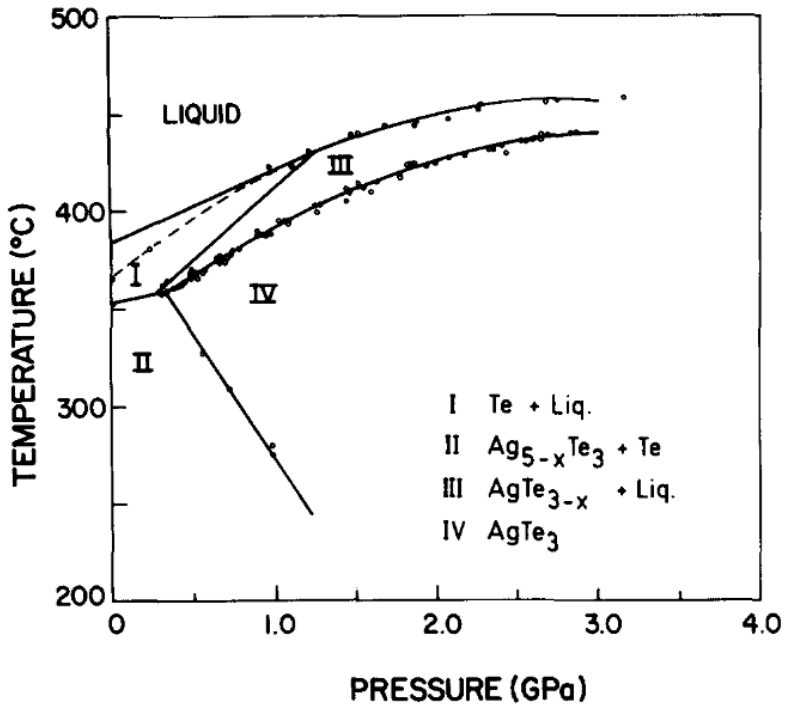

Figure 8 – Pressure and temperature-relations in the silver-tellurium system at 75 at-% Te. Phase boundaries are given as least-square-fitted curves, and the dotted lines represent metastable transitions.

$AgTe_3$ is a metastable phase formed during rapid cooling or under high pressures. As showed by Range et al., rapid quenching of alloys with a 1:3 ratio of Ag/Te from an equilibrated melt above 365 °C at a pressure of 1 atm. always produce a certain portion of the metastable $AgTe_3$ phase. Moreover, decomposition of this phase requires high-temperature annealing. $AgTe_3$ phase is also found to become a stable phase only at high pressures (above 400 MPa).[38] In 1964, the metallic $AgTe_3$ phase was found to be superconducting below 2.6 K by Luo et al.,[39] though not in its stable state. In 1982, Range et al.[40] described the decomposition of the rhombohedral $AgTe_3$ into its thermodynamically stable state by its color change from gold to silver. As follows from JCPDS 04-004-8714, its lattice parameters are a=8.645 Å, c=5.272 Å.

4.3.5.5 Ag-based PbTe solid solutions

The silver atoms occupation state is of an amphoteric nature,[28,41] which influences the electrical properties of the material. Sometimes the silver atoms occupy interstitial sites, thus act as donors (n-type), while sometimes they occupy Pb-substitution sites, thus act as acceptors (p-type), since Pb atoms are divalent and Ag-atoms are monovalent. Figure 3 demonstrates this concept based on a previous study done by our group. [28,41] It was found that the site-occupation of Ag atoms is a function of their concentration [C], as well as temperature and aging time [t_a].

The following findings were reported by us recently: [28,41] (1) The concentration of Ag-atoms dissolved in the PbTe-matrix decreases upon aging at 380°C. (2) Nucleation of Ag-rich precipitates takes place up to 6 h aging with the highest number density (N_v), and the onset of coarsening is between 6 and 48 h, see Figure 9.

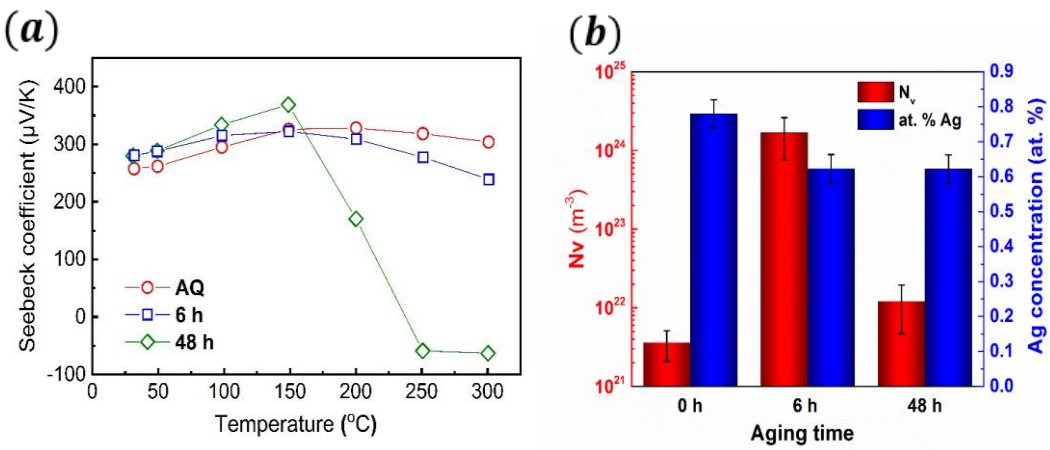

Figure 9 - (a) Aging time can modify the p/n-type polarity of an Ag-doped PbTe system, as manifested by *p*-to-*n* transition for T>200°C. (b) Aging time can modify the Ag concentration in the matrix and change the number density of Ag-rich precipitates. Full details are provided by Sheskin et al.[28,41]

Ag-rich precipitates can also act as reservoirs for Ag-dopants and their evolution modifies the p/n-type polarity of the PbTe matrix upon heat treatments. Such a phenomenon is termed *dynamic doping*.[42] It is, therefore, important to investigate diffusion properties of silver in lead-telluride compounds, which is expected to provide deeper insights into the kinetics of microstructure evolution, thereby improving our ability to control the nucleation, growth, and morphology of Ag-rich precipitates.

4.4 Kinetics of microstructure evolution

The challenge in producing second-phase in TE materials for phonon scattering lays in controlling the size, number density, and distribution uniformity of the precipitates, so as to yield maximum scattering effect. For homogenous nucleation, the transformation kinetics of the nucleus growth is governed by the Gibbs free energy[43] The nucleus growth Gibbs free energy is balanced by the two competing factors, namely the volumetric free energy and interfacial free energy. This yield a maximum value of ΔG as depicted in Figure 10.

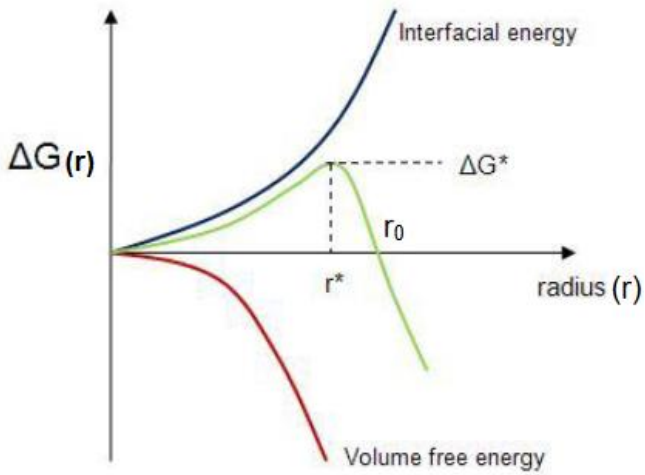

Figure 10 – A typical plot of the change of free energy for a spherical precipitate of radius r, yielding the energy barrier, $\boldsymbol{\Delta G^*}$, and critical nucleus size of $\boldsymbol{r^*}$.

The nucleation rate, I, depends on both ΔG^* and the rate in which solute atoms arrive at the nucleus, according to the following Arrhenius-type expression:[13,44,45]

$$I \propto \exp\left(-\frac{\Delta G^* + \Delta G_D}{RT}\right) \tag{10}$$

where ΔG_D is the Gibbs free energy for diffusion.

There are two main approaches to describe the theory of diffusion: continuum and atomistic approach. We will further describe both approaches, highlighting the aspects most relevant for this study.

4.4.1 Diffusion in crystals – the continuum approach

The continuum approach is based on Fick's laws (1855). The first Fick's law in a three-dimensional space states that the particles diffusion flux, $\vec{J}$, is formed in the opposite direction to the gradient of concentration, C, and can be expressed by the following form[46]

$$\vec{J} = -D\vec{\nabla}\, C(x, y, z, t) \tag{11}$$

D is the diffusion coefficient of the diffusing particles, and is given in unit of length^2/time. The units of $\vec{J}$ are particles/time×cross-section area.

Applying the mass conservation law and assuming that D is not a function of x, the concentration change is proportional to the local Laplacian of the concentration, as described by as Fick's second law: [46]

$$\frac{\partial C}{\partial t} = D\nabla^2 C \tag{12}$$

which is known as the diffusion equation. Using the second law, the diffusion coefficients can be extracted from concentration profiles, equation 12, and can be derived analytically using particular initial and boundary conditions.

Equation 12 can be solved for many boundary conditions. [46,47] For example, in the case of diffusion couples, where the concentration at the interface is maintained constant, the solution for one dimension can be expressed as:[48]

$$C_i(x, t) = C^\alpha + (C^\alpha - C_0)\,\mathrm{erf}\left(\frac{x}{2\sqrt{D_i t}}\right) \tag{13}$$

where C_i is the concentration of an element i in the bulk at time t, C^{α} is the concentration of an element i at the surface, C_0 is the concentration of an element i far away from the interface, and D_i is its diffusion coefficient.[32]

4.4.2 Diffusion in crystals – the atomistic approach

In the atomistic approach, diffusion is treated by considering an element with given probabilities to jump toward different directions. The atomistic approach can be applied for different media, e.g. (i) in bulk; (ii) along grain boundaries or (iii) dislocations, or (iv) at external surfaces. In the case of diffusion along confined media (cases ii through iv), the lattice structure is not considered when defining the elementary jumps. Conversely, for the case of bulk diffusion the lattice structure plays a key role, yielding eight optional mechanisms for elementary jumps: (i) Relaxation mechanism; (ii) Exchange mechanism; (iii) Ring mechanism; (iv) Interstitialcy mechanism, also called the "kick-out" mechanism; (v) Crowdion mechanism; (vi) Vacancy mechanism; (vi) Di-vacancy mechanism; and (vii) Interstitial mechanism.[49–51] In this work, we focus of the interstitial diffusion mechanism.

4.4.2.1 The random walk theory

The concept of random walk was first introduced by Pearson in a letter to *Nature* in 1905.[52] Let us assume that a particle can jump to either left or right directions without "memory" of its preceding jumps.

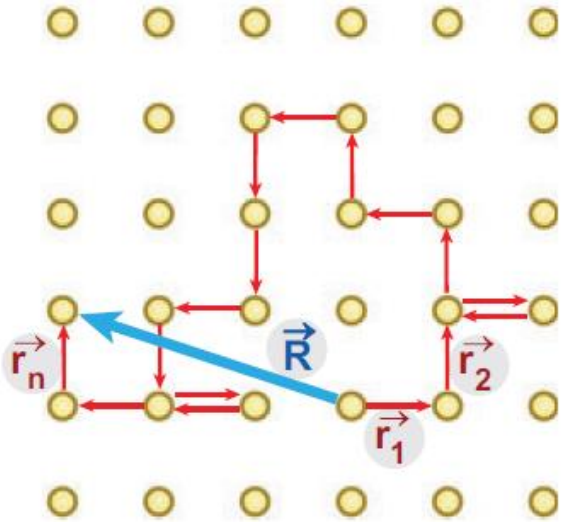

Figure 11 – An illustration of a random walk taking place in a uniform lattice showing how the net displacement after n-steps (blue arrow) is much shorter than n times the length of each jump (short red arrows). The yellow particles represent be optional lattice sites.[47]

Applying the random walk theory and defining a frequency of jumps, Γ, as the average number of jumps per unit time, τ, the dependence of the diffusion coefficient on the frequency of jumps for a 3D cubic isotropic crystal is given by the following form:

$$D = \frac{1}{6}\Gamma_i \Delta^2 \tag{14}$$

where $\vec{\Delta} = (\Delta_x, \Delta_y, \Delta_z)$ is the length vector of jumps. Different theories were developed in attempt to define the frequency of jumps. In the sections below some of the well-established theories are described in detail.

4.4.3 The transition state theory (TST)

In crystals the potential energy of atoms is regarded as multiple potential wells, as shown in Figure 12, which are located periodically in the 3D space. Random thermal fluctuations in the lattice supply the adequate energy for an atom to pass through the high-energy configuration between adjacent lattice positions. An atom diffusing between two adjacent potential wells will encounter an energy barrier, which is a transition state located at or near a saddle point in the 3D coordinate-energy diagram.

The *transition state theory* (TST)[49,53,54] hypothesizes that there is a state between the reactants and products that can be treated in terms of local equilibrium. To obtain an expression for the frequency of jumps, Γ, at which an atom passes through this energy barrier (activation energy), we will first describe Eyring's reaction-rate theory.

4.4.3.1 Eyring's reaction rate theory

In chemistry, reactions are explained assuming an activated complex formed between the reactants, which dissociates into products. The reaction rate was defined by Eyring (1934)[55] as:

$$\Gamma = \frac{k_B T}{h} \frac{Z_{TS}}{Z_0} \tag{15}$$

Where Z_{TS} and Z_0 are partition functions for the activated and the ground states, respectively, and h is Planck's constant. Wert and Zener showed [56] (1949) that Z_{TS} and Z_0 can be expressed as the partition functions of the system containing a solute atom plus its neighbouring atoms in the lattice and of the solute atom in its initial position, respectively. It should be noted that Z_0, the partition function of the system while the solute atom is at the ground state, has one more degree of freedom - the direction that is perpendicular to this separating plane. To obtain a ratio of partition functions that have the same number of degrees of freedom (the ratio between Z_{TS} and Z_0), it is necessary to separate Z_0 into two factors: the partition function for a <u>single</u> linear oscillator which represents the vibrational motion of the atom <u>about its equilibrium position along the direction of the jump</u>, Z_v, and the partition function for the complete system, with the jumping atom <u>constrained to move in a plane normal to the direction of diffusion</u>, Z_1.

$$Z_0 = Z_v Z_1 \tag{16}$$

Since Z_{TS} and Z_1 have the same number of degrees of freedom, substituting them in equation 15 yields the exponent of the Gibbs free energy for migration, G_m, which expresses the difference between the configuration when the atom is at the saddle point and when the atom is in a lattice site. Wert and Zener also expressed Z_v^{-1} for a harmonic lattice to be $Z_v^{-1} = 2\sinh\left(\frac{h\tilde{\nu}}{2k_B T}\right)$ for an atom vibrating at the direction of the jumps <u>about its equilibrium position</u> with an effective frequency of $\tilde{\nu}$. For the high

temperature regime, it can be approximated to a value of $Z_{\nu}^{-1} \approx \frac{h\tilde{\nu}}{k_B T}$.[54] Wert and Zener defined the jump frequency, Γ, using the following form:

$$\Gamma = \tilde{\nu} e^{-\frac{\Delta G^M}{k_B T}} \tag{17}$$

Where ΔG_M is the difference between Gibbs free energies of the crystal required for migration of atoms from the initial site to the saddle point; the subscript *M* stands for "migration". The enthalpy (*H*) and entropy (*S*) of diffusion are identical with the pertinent migration quantities of interstitial diffusion, that is, $\Delta S = \Delta S^M$ and $\Delta H = \Delta H^M$ where H^M denotes the enthalpy and S^M the entropy of such a system. The Gibbs free energy of migration can be expressed as: [57]

$$\boldsymbol{\Delta G^M = \Delta H^M - T\Delta S^M} \tag{18}$$

Based on these thermodynamic parameters, equation 17 can be expressed as follows:

$$\Gamma = \tilde{\nu}\, exp\left(\frac{\Delta S^M}{k_B}\right) exp\left(-\frac{\Delta H^M}{k_B T}\right) \tag{19}$$

4.4.3.2 The harmonic transition state theory (HTST)

One of the principal assumptions of the reaction-rate theory is that the particles move isothermally and reversibly from an initial stable position over a saddle point along the reaction coordinate in thermal equilibrium. Thermodynamically, this means that the reaction must occur at an infinitesimal increment of velocity. Vineyard (1957) applied a rigorous many-body approach to develop an expression for the jump rate.[54,58–60] Under the assumptions that (a) at all stages the of the reaction quantum effects can be neglected; and (b) atomistic motions near the saddle point can be treated as simple harmonic oscillations. Among the various diffusion mechanisms, the interstitial diffusion process is more relevant for our study. To understand this approach, let us assume a lattice with N atoms and 3N degrees of freedom.

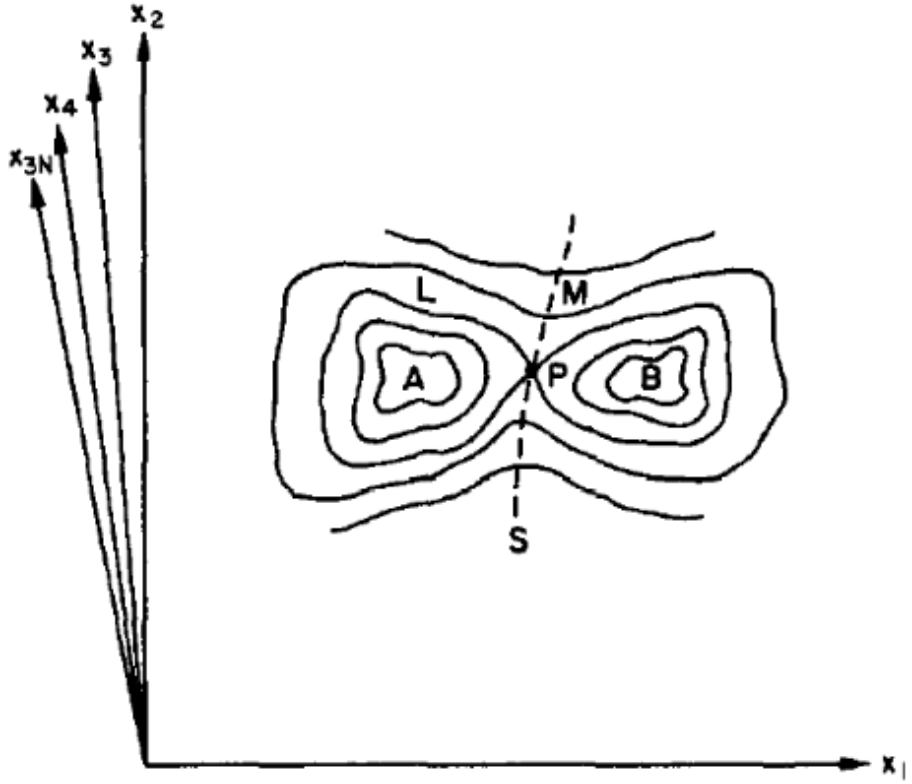

Figure 12 - Constant potential energy hypersurfaces (solid lines) of an N-dimensional energy diagram showing two equilibrium energy minima denoted by A and B, which represent voids at the structure. Atom located at site A will pass through a saddle point, denoted by P, on its way to the site B constrained in its motion to the hypersurface. M represents a point on the hypersurface S.[49]

The potential energy of the crystal φ, illustrated in Figure 12, possesses a minimum at a point A and B in the N-dimensional configuration space, corresponding to voids at the perfect cell while the diffusant is placed at an equilibrium position. Let us position an interstitial atom at point A. Its probability to reside in an arbitrary subspace on the contour S can be expressed as:

$$P_S = \frac{\int_S e^{-\frac{\varphi}{k_B T}} dq}{\int_A e^{-\frac{\varphi'}{k_B T}} dq_A{}'} \equiv \frac{Z_S}{Z_A} \qquad (20)$$

Where Z_S and Z_A are configuration integrals over the coordinates q of zones S and A, respectively, and φ is the potential energy. It is important to note that in numerator we perform an integral along countor S and in the integral denominator on area A. Hence

P_s is in units of 1 / length. Assuming the jump of the interstitial atom takes place between point A and B, its probability of residing in the transition state is the ratio of number of representative points in S that have positive velocities in the diffusion direction, towards point B, and the number of representative points which at point A.

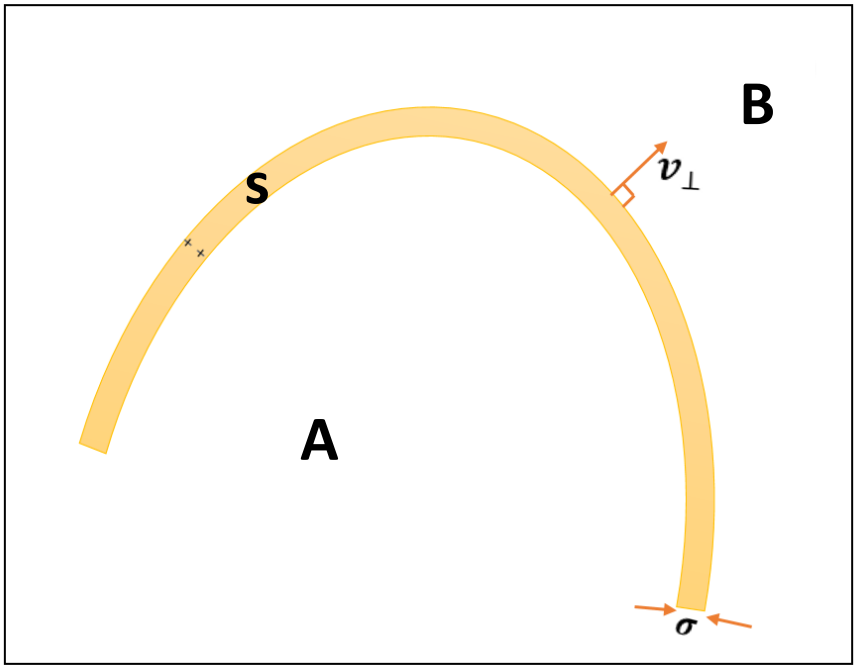

Figure 13 – An illustration of the assumption that the thickness of the subspace is σ and the velocity of crossing the transition state is $\boldsymbol{v}_\perp$ for jumping from A to B.

Vineyard assumed that in classical systems in equilibrium the position and velocity at a point are independently distributed. The jump rate can be expressed by multiplying the probability of being in S times the contour unit thickness, σ, times the average velocity perpendicular to contour S per unit thickness, $\langle \vec{v}_\perp \rangle / \sigma$

$$\Gamma^{TST} = \sigma P_S \frac{\langle \vec{v}_\perp \rangle}{\sigma} \tag{21}$$

The average velocity to perpendicular the contour S, $\langle \vec{v}_\perp \rangle$, can be calculated by separating the perpendicular velocity, $v_\perp$, and integrating with other direction velocities, $\vec{v}_i$, and integrating positive velocities in the diffusion direction.

$$\langle v_\perp \rangle = \frac{\int_{-\infty}^{\infty} v_\perp e^{-\frac{\sum_i \frac{1}{2} m v_i^2}{k_B T}} d\vec{v}}{\int_{-\infty}^{\infty} e^{-\frac{\sum_i \frac{1}{2} m v_i^2}{k_B T}} d\vec{v}} = \frac{\int_0^{\infty} v_\perp e^{-\frac{\sum_i \frac{1}{2} m v_\perp^2}{k_B T}} dv_\perp}{\int_{-\infty}^{\infty} e^{-\frac{\sum_i \frac{1}{2} m v_\perp^2}{k_B T}} dv_\perp} \frac{\int_{-\infty}^{\infty} e^{-\frac{\sum_i \frac{1}{2} m v_i^2}{k_B T}} d\vec{v}_i}{\int_{-\infty}^{\infty} e^{-\frac{\sum_i \frac{1}{2} m v_i^2}{k_B T}} d\vec{v}_i}$$

$$= \frac{\int_0^{\infty} v_\perp e^{-\frac{\sum_i \frac{1}{2} m v_\perp^2}{k_B T}} dv_\perp}{\int_{-\infty}^{\infty} e^{-\frac{\sum_i \frac{1}{2} m v_\perp^2}{k_B T}} dv_\perp} = \sqrt{\frac{k_B T}{2\pi m}} \tag{22}$$

Where $i = 1, \ldots 3N - 1$, $q_i = \sqrt{m_i} y_i$, and $v_i \equiv \dot{q}_i$ and the mass will be cancelled-out in future approximations using a constant ration between the frequency and harmonic oscillator constant: $\nu = \omega / 2\pi = (1/2\pi) \sqrt{(k/\mu)}$. Thus, Vineyard's rate is reduced to the following form:

$$\Gamma^{TST} = \sqrt{\frac{k_B T}{2\pi m}} \frac{Z_S}{Z_A} \tag{23}$$

The next step is performing the harmonic approximation. Taylor expansion of the potential energy surface, φ, at the saddle point, S, and around the minimum, A, yields the following form:

$$\varphi^T \approx \varphi_T + \sum_i^{D^T} \frac{1}{2} k_i^T q_{T,i}^2 \tag{24}$$

Where T represents a location at the saddle point, S, or at the initial state, A, and $k_i^T = 2\pi \nu_i^T$ are the i normal modes (having a maximum number of D^T), which count 3N at the initial state and 3N-1 at the saddle point (this is because we disregard the vibration in the B direction, see Figure 13 and Figure 12, where the potential is lower than at the saddle point, i.e. no vibrations). Equations 24, 20, and 23 yield:

$$\Gamma^{HTST} = \frac{\prod_{i=1}^{3N} \nu_i^A}{\prod_{i=1}^{3N-1} \nu_i^S} e^{-\frac{Q}{k_B T}} = \nu^* e^{-\frac{Q}{k_B T}} \tag{25}$$

Where Q is the difference between φ_S and φ_A, ν^* is Vineyard effective frequency, and ν_i^T are the harmonic vibrations ($T = A$ or S).[54,59,60] The approximation is valid for high temperatures, unless quantum effects become significant.[54,61] Here, the frequency of the unstable vibration mode of the activated state (in the direction of the diffusion path) is excluded from the equation 25.

4.4.3.3 The quasi-quantum approximation of HTST (QQ-HTST)

The zero-point energy (ZPE) effect arises when the quantum "zero-vibrations" in the ground and in the transition states are not identical. To address this phenomenon, the quantum mechanical partition function is used instead of the classical partition function, where zero-point energy terms are added as small corrections to both φ_s and φ_A; thus, the term $Q = \varphi_s - \varphi_A$ is now replaced by:

$$Q = \left(\varphi_S + \sum_{i}^{3N-1} \frac{h\nu_i^S}{2}\right) - \left(\varphi_A + \sum_{i}^{3N} \frac{h\nu_i^A}{2}\right) \tag{26}$$

This yields the quasi-quantum approximation (QQ-HTST), [53,54,59,61] and a new expression for the jump rate:

$$\Gamma_{QQ-HTST} = \frac{k_B T}{h} \frac{\prod_{i=1}^{3N} 2sinh\left(\frac{h\nu_i^0}{2k_B T}\right)}{\prod_{i=1}^{3N-1} 2sinh\left(\frac{h\nu_i^{TS}}{2k_B T}\right)} e^{-\frac{\varphi_S - \varphi_A}{k_B T}} \tag{27}$$

This form of TST includes ZPE effects, however disregards the tunneling effect. This form of transition is useful for low temperatures, where ZPE correction is not negligible.

4.4.3.4 Interstitial diffusion

Among other diffusion mechanisms, interstitial diffusion is the simplest process , which means that an impurity atom jumps between two adjacent interstitial sites.[57]

In 1949, Wert and Zener introduced the temperature-independent diffusion coefficient factor D_0 of interstitial solute atoms in metals. The theoretical diffusion coefficient for interstitial atoms in a cubic lattice has the following form[56]

$$D = n\beta d^2 \Gamma \tag{28}$$

where n is the number of nearest-neighbour stable sites for the diffusing atom and β is the jump probability in the direction of diffusion; for example, the values of β for face-centred cubic (FCC) and for body-centred cubic (BCC) lattices are 1/12 and 1/8, respectively.[60] From the symmetry of rocksalt-derived systems, we can approximate $n\beta$ to be $n\beta=1$. [16]

Using equation 19 and equation 28, the diffusion coefficient of solute interstitials can be written as[57]

$$D = n\beta f d^2 v^* \exp\left(-\frac{\Delta G^M}{k_B T}\right) \tag{29}$$

While v^* is the effective frequency and f is the correlation factor , which is a correction for the non-randomness of the displacements and thus equals to 1 in the case of interstitial diffusion mechanism with isotropic symmetry, and d is the length of the diffusant's jump.

Substituting equation 18 into equation 29 yields the following expression:

$$D = n\beta f d^2 v^* \exp\left(\frac{\Delta S^M}{k_B}\right) \exp\left(-\frac{\Delta H^M}{k_B T}\right) \tag{30}$$

Its generic form is commonly expressed as:[56]

$$D = D_0 e^{-\frac{Q}{k_B T}} \tag{31}$$

Where $D_0 = n\beta f a^2 v^* \exp\left(\frac{S^M}{k_B}\right)$ is temperature independent, termed as the pre-exponential diffusion coefficient, and Q is the activation energy for migration, and equals ΔH^M.

4.4.4 Bulk diffusion coefficients typical for Pb-chalcogenide compounds

As opposed to metallic systems, the interstitial mechanism is preferred either in cases of loosely-packed crystal structures, or when impurities are considerably small compared to atoms of the host matrix. This is because in such systems the energy required for breaking bonds is small, which makes the interstitial mechanism, which requires atom transport with no need of vacancies, the best choice of nature. [49,59] Detailed information of diffusion in Pb-chalcogenide compounds is summarized in Table II. As shown and discussed by Dyson et al., [62] the dominant bulk diffusion mechanism of silver in face-centered cubic (FCC) lead is via interstitial sites, since the self-diffusion coefficient of lead is unaffected by dissolution of the noble element atoms considered therein (Cu, Ag, and Au). Fedorovich [63,64] reported on low solubility of silver in single crystalline PbSe grown by the Bridgman method (10^{-18} cm^{-3} at 400 °C and $8\cdot10^{-18}$ cm^{-3} at 850 °C) and low activation energy for diffusion, which led him

to suggest that diffusion of Ag in the PbSe system takes place via the interstitial mechanism.

Table II - A summary of experimentally acquired diffusion coefficients reported for Pb-chalcogenide compounds.

Diffusant	System	D_0 $\left[\frac{cm^2}{s}\right]$	ΔE $\left[\frac{kJ}{mole}\right]$	Temperature range (°C)	Proposed mechanism	Ref.
Ag	Pb	$4.6 \cdot 10^{-2}$	60.41		Interstitial	62
^{110}Ag	PbSe		33.76	400-850	Interstitial	63
^{210}Pb	PbSe	$4.98 \cdot 10^{-6}$	80	400-800	Primarily interstitial	65
^{75}Se	PbSe	$2.1 \cdot 10^{-5}$	115.782	400-800	Vacancy	65
^{210}Pb	PbSe +0.5% mol. Bi_2Se_3	$4.28 \cdot 10^{-2}$	155.34	-	-	65
^{210}Pb	PbSe +0.5% mol. Ag_2Se	$4.41 \cdot 10^{-7}$	53	-	-	65
Pb	PbTe	$2.9 \cdot 10^{-5}$	57.9	259-500	Vacancy	16
Te	PbTe	$2.9 \cdot 10^{-6}$	72.3	500-800	Vacancy	16
Cu	PbSe	$2 \cdot 10^{-5}$	29.91	93-520	Interstitial	16
Na	PbSe	$5.6 \cdot 10^{-6}$	38.6	400-850	Interstitial	16

Interstitial diffusion of ^{210}Pb or ^{75}Se in PbSe was studied by Seltzer et al.[65] over a temperature range of 400 through 800 °C for single crystal samples grown using the Bridgman technique. They also found that the presence of the Bi_2Se_3 phase in the

PbSe-matrix significantly reduces the diffusion rate of lead; conversely, the presence of the Ag_2Se phase in this system significantly increases the diffusion rate of lead for temperatures lower than the melting point of PbSe. The doped PbSe crystals were prepared by adding 0.5 mol. % of Bi_2Se_3 or Ag_2Se to the undoped PbSe prior to crystal growth by the Bridgman technique. Hence, the presence of such phases may alter the diffusion mechanism from interstitial to substitutional. Since the PbTe and PbSe systems are similar in their lattice structures and chemical behavior, we hypothesize that they should exhibit similar bulk diffusion mechanisms. It can, therefore, be assumed that introducing bismuth to PbTe should change the dominant diffusion mechanism. As discussed by Grossfeld et al., [13] alloying of the Ag-Pb-Te system with 0.05 at. % Bi results in retardation of the precipitation of the Ag_2Te phase. One of the options suggested by Grossfeld et al. was that the presence of Bi atoms in the PbTe-matrix reduces the diffusion rate of Ag, which may suppress the nucleation and growth of Ag_2Te-precipitates.

As discussed by Grossfeld et al., [13,27] adding Bi to an Ag-Pb-Te system results in needle or disk shape Ag_2Te precipitates after 6 hours of aging in contrast to the case without Bi doping. It was suggested that Bi atoms retard the diffusion rate of Ag in the PbTe matrix, which may suppress the evolution of the Ag_2Te to the spherical stable precipitates. Grossfeld et al. suggested that Bi atoms encourage “pinning” of the Ag_2Te-precipitates to their original sizes.

Measurements of Ag diffusion in PbSe matrix were performed by Fedorovich [63] using the ^{110}Ag radioactive isotope. This technique is considered to be the most accurate one for measuring diffusion coefficients due to its high sensitivity to low concentrations spanning over a range of about five orders of magnitude in radioactive intensity. The activation energy for diffusion and the pre-exponential diffusion coefficients reported by Fedorovich were 33.76 $kJ \cdot mole^{-1}$ and $7.4 \cdot 10^{-4}$ $cm^2 s^{-1}$, respectively.

To the best of our knowledge, only one study of direct estimation of silver diffusion in PbTe was reported. Didik et al.[66] (1979) estimated the diffusion coefficient of Ag in PbTe at 313 K to be ~ 10^{-14} $cm^2 s^{-1}$.

Additionally, the diffusion coefficient of Ag in PbTe can be extracted from the study of Bergum et al., [32] who measured the concentration of Ag atoms across the interface between PbTe–Ag_2Te diffusion couples applying electron probe microanalysis (EPMA) to determine the solvus lines of the PbTe and Ag_2Te phases in the pseudo-binary PbTe-Ag_2Te system. It is noteworthy that the goal of Bergum's study was not to determine diffusion coefficients; however, they can be indirectly extracted from the concentration profiles reported therein. The diffusion coefficients of Ag in PbTe at 375, 450, 550, and 650 °C were extracted to be $D_0^{Bergum} = 3.58\times10^{-5}$ $cm^2\cdot s^{-1}$ and Q=87.05 $kJ\cdot mole^{-1}$ by fitting the Ag-concentration profiles to the error function, describing diffusion of solute atoms from a semi-infinite source.

4.5 Density Functional Theory

"The fundamental laws necessary for the mathematical treatment of a large part of physics and the whole of chemistry are thus completely known, and the difficulty lies only in the fact that application of these laws leads to equations that are too complex to be solved." (Paul Dirac, 1902-1984)

This chapter describes the fundamentals of the density functional theory (DFT), which is a method to solve quantum many-body problems.

4.5.1 The many-body problem

The well-known time-independent, non-relativistic Schrödinger equation takes the following form

$$\hat{H}\psi = E\psi \tag{32}$$

This equation can be solved analytically for the simplest cases, i.e. harmonic oscillator. A more complex case involving multiple electrons and nuclei is known as the quantum-mechanical many-body problem.

Unfortunately, there is no analytical solution to the many-body problem for more than three interacting particles. Since solving the problem allows us to investigate the system's fundamental properties from first-principles, several approximate methods to solve the many-body problem were developed.[67] One of these methods is the DFT.

The fundamental basis of DFT[68] is that ground state energy of a many-electron system is a functional of the electron density, $n(r)$, and can be obtained by energy minimization with respect to $n(r)$. By doing so, we reduce the problem from 3N degrees of freedom, for N particles, to a much simpler three-dimensional problem. DFT is the major tool of modern computational chemistry and materials science, and is used here as an important tool for estimation of diffusion coefficients. In the section below, some of the most relevant approximations are described.

4.5.2 The Born-Oppenheimer approximation

For a many-body problem with N_1 nuclei and N_2 electrons, the following equation should be solved:

$$\left[\hat{T}_n + \hat{V}_{n-n} + \hat{H}_e\right]\psi = E\psi \tag{33}$$

where $\hat{T}_n$ is the kinetic energy of the N_1 nuclei of the system, $\hat{V}_{n-n}$ is the repulsion between the nuclei, and $\hat{H}_e$ is the electronic Hamiltonian. These terms are, explicitly, given by

$$\hat{T}_n = \sum_{\alpha=1}^{N_1} -\frac{\hbar^2 \nabla^2_{\vec{R}_\alpha}}{2M_\alpha} \tag{34}$$

$$\hat{V}_{n-n} = \sum_{\alpha,\beta=1;\alpha<\beta}^{N_1} \frac{Z_\alpha Z_\beta e^2}{\left|\vec{R}_\alpha - \vec{R}_\beta\right|} \tag{35}$$

$$\begin{aligned} \hat{H}_e &= \hat{T}_e + \hat{V}_{n-e} + \hat{V}_{e-e} \\ &= \sum_{i=1}^{N_2} -\frac{\hbar^2 \nabla^2_{\vec{r}_i}}{2m} + \left(-\sum_{\alpha=1}^{N_1}\sum_{i=1}^{N_2} \frac{Z_\alpha e^2}{\left|\vec{R}_\alpha - \vec{r}_i\right|} \right) \\ &\quad + \sum_{i,j=1;i<j}^{N_2} \frac{e^2}{\left|\vec{r}_i - \vec{r}_j\right|} \end{aligned} \tag{36}$$

Where M_α is the ion α mass, m is the electron mass, and Z_α is the ion α atomic number. $\vec{r}_i$ and $\vec{R}_\alpha$ are the position vectors of the ith electron and α ion, respectively. The electronic Hamiltonian comprises the kinetic energy of N electrons, $\hat{T}_e$, the interaction between the electrons and the nuclei, $\hat{V}_{n-e}$, and the electrostatic interaction between the electrons, $\hat{V}_{e-e}$.

As can be shown for the many-body Schrödinger equation, we should, ideally, consider every particle and its interaction with the other particles at the system. The problem has exponential complexity with the number of particles and any direct numerical solution is not feasible, even for the simplest systems. Moreover, the Hamiltonian presented here is stationary, and does not consider external fields. Spin-orbit coupling (SOC) and relativistic effects, which may be significant for heavy atoms, are excluded from this simplistic formulation. . Nevertheless, for simplicity we consider this form of Hamiltonian, ignoring time-dependence, relativistic effects, and external fields. [69]

We first apply the Born-Oppenheimer approximation,[70] considering only electron-related terms in the Hamiltonian, thus solving the Schrödinger equation for electrons only by neglecting the kinetic energy of the nuclei. Nucleus-nucleus interaction energy is constant. The justification for such approximation is the different time scales of the electronic and nuclear motion. Therefore, equation 33 now gets the following form

$$\hat{H}_e\psi = E\psi \tag{37}$$

By solving equation 37 for a given set of ion location $\{\vec{R}_\alpha\}$, we obtain the system's energy spectrum with the electronic part of the wave function.

4.5.3 Hohenberg-Kohn theorems

The Hohenberg-Kohn-Sham theory[68] simplifies DFT applying a one-electron approximation, in which the very complex many-body problem of interacting electrons is replaced by an equivalent, but a much simpler problem of solving the wave function of a single electron interacting with other electrons through an effective potential. A Schrödinger-like equation of one-electron wave function is defined with a potential energy term, i.e. an effective potential that is a function of electron density.

$$\hat{H} = \hat{T}_e + \hat{V}_{ext} + \hat{V}_{e-e} \tag{38}$$

$\hat{T}$ is the kinetic energy operator of the electrons, $\hat{V}_{e-e}$ represents the repulsion between the electrons in the system, and $\hat{V}_{ext}$ is the total energy due to the interaction of the electrons with an external field induced by the nuclei. These terms can be presented as

$$\hat{T} = \sum_{i=1}^{N_2} \frac{\hbar^2 \nabla_{\vec{r}_i}^2}{2m}, \quad \hat{V}_{ext} = \sum_{i=1}^{N_2} V_{ext}(\vec{r}_i), \quad \hat{V}_{e-e} = \sum_{i,j} V_{e-e}(\vec{r}_i, \vec{r}_j) \qquad (39)$$

where $V_{ext}(\vec{r}_i)$ is due to the interaction between an electron located at $\vec{r}_i$ and the external field induced by the nuclei (Coulombic interaction), and $V_{e-e}(\vec{r}_i, \vec{r}_j)$ is the interaction between each electron pair located at $\vec{r}_i$ and $\vec{r}_j$, which is not only due to the classical electrostatic interaction, however has an exchange-correlation contribution. Assuming that $\hat{V}_{e-e}$ is known, the number of electrons N and the external potential $\hat{V}_{ext}$ fully define the Hamiltonian and all properties of the ground state. In practice, $\hat{V}_{e-e}$ is not fully-known, which establishes the theoretical grounds for DFT, based on the two Hohenberg–Kohn theorems; to be introduced further below.[71]

4.5.3.1 The first Hohenberg-Kohn theorem

The first Hohenberg-Kohn theorem[68] states that there is a unique external potential denoting the interaction between electrons and nuclei, $E_{ext}(n_0(r))$, and is determined solely by the ground-state electron density, $n_0(r)$. Thus, if the system is at the ground state, the electron density alone can define the external potential and vice-versa. The ground-state electron density is expressed as:

$$n_0(\vec{r}) = N \int \left|\Psi_0(\vec{r}, \vec{r}_2, \dots, \vec{r}_{N_2})\right|^2 d\vec{r}_2 \dots d\vec{r}_{N_2} \qquad (40)$$

Mathematically, the ground-state energy is a unique functional of the ground-state electron density, $n_0(\vec{r})$:

$$E[n_0(\vec{r})] \equiv F[n_0(\vec{r})] + E_{ext}[n_0(\vec{r})] \qquad (41)$$

Where

$$F[n_0(\vec{r})] \equiv \langle \Psi_0 | \hat{T} + \hat{V}_{e-e} | \Psi_0 \rangle \qquad (42)$$

$$E_{ext}[n_0(\vec{r})] \equiv \langle \Psi_0 | \hat{V}_{ext} | \Psi_0 \rangle \qquad (43)$$

As follows from the first Hohenberg-Kohn theorem, the internal energy (electronic kinetic energy and the electron-electron energy) does not depend on the external potential, so that an internal energy functional, namely $F[n(\boldsymbol{r})]$, should exist, although its explicit formula is unknown, and this functional should be identical for all systems. Therefore, only the external potential changes according to the geometrical structure and type of nuclei.

4.5.3.2 The Second Hohenberg-Kohn theorem

The second Hohenberg-Kohn theorem defines the energy functional as $E[n(\mathbf{r})]=F[n(\mathbf{r})]+E_{\text{ext}}[n(\mathbf{r})]$ and proves that the correct ground state electron density minimizes this energy functional using the variational principle. Thus, for any electron density $n(\vec{r})$ with $n(\vec{r}) \geq 0$ and $\int n(\vec{r})d\vec{r} = N_2$ the following relationship holds:[69]

$$E[n_0(\vec{r})] \leq E[n(\vec{r})] \tag{44}$$

Combine the two theorems implies that the functional of the system provides the lowest energy, if and only if the pertinent electron density is the correct ground-state electron density.

4.5.4 Kohn-Sham Equations

In 1965, a year after Hohenberg and Kohn introduced their theorems, [72] Kohn and Sham suggested a practical scheme for calculating the ground state energy for a given system. At the first step, they rewrote equation 42, the internal energy functional, which is unknown as discussed in chapter 4.5.3.1, as follows

$$F[n(\vec{r})] = T_S[n(\vec{r})] + J[n(\vec{r})] + E_{XC}[n(\vec{r})] \tag{45}$$

Where $T_S[n(\vec{r})]$ is the kinetic energy of the non-interacting system and $J[n(\vec{r})]$ is the classical coulombic repulsion term

$$T_S[n(\vec{r})] = -\frac{\hbar^2}{2m}\sum_{i=1}^{N_2}\langle\varphi_i|\nabla^2_{\vec{r}_i}|\varphi_i\rangle \tag{46}$$

By doing so, Kohn and Sham defined the exchange-correlation (XC) energy functional, $E_{XC}[n(\vec{r})]$, and by comparing equations 45 and 42 they transformed the problem into an equivalent, non-interacting system constructed from a set of one-electron orbitals, φ_i. [72]

$$E_{XC}[n(\vec{r})] = (T[n(\vec{r})] - T_S[n(\vec{r})]) + (E_{e-e}[n(\vec{r})] - J[n(\vec{r})]) \tag{47}$$

In fact, $E_{XC}[n(\vec{r})]$ is the sum of the difference between the kinetic energy of the interacting system, $T[n(\vec{r})]$, and that of the non-interacting contribution to the kinetic energy, $T_S[n(\vec{r})]$, and the difference between the interaction between each pair of electrons, $E_{e-e}[n(\vec{r})]$, and that of the classical Coulombic repulsion, $J[n(\vec{r})]$. The

basic concept in Kohn and Sham approach is avoiding the more difficult problem, that is the unknown parts of the true kinetic energy, self-interaction, exchange, and correlation interactions; instead, this approach encompasses these unknowns in the term E_{xc}. In this approach, since this energy is less than 10% of the total energy, most of the information is computed exactly, whereas only a small part of it is approximated by a density functional. The exchange-correlation contribution is small but vital for calculation of some physical properties. Thus, choosing the best form of the exchange-correlation energy should lead to the precise solution of the Schrödinger equation describing the full system reliably.

Finally, Kohn and Sham (K-S) formulated their equation as follows[72]:

$$\left(-\frac{\hbar^2}{2m}\nabla^2 + \hat{V}_{eff}^{KS}(\vec{r})\right)\varphi_i(\vec{r}) = \epsilon_i\varphi_i(\vec{r}) \qquad (48)$$

The K-S effective potential, $\hat{V}_{eff}^{KS}$, contains the external potential, $\hat{V}_{ext}$, the Coulomb interaction of the electrons with themselves, namely the Hartree potential, $\hat{V}_H = \int \frac{n(\vec{r}')}{|\vec{r}-\vec{r}'|} d\vec{r}'$, and the exchange-correlation potential, $\hat{V}_{XC}$. $\varphi_i(\vec{r})$ is the K-S orbital, which represents the electronic state of the imaginary non-interacting system, and ϵ_i is the energy of the corresponding K-S orbital. K-S orbitals have no physical meaning, but the sum of the charge density related to these orbitals, obtained by replacing ψ_i with φ_i at equation 40, equals to the electron density of the real system. Equation 48 is then solved self-consistently to yield the ground state charge density, $n_0(\vec{r})$, from which the ground state total energy of the system with interacting electrons is obtained. The general DFT calculation process consists of the following steps:

1. Guess an initial set of K-S orbitals that would yield the initial electron density, $n(\vec{r})$, using Equation 40, and the location of the nuclei to form the external potential, $\hat{V}_{ext}(\vec{r})$1.
2. Build the electrons Hartree potential, $\hat{V}_H$, the approximated exchange-correlation potential, $\hat{V}_{XC}$, resulting in the K-S effective potential, $\hat{V}_{eff}^{KS}$, utilizing the guessed initial electron density.
3. Solve the K-S equation for a new set of K-S orbitals, φ_i^{new}, and use these new orbitals to build a new electron density.

4. Calculate the system's energy using the new set of K-S φ_i^{new} orbitals. Then, compare it to the total energy obtained by the old φ_i orbitals. If the difference between the two energies reaches at a convergence criteria, then the calculation ends. If not, then the iterative algorithm "jumps" back to step 2.
5. Various output quantities can be computed using the convergence results.

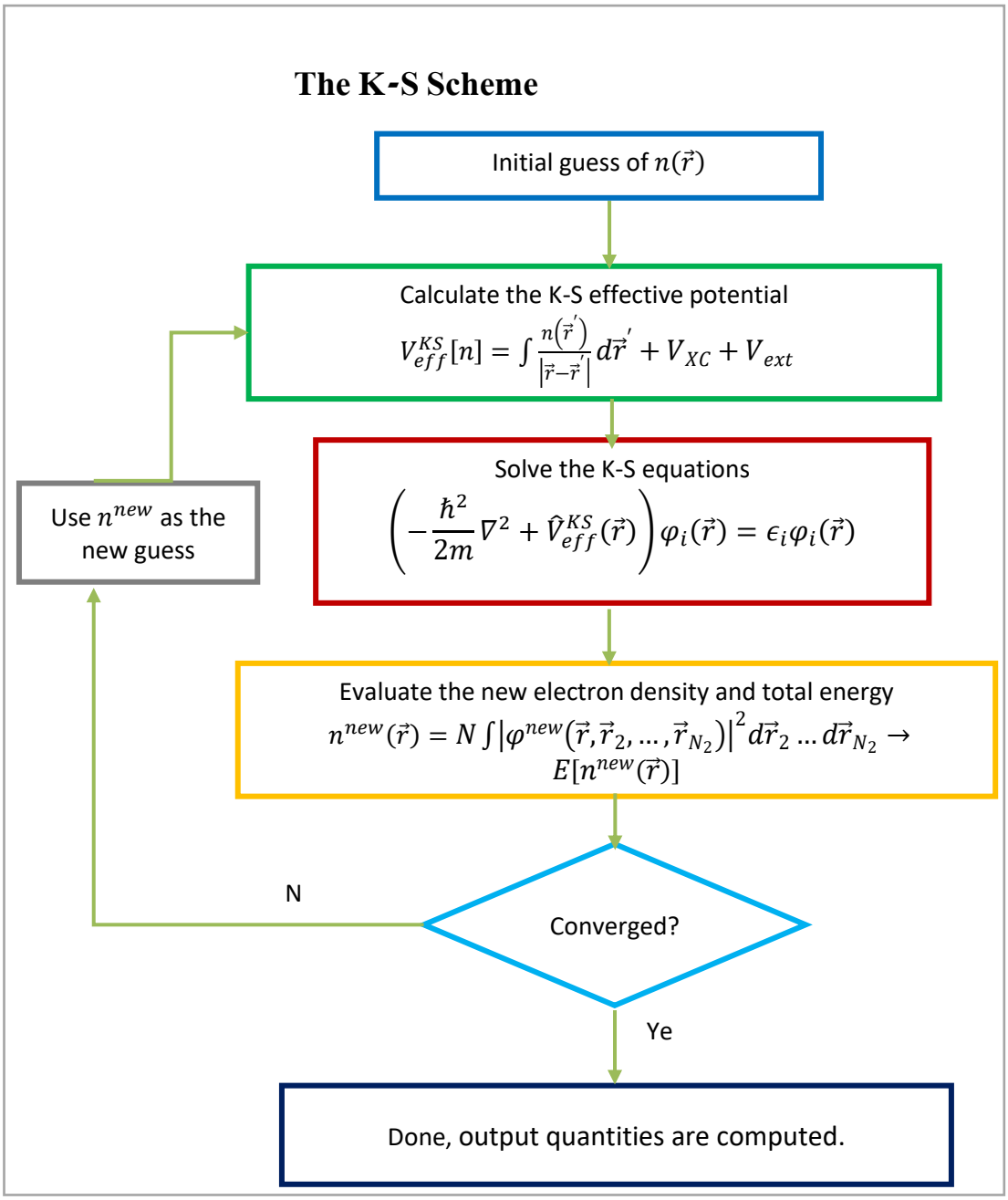

Figure 14 - A flow chart of the iteration scheme. At first, an initial guess for the electron density, $\boldsymbol{n(\vec{r})}$, is assumed and used for the calculation of $\boldsymbol{\hat{V}_{eff}}$, meaning

diagonalization of the K-S equations which evaluates $\boldsymbol{n}(\vec{\boldsymbol{r}})$ and $\boldsymbol{E}$. As long as the convergence criterion is not fulfilled, the numerical procedure continues with the last $\boldsymbol{n}(\vec{\boldsymbol{r}})$ instead of the initial guess. Finally, after the criterion is satisfied, various output quantities are computed using the convergence results.

4.5.5 Physical properties that can be calculated using DFT

DFT finds more and more extensive application in chemistry and materials science for interpretation and prediction of complex system behavior at the atomic scale. The total energy that is discussed in the chapters above is the sum of eigenvalues (energies of the individual independent particles). Usually, the total energy of a system is subdivided into kinetic energies of all particles and potential energies of the interactions between them, where the later are most often limited to the Coulomb interactions only. So, "zero energy" corresponds to the case where all the terms are zero. The kinetic energy is zero when velocity is zero, while the Coulomb interaction energy is zero when particles are infinitely separated from each other. Thus, the "zero energy" corresponds to the case where all the particles are infinitely far away from each other and are not moving. This is essentially a reference state that does not exist.

Specifically, DFT calculation methods are applied for predicting stable systems and material's mechanical and electronic parameters by using the total energy. Examples of current DFT applications include the study of phase transformation behavior, for example in oxides, magnetic and electrical behavior in various types of materials: semiconductors, metals, etc. By applying DFT one can derive both structural and electronic properties. For example, from the structural properties, one can derive the lattice parameter and, thus, the predicted XRD pattern.

It has also been shown that DFT provides good predictions of mechanical properties such as Young modulus,[73] vibrational properties such as phonons[74] and sound velocity,[75] interface stability between two phases or interface energy,[76] etc.. This means that one can predict various response functions, e.g. spectroscopic information derived from the above properties.

For electronic calculations, one can derive magnetic and electrical polarization, effective masses, the shape of optical spectra, bandgap and band structure, and total

energy differences; the latter can lead to thermodynamic properties depending on the choice of the proper reference states. [71]

4.5.6 Calculation of atomic vibrations

Every system of atoms at non-zero temperature vibrates around its equilibrium position, forming the lattice normal vibrational modes. Here, we will treat them from a classical point-of-view. Let us consider a diatomic molecule with a bond length R and equilibrium bond length R_0. The potential of such a molecule, $V(R)$, depends on the deviation from the equilibrium bond length. The *harmonic approximation* applies a 2nd-order Taylor expansion for the molecular potential around R_0 yielding:

$$V(R) \approx V_0 + \left.\frac{\partial V}{\partial R}\right|_{R=R_0} (R - R_0) + \frac{1}{2}\left.\frac{\partial^2 V}{\partial R^2}\right|_{R=R_0} (R - R_0)^2 \qquad (49)$$

Since the minimal potential energy is obtained for $R = R_0$, we can consider the second term, which is the force acting at equilibrium state, to be zero,[77] and the expression reduces to

$$V(R) \approx V_0 + \frac{1}{2}\left.\frac{\partial^2 V}{\partial R^2}\right|_{R=R_0} (R - R_0)^2 \qquad (50)$$

where $\frac{1}{2}\left.\frac{\partial^2 V}{\partial R^2}\right|_{R=R_0}$ is the "spring constant" of the molecule. Let us define the lattice site coordinates of N atoms by a single vector with 3N components: $\vec{r} = (\vec{r}_1, \vec{r}_2, \dots, \vec{r}_{3N})$. Considering the deviations from equilibrium positions by defining new coordinates $\vec{x} = \vec{r} - \vec{r}_0$, equation 50 gets the following form [78]

$$V(\vec{x}) \approx V_0 + \frac{1}{2}\sum_{i=1}^{3N}\sum_{j=1}^{3N} \left.\frac{\partial^2 V}{\partial x_i \partial x_j}\right|_{x=0} x_i \cdot x_j \qquad (51)$$

The "spring constant" in equation 51, $H_{ij} = \sum_{i=1}^{3N}\sum_{j=1}^{3N} \left.\frac{\partial^2 V}{\partial x_i \partial x_j}\right|_{x=0}$, is called the *Hessian matrix*.[79] Here H_{ij} describes the local "curvature" of the energy surface for variations of many atom positions. The equation of motion for each atom located at r_i is

$$\vec{F}_i = m_i \frac{\partial^2 x_i}{dt^2} \qquad (52)$$

and the force acting on each atom that is diverted from the equilibrium position is:

$$\vec{F}_i = -\frac{\partial V}{\partial x_i} = -H_{ik}x_k \tag{53}$$

Newton equation then yields:

$$\frac{\partial^2 x_i}{dt^2} = -H'_{ik}x_k \ ; \quad H'_{ik} = \frac{H_{ik}}{m_i} \tag{54}$$

where H'_{ik} is the mass-weighted Hessian matrix. Assuming that x_i undergo some form of sinusoidal time evolution of the form:

$$x_i(t) = x_i(0)\cos(\omega t) \tag{55}$$

and substituting this into the Newton equations yields a matrix eigenvalue equation

$$\omega^2 x_i = -H'_{ik}x_k \tag{56}$$

The eigenvalues of this equation are the squares of the so-called normal mode vibrational frequencies of the atoms in a solid-state system.

To perform a normal-mode analysis for a solid-state system, one should produce the mass-weighted Hessian matrix, and then find the non-zero eigenvalues. In DFT, we have the ability to calculate the Hessian matrix by deflecting each atom in a small increment *dx* in a specific direction, and to calculate the forces in the deviation direction (potential gradient).

$$H_{ik} = \frac{\left.\frac{\partial V}{\partial x_i}\right|_{dx=dx_k} - \left.\frac{\partial V}{\partial x_i}\right|_{dx=-dx_k}}{dx_k} \tag{57}$$

It should be noted that, if such analysis was performed for atomic configurations corresponding to a transition state (discussed in 4.4.3.2), then $3N-1$ of the ω_j^2 values should have become positive and one of the frequencies would become negative. The eigenvector corresponding to the negative eigenvalue of the mass-weighted Hessian points toward a very important direction, which is diffusion trajectory.

4.5.7 Exchange-Correlation functionals

As shown in Section 4.5.3.2, 4.5.3.1, and 4.5.4, the exchange-correlation energy contains unknown information. A central goal of DFT is to find the ground-state energy of electrons in solids. Implementing this accurately for any configuration of nuclei would provide many basic properties of solids and their structure. The

approximations made to the exchange-correlation potential can be termed in a hierarchy that is sometimes referred to as *Jacob's ladder*, extending from very simple through very complex functionals. [80] The lowest "rung" of this ladder include contributions to the energy that are is determined by the 3D local density, $n(\vec{r})$, solely. Higher "rungs" incorporate increasingly complex ingredients comprising operators of the electron density, such as $\nabla n(\vec{r})$ and $\nabla^2 n(\vec{r})^2/8n(\vec{r})$ or the K-S orbitals. Here we will introduce three common approaches; some of them have been used at this work.

4.5.7.1 The Local Density approximation

The first rung in Jacob's ladder, the simplest potential, is the local density approximation (LDA). Here, the exchange-correlation term is considered to be identical to that of a homogeneous electron gas.[81] The exchange-correlation energy is expressed as:

$$E_{XC}^{LDA}[n(\vec{r})] = \int n(\vec{r})\varepsilon_{XC}\big(n(\vec{r})\big)d\vec{r} \qquad (58)$$

where the electron density is given per unit volume, and the energy density is per particle. Surprisingly, the LDA has proved to be successful, even when applied for systems that are quite different from the state of an electron gas. Although this method demands the lowest computational cost and can provide accurate results for many cases, it is inaccurate for systems with localized electrons, and the appearance of new and more accurate methods leads this method to be rarely used today.[82] Note that K-S equations do not take into account the spin of the electron. One can consider it by including the spin into the definition of the electron density, yielding the local spin density approximation, LSDA, which looks more complicated than the spinless case of LDA.

4.5.7.2 Generalized gradient approximation functionals

The subsequent rung includes generalized gradient approximations (GGAs), which are formulas that utilize both the density, $n(\vec{r})$, and its gradient, $\vec{\nabla}n(r)$, at each point in the real space.

$$E_{XC}^{GGA}\big[n(\vec{r}), \vec{\nabla}n(\vec{r})\big] = \int f\big[n(\vec{r}), \vec{\nabla}n(\vec{r})\big]d\vec{r} \qquad (59)$$

The GGA is very common, since it represents a well-balanced compromise between accuracy and computational efficiency; yet, GGA functionals are computationally more demanding than LDA. [83] Universal GGAs, such as GGA-Pedrew-Burke-Ernzerhof (GGA-PBE), operate for a wide range of systems, however with limited accuracy. This limitation may be caused by the functional form of GGAs. The GGA-PBE can be described by two terms separating the exchange and the correlation contributions in the following form

$$E_{XC}^{PBE}\left[n(\vec{r}),\vec{\nabla}n(\vec{r})\right] = E_{X}^{PBE}\left[n(\vec{r}),\vec{\nabla}n(\vec{r})\right] + E_{C}^{PBE}\left[n(\vec{r}),\vec{\nabla}n(\vec{r})\right] \qquad (60)$$

One approach is to devise GGA functionals that are specialized for certain classes of compounds. For instance, the GGA-Perdew-Burke-Ernzerhof-solid (GGA-PBEsol) functional is designed for the solid-state in particular. GGA-PBEsol recovers the original gradient expansion for exchange, denoted as μ, and its correlation component is adjusted to reproduce jellium surface energies more accurately than does PBE. PBEsol has the same analytical form as PBE with only two differences. The PBE GGA can be adapted to solids and surfaces by changing the exchange as well as the correlation gradient coefficient. The reduced sensitivity of PBEsol to the gradient compared to PBE improves its ability to yield better lattice constants than PBE in solid system calculations.[84,85] Thus, PBEsol is better for systems with “slowly varying” densities, i.e. solids.[78]

4.5.8 Applications for the solid state

Apart from the choice of a specific exchange correlation functional, application of DFT for solids requires additional steps. For example, changing the solution space (e.g. planewaves) or considering defects, charged systems, or instabilities, etc.

The first step in DFT calculations for crystalline solids, which consist of a large number of nuclei and electrons, is to represent the large number of electrons by a *pseudopotential*. In this approach the core electronic states are represented by a pseudopotential, and the valence electrons are described by pseudo-wavefunctions with fewer nodes. Manual “smoothing” of the potential function near the core of the nucleus makes the calculations easier. This allows representation of the pseudo-wavefunctions by significantly fewer Fourier modes, which makes plane-wave basis

sets practical to use. Such approximation can be applied because of the small contribution of the core electrons to inter-atomic bonding, thus considering their screening effect on the nuclei. The case of periodic crystals is treated applying periodic boundary conditions on unit cells. In addition, the reciprocal lattice is represented by dividing the Brillouin zone into a *k*-point mesh. This enables numerical solution of the K-S equation. Two common pseudopotentials schemes are norm-conserving: the ultrasoft and the projector-augmented wave (PAW). The later used in this work.

In the framework of periodic boundary conditions we sometimes reduce the bulk into a supercell, which is a periodic extension of a single unit cell. Supercells allow us to control the concertation of defects in our system and to diminish interactions between neighboring point defects. To facilitate the calculations, the wave functions and lattice vectors are transformed from the real to the reciprocal space, and projected onto the first Brillouin zone. Based on the symmetry of the lattice, we further reach at the irreducible Brillouin zone without losing any information. Then, the irreducible Brillouin zone is sampled with discrete *k*-points, and the calculations are implemented by integration over them. To solve the K-S equations under these conditions, a basis set of plane-wave expansion is used to represent the K-S orbitals φ_i. These plane-waves are already periodic solutions and are Fourier-transformed into the reciprocal space. Practically, infinite expansion of plane-waves cannot be used; therefore, an energy cutoff is introduced which effectively limits the number of plane-waves that are considered in practice. Another numerical problem arises from the sharp drop of charge densities near the Fermi level at 0 K. A smearing method is then applied, by introducing an imaginary, effective temperature in the system, and then cancel its effect. The common smearing schemes are Gaussian,[86] Fermi,[87] Methfessel-Paxton[88] and tetrahedron method with Blöchl corrections.[89]

4.5.8.1 Spin-Orbit Coupling

There are several approaches to improve the accuracy of the calculation using more accurate XC functionals, including relativistic corrections and spin-orbit coupling (SOC). SOC shifts the band edge positions and significantly reduces the magnitude of the band gap.[90] Basically, the significance of SOC increases with the atomic number, Z. In cases of light elements SOC can be neglected However, for

specific properties, SOC might be important even for systems containing light elements, such as graphite. In second-row transition metals and heavier elements, but also for some lighter elements, SOC is essential to reproduce correctly the electronic structure of materials. For heavier elements, in general, the SOC becomes as important for structural properties as for electronic properties. For bulk structures, SOC should be considered when heavy elements are present, such as late *d*-metals and *f*-metals.

4.5.9 Computational tools commonly used for DFT calculations

There are several different software packages for performing DFT simulations. Most packages focus on modeling either solids (periodic boundary conditions) or molecules (isolated boundary conditions). The most common ones for solid-state calculations are VASP, [91] Quantum Espresso, [92] ABINIT, [93] and GPAW. [94] Some of the packages widely used for isolated systems are Gaussian, NWChem, [95] and GAMESS. [96] Some of these packages can be used for both solids and molecules. In this section, we will describe in general the differences between some of these tools and their advantages and disadvantages.

When dealing with computational tools for DFT calculations there are two high-level distinctions used: time-dependent vs. static methods, and periodic-boundary conditions vs. non-periodic or isolated systems.[97] The latter turns out to be, actually, a distinction between computational quantum "physics" and “chemistry". Practically, the term "simulation" refer to computational methods that model dynamics and the progression of some physical quantities with time, whereas the term "calculations" refer to computations that do not involve time explicitly, such as direct calculations of thermodynamic quantities.

Non-periodic quantum dynamics simulations using DFT are less common than static DFT calculations, but are probably growing in prevalence. Methods like TD-DFT for non-periodic systems can be performed using many standard quantum chemistry packages, including GAMESS, [96] which is (available at http://www.msg.chem.iastate.edu/gamess/). The GAMESS package is mostly used to run static DFT calculations for isolated systems.

In periodic systems, a commonly used DFT-based dynamics method is Car-Parrinello Molecular Dynamics (CPMD). CPMD is not used for non-periodic systems. A widely used open-source package for CPMD and other periodic boundary condition DFT electronic structure methods is Quantum Espresso. [92] One of the benefits of Quantum Espresso as a CPMD tool is that it is available for free (at http://www.quantum-espresso.org/). A popular non-free code for the type of CPMD calculations is the Vienna *ab-initio* simulation package (VASP). [91] Both codes, Quantum Espresso and VASP, can run a variety of static DFT calculations as well.

The common CPMD-based tool VASP is used in this work. [91] VASP solves the K-S equations with periodic boundary conditions and applies the PAW method together with plane-wave basis to expand the K-S orbitals.

5 Summary and Research Goals

The Pb-Te-Ag system has attracted scientific interest owing to its potential of enhanced TE performance due to formation of Ag_2Te precipitates. The dependence of the Ag-rich precipitates distribution and their temporal evolution on the Ag concentration and heat treatment time has been investigated, as well as the diffusion-based growth rate of Ag-rich precipitates. We are interested in studying the diffusion rate of Ag in PbTe and its implications on microstructure evolution and the resulting TE coefficients.

The goals of this research are: (1) to quantitatively evaluate diffusion coefficients of Ag-atoms in PbTe for different temperatures from first-principles; and (2) to experimentally measure the effects of microstructure evolution, resulting from Ag-diffusion, on the TE coefficients of Ag-alloyed PbTe. The latter include thermal and electrical conductivities and Seebeck coefficients.

Finally, both computational and experimental aspects will be compared to each other. Achieving this knowledge will help us improve the TE performance of PbTe-compounds.

6 Research Methods

6.1 Synthesis of $Ag_xPb_{0.5-x}Te_{0.5}$ compounds

Samples were prepared based on the pseudo-binary PbTe-Ag_2Te phase diagram [32,98] and previous experimental routines done in our group. [13,27,28] Pb (99.96%, Riedel-de Haën®), Te (99.99%, STREM CHEMICALS®), and Ag (99.999%, Alfa Aesar®) flakes were weighted and placed in quartz tubes in the stoichiometric ratios of (50-x):50:x, respectively, with x=0, 1, 2, 3 and 4. The quartz tubes were evacuated, sealed, and placed inside a furnace.

To avoid oxidation and evaporation of Te,[99] the samples were melted in 140 torr Ar-7% H_2 gas mixture in sealed quartz tubes at 1000 °C for 6 h with mixing every 1 h, followed by annealing at 700 °C for 72 h to ensure the homogeneity at the PbTe single-phase regime. Finally, the samples (expected to be super-saturated PbTe-based solid solutions) were quenched in an iced-water bath as shown in Figure 15.

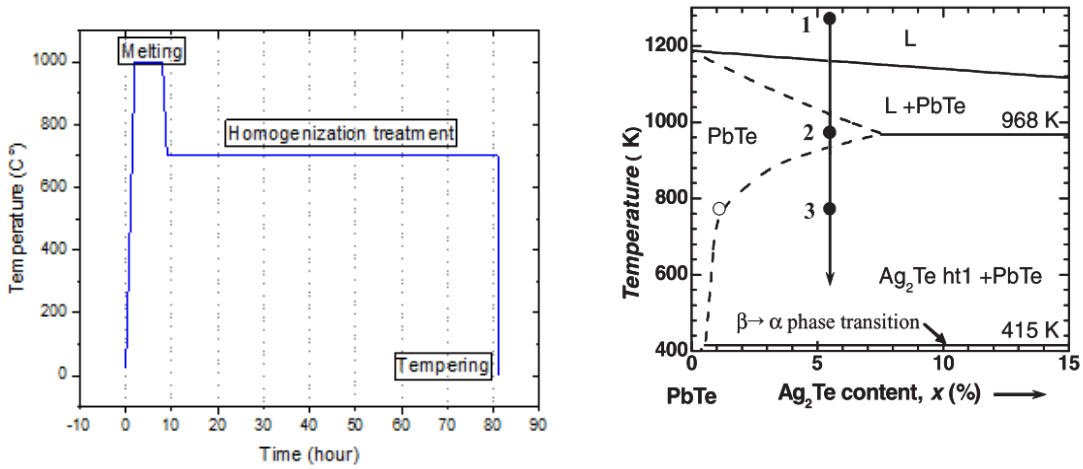

Figure 15 - Materials synthesis process based mainly on the pseudo-binary PbTe-Ag_2Te phase diagram[32,98,31]

In this work, we divided the experimental section into two different types of experiments, and thus two types of samples. X-ray powder diffraction samples and in-situ samples. In the following sections, we will present how the samples are prepared for the two different types of experiments.

6.1.1 X-ray powder diffraction samples

We divide our X-ray measurements into two sections: aging experiments and concentration experiments. Both sections will help us monitor the effects of Ag-alloying on the phases that appear and grow in the PbTe system and determine the rate of changes in the microstructure under aging treatments. The cast ingots were ground into powder by agate pestle and mortar down to an average particle diameter of ca. 54 μm.

For the aging experiments, powders of $Ag_{0.04}Te_{0.5}Pb_{0.46}$ and $Ag_{0.02}Te_{0.5}Pb_{0.48}$ were put into mold and cold-pressed (CP) under 3-ton pressure. The $Ag_{0.04}Te_{0.5}Pb_{0.46}$ cold-pressed samples were placed in quartz tubes and aged at 380 °C for different durations to encourage nucleation of Ag-rich precipitates (High Temperature – HT). The $Ag_{0.02}Te_{0.5}Pb_{0.48}$ samples were aged at HT and then at 300 °C (Low Temperature – LT). Finally, all of these aged samples quenched in iced water and measured by XRD.

For the concentration experiment, powders from as-cast (AC) $Ag_xPb_{0.5-x}Te_{0.5}$ ingots with different x-values were measured by XRD. The powders were mixed with 40 wt. % Ni powder as a reference, since it exhibits diffraction peaks located far from the PbTe peaks. Adding a reference material to the samples helps us compensate for the deviations in peak locations that may arise for different XRD scans. In this way, calculation of the lattice parameters change upon aging should be more accurate.

6.1.2 In-situ samples

Based on previous work done in our group, [13,27,28] the cast ingots were hot-pressed at 650 °C within the single-phase region in a 12.5 mm diameter die at 45 MPa for 15 min. under Ar-7% H_2 atmosphere, followed by iced-water quenching.

6.2 Microstructure analysis and physical property measurements

6.2.1 Scanning electron microscopy

Characterization of the materials' surface was carried out using a Zeiss ® *Ultra Plus* high-resolution scanning electron microscope (HR-SEM) equipped with 80 mm^2 active area Oxford® SDD EDS detector with an energy resolution of 127 eV, equipped

with a Schottky field-emission electron gun. The micrographs presented in this study were taken with secondary and backscattered electron detectors.

6.2.2 X-ray diffraction

Phase identification and lattice parameter analysis were performed applying a Rigaku *SmartLab* X-ray diffractometer, which includes a parallel-beam with high-resolution Ge(220)x2 bounce monochromator optics, a high-speed 1D silicon strip detector (D/teX), [100] and a Cu K_α X-ray source (1.540593 Å). Measurements were taken in an angular range of 2θ = 20° through 100° with a step size of 0.05° and scan rate of 5°/min.

To monitor the change in location of the XRD peaks of the system during the aging process, we added nickel powder to the ground PbTe-samples as a reference. The reason for selection of Ni is that its diffraction peaks are located far from the PbTe peaks. The initial fit is based on the Ni peak at around 44.5°. We added 40 wt. % Ni powder, a high amount that will allow accurate determination of the location of the peaks.

6.2.2.1 Rietveld analysis

Once the final phases were identified, Rietveld refinement was carried out using the GSAS-II software.[101,102] The Rietveld method is a powerful method for extracting detailed crystal structural information from X-ray powder diffraction data. In Rietveld analysis, we fit a model describing how the atoms are ordered in the cell to the experimental data. If the model is correct, then it predicts what the "true" intensity values should be.

Refinement conditions were: angle limit of 22°-99.97°, "constraint searching frac" (All:0:Scale), 10 parameters for background correction, initial phase fraction for Ni, PbTe, and $AgTe_3$ to be 0.7, 0.2, and 0.1, respectively; the preferred orientation calculation method was implemented by spherical harmonics for all phases, and a μStrain parameter was also refined for all phases.

6.3 Density measurements

Determination of an irregularly shaped object is done using Archimedes' principle. An object immersed in a fluid (liquid or gas) is buoyed up by a force equals

to the weight of the fluid that is displaced. An advantage of this method is its ability to consider the porosity of the sample. The sample's bulk density can be determined using

$$B = \frac{D\rho_f}{S - M} \tag{61}$$

where D [g] is the weight of the dried sample, ρ_f [g cm^{-3}] is the fluid density at a given temperature, S [g] is the weight of the sample when soaked in water, M [g] is the "moist" weight of the sample, and B[g cm^{-3}] is the bulk density. The method was adapted from the international ASTM-C373-88 standard.[103]

6.4 Thermoelectric measurements

A unique aspect of this study is *in-situ* TE measurements for Ag- supersaturated PbTe specimens that are heated at certain temperatures for different times to track the onset of nucleation of Ag_2Te-precipitates and their influence on TE properties. The TE measurements utilized in this study are divided into two main categories: electrical and thermal measurements. The electrical measurements were done using the Seebeck Analyser (SBA) and the thermal measurements were done applying the laser flash analysis (LFA).

6.4.1 Electrical Analysis

All of our measurements are done applying the Netzsch SBA-458 *Nemesis* ® system to measure the electrical conductivity and the Seebeck coefficient of bulk samples. All measurements are carried out in a purged Ar atmosphere.

6.4.1.1 Principle of operation

The measurement setup, see Figure 16.(a), allows a simple way for determination of the Seebeck coefficient of a sample, since it can be reduced to the configuration shown in Figure 16.(b).

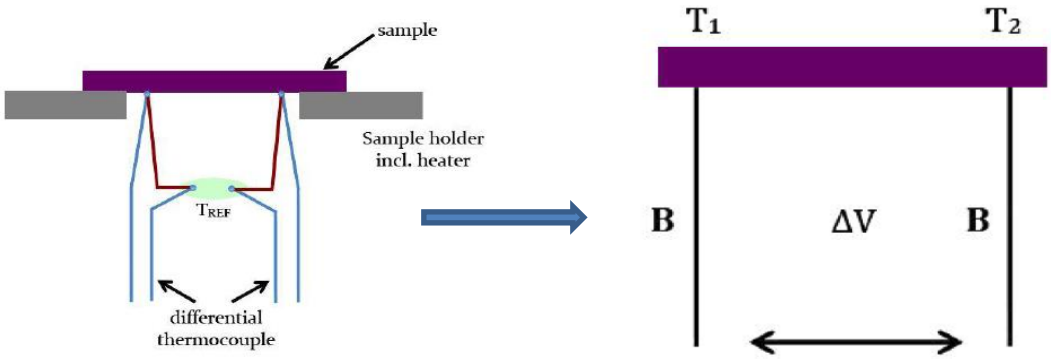

Figure 16 – (a). A schematic description of the principle of Seebeck coefficient measurement which can be reduced **(b)** to a typical configuration for the measurement of the Seebeck coefficient. (taken from Netzsch® official website)

A temperature difference $\Delta T = T_2 - T_1$ is applied by external heaters on the sample and the built-in voltage ΔV is measured. The Seebeck-coefficient of the thermocouple material B (α_{AB}) is known, thus, the Seebeck coefficient of the sample (S_A) is measured.

6.4.1.2 In-situ SBA *m*easurements

In-situ SBA measurements were made by loading a series of single shots during certain time intervals at an aging temperature of 380 °C. The sample is placed on a sample holder inside a chamber surrounded by a furnace. Each of the two opposite edges of the sample is connected to an electrical contact, thermocouple and a microheater. The chamber was evacuated and continuously purged with an Ar inert gas. The entire measurement procedure is fully automatic. The furnace starts to heat and follows a predefined program of temperature steps. The first step is heating at a heating rate of 10 °/min up to 350 °C. When the 350°C temperature step is reached a measurement of the electrical conductivity takes place using the electrical contacts. Subsequently, the two micro heaters generate a temperature difference along the sample and a measurement of the Seebeck coefficient takes place. Such a set of measurements (Electrical conductivity and Seebeck coefficients) takes 15 minutes. At the next step, the sample was heated with a heating rate of 5 °/min up to 380°C. The

program is predefined to apply approximately 170 measurement sets at 380 °C and 380.1 °C alternatively to achieve the desired aging time. Finally, the furnace cools down and the sample is removed.

6.4.2 Thermal analysis

The thermal measurements performed in this study refer to thermal diffusivity and heat capacity. Employing the Netzsch LFA-457 *Microflash* ® apparatus, [104] we directly measure the thermal diffusivity and indirectly measure the heat capacity. The thermal conductivity, κ, of material can be calculated by equation 5. The material's density, $\rho(T)$, has a weak temperature dependence; hence, we neglect the temperature dependence of ρ. The LFA allows us to measure the thermal diffusion directly from the reaction time of the material to a thermal pulse.

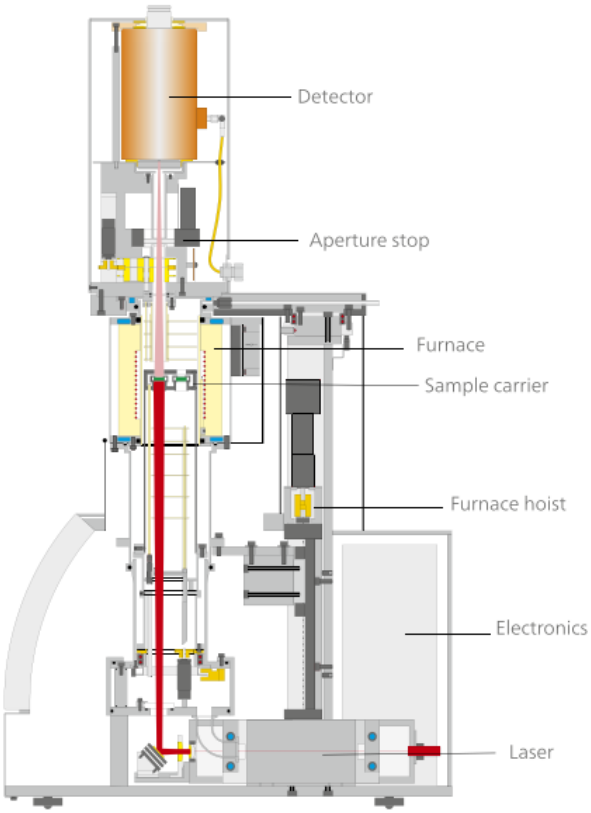

Figure 17 – A schematic description of the LFA apparatus (taken from Netzsch® official manual[104]).

The Netzsch LFA-457 is based on a solid-state pulsed Nd:YAG laser with a wavelength of 1054 nm. Our LFA-457 system properties are:

- Adjustable laser power energy up to 18 J/pulse.
- Two exchangeable furnaces that cover the entire temperature range from -125 °C up to 1100 °C.
- Cooling/heating rates are: 0.01-50 $Kmin^{-1}$.

The system can measure a thermal diffusivity range of 0.01 through 1000 mm^2s^{-1} and a thermal conductivity range of 0.1 through 2000 $Wm^{-1}K^{-1}$.

The laser flash method dates back to studies by Parker et al. in 1961. [105] In carrying out measurement, a surface of plane-parallel sample is heated by a short energy pulse and the resulting temperature change on the other samples' face is then measured with an infrared detector, and a thermocouple placed at the sample's environs measures its absolute temperature, Figure 17. A typical result obtained at such a measurement shown in Figure 18. The higher the sample's thermal diffusivity, the steeper the signal increase and the earlier time to receive a signal.

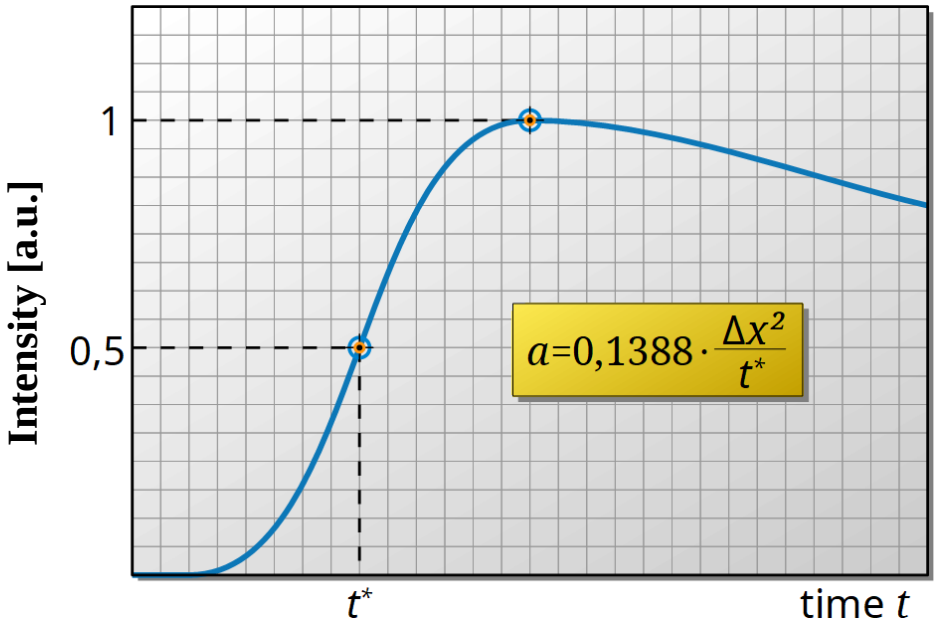

Figure 18 - A typical thermal signal detected from the back face of the sample, allowing to assess the "half-time" rise.

For adiabatic conditions, the thermal diffusivity can be calculated by[105]

$$D = 1.388\frac{l_T^2}{t_{0.5}} \tag{62}$$

Where l_T is the thickness of the measured sample and $t_{0.5}$ is the time required for the output signal to reach 50% intensity.

The heat capacity denotes how much heat needs to be invested to raise the sample's temperature.

$$C_p \equiv \left(\frac{\partial H}{\partial T}\right)_P \tag{63}$$

The heat capacity can be roughly described by

$$C_p = \frac{I}{\Delta T} \tag{64}$$

Were I is the intensity of the heat absorbed by the sample with a temperature rise ΔT. To measure the heat capacity using the LFA, we measure the thermal signal of the material having heat capacity C_p^{mat} and the signal of a reference sample with a known heat capacity, C_p^{REF}. We integrate the two signals obtaining the intensities I^{REF} and I^{mat}. Our calculated intensities obey the ratio

$$\frac{C_p^{mat}}{C_p^{REF}} = \frac{I^{mat}}{I^{REF}} \;\Rightarrow\; C_p^{mat} = C_p^{REF}\frac{I^{mat}}{I^{REF}} \tag{65}$$

This ratio is based on an assumption that both the sample and the reference sample absorb the same heat intensity in each pulse.

6.4.2.1 In-situ LFA measurements

In-situ LFA measurements were made applying the LFA-457 to load a series of single shots at an aging temperature of 380 °C. The sample is placed on a holder inside a chamber surrounded by a furnace. The chamber was evacuated and continuously purged with an Ar inert gas. The furnace starts to heat and follows a predefined program of temperature steps. The first step is heating at 10 °/min up to 350 °C; then, a shot is taken. Such shot measurement prolongs approximately 5 min. At the next step, the sample was heated at 5 °/min up to 380 °C. The program is predefined to apply approximately 170 measurement sets at 380 °C and 380.1 °C alternately to achieve the desired aging time. Finally, the furnace cools down and the sample is removed.

6.5 Computational Methods

In this chapter, we describe the theoretical method for modeling the diffusion process from first-principles. Whereas underlying theory was detailed above, herein we focus on technical parameters applied by VASP.

6.5.1 Optimization

In order to analyze the influence of Ag dopant at rocksalt PbTe system, we build a 2×2×2 supercell and then substitute some of the voids, Pb or Te sites, with Ag. For a 64-atom PbTe supercell, substitution of one atom yields the smallest doping level of 1/64 = 1.56 at. %. An interstitial site occupation yields the smallest doping level of 1/65 = 1.54 at. %. Smaller doping level, which may be obtained by larger supercells, is not as practical as the computation time increases significantly.

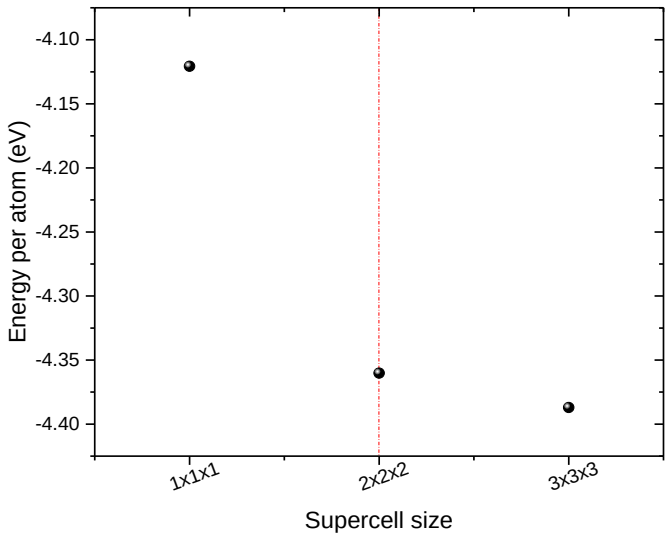

Figure 19 - Examination of the Methfessel-Paxton method convergence for different supercells of Ag-doped PbTe. The dashed red line describes our choice of a 2×2×2 cell that yields total energy that differs by merely 0.01 eV from the 3×3×3 supercell energy.

Figure 19 shows the calculated specific energies (per atom) for a 1×1×1, 2×2×2, and 3×3×3 supercells. The calculated energy difference between 2×2×2 and 3×3×3 supercells differs by merely about 0.01 eV. All calculations in this study were, therefore, performed for a 2×2×2 supercell.

6.5.1.1 Selection of the appropriate functional

No systematic and practical way is known today to converge to the exact density functional.[106] Based on comparison between the following density functionals: LDA, BLYP, PBE, rPBE, AM05, and PBEsol with and without consideration of SOC, we conclude that GGA-PBEsol with SOC is the most accurate way to obtain suitable calculated results of the parameters bandgap, lattice parameters, and density. All the results obtained by us are given in Table III.

6.5.1.2 k-mesh density

The first step in determination the appropriate cell geometry and size is structure relaxation calculation, which yields the lowest energy. Recent work done by Joseph et al. [74,75] in our group for PbTe examined the convergence for different *k*-points between the lowest density of 0.563 $Å^{-1}$, which is equivalent to a 3×3×3 Monkhorst-Pack *k*-point grid, and the highest density of 0.068 $Å^{-1}$ corresponds to 25×25×25 *k*-point grid. To calculate the electronic and elastic properties for the different doping levels Joseph et al. applied a finer k-mesh grid with a density around 0.1 $Å^{-1}$. Since the PbTe unit cell has the high symmetry of $Fm\bar{3}m$, the total number symmetrically <u>unique</u> points is much lower, for example, the 25×25×25 grid which has a total of 15,625 *k*-points yields eventually only 455 symmetrically unique *k*-points. The requested k-spacing is 0.0956592 $Å^{-1}$, which leads to a 6×6×6 mesh for the tetrahedron method and 0.118 per Angstrom which leads to a 5×5×5 mesh for Methfessel-Paxton smearing with a width of 0.126563 eV. The former is used for diffusion coefficient calculations, and the latter is used for lattice parameter calculation.

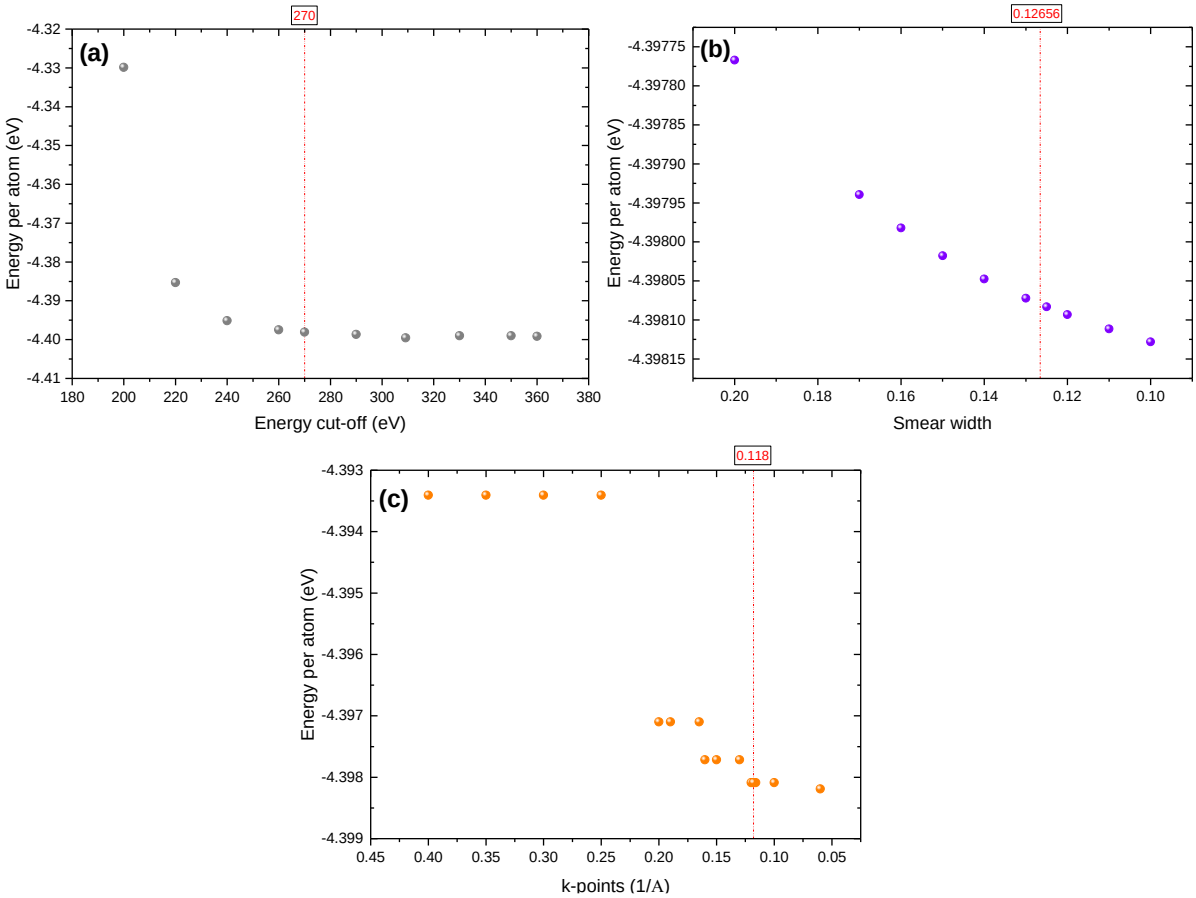

Figure 20- Examination of the Methfessel-Paxton method convergence for different **(a)** cut-off energies, **(b)** smearing widths, and **(c)** *k*-points calculated for different ranges. The initial parameters are: **(a)** cut-off energy of 270 eV, **(b)** smearing width of 0.126563 eV, and **(c)** *k*-mesh grid of 0.118 $Å^{-1}$, which leads to a 5x5x5 mesh also plotted with red vertical line.

6.5.1.3 Applying spin-orbit coupling (SOC)

Previous studies have shown the importance of the SOC for band structure calculations of PbTe due to the relatively heavy Pb atoms. [107–109] The shape of the energy bands has little influence and the main effect of the SOC is on the bandgap itself. [108,110,111] Previous study performed in our group indicates that the Seebeck coefficient is more sensitive to SOC than electrical conductivity does, which depends on the shape of the energy bands more significantly.[74] For our needs in this study, we decide not to incorporate SOC for frequency calculations as the computation time

increases significantly. However, SOC was considered for activation energy calculations and bandgap structure calculations.

6.5.2 Activation energy barrier

It should be noted that the absolute values of calculated energies are rarely used in DFT applications. More relevant for DFT calculations are reaction energies and relative stabilities, which are more accurate due to error cancellation. The largest errors of approximated exchange-correlation functionals are typically in atoms and cell energies, thus calculation of total energies are include these errors fully. However, reaction energies and energy differences are affected much less. [84]

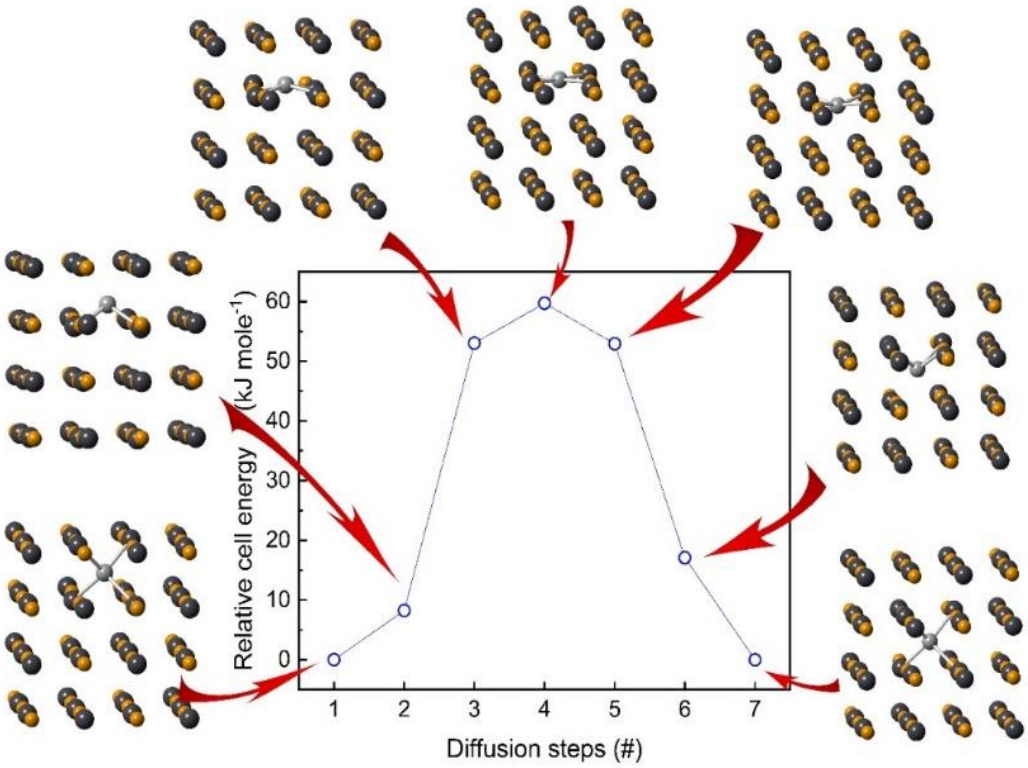

Figure 21 - Evaluation of the activation energy for Ag diffusion in PbTe using the density functional theory (DFT). The relative cell energies are calculated for different steps of the Ag-diffusant (light grey) along the <100> direction. Pb atoms are marked in dark grey and Te atoms in orange. The activation energy is the maximum value of the calculated relative cell energy, and is obtained at the saddle point, step no. 4.

To determine the activation energy for the interstitial diffusion mechanism, the energy invested by the system for one diffusion step is obtained by placing a silver atom in a 2×2×2 PbTe supercell which contains 64 atoms. In this way, we avoid interaction between the other silver impurities placed at the other cells of the periodic system.

Adopting a straight path for diffusion jump is probably a good approximation for cubic PbTe. More elaborate approach would be using the nudged elastic band method without assuming in advance the geometry of diffusion jump. Adding additional degree of freedom may somewhat reduce the diffusion barrier. To simulate the transition state, the diffusion trajectory is divided into seven steps, for which the total energies are calculated. For each of these seven steps, all atoms surrounding the Ag-diffusant are allowed to relax toward their equilibrium positions, where the Ag-atom position is frozen along the diffusion path only. The *relative cell energy* is then calculated for each step, indicating the difference between the total energies calculated for the cells where the diffusant resides at its pertinent and initial positions. The activation energy for diffusion is, accordingly, the maximum relative cell energy. Figure 21 exemplifies the way how we applied the above method for calculating the activation energy for diffusion of Ag in PbTe in the interstitial mechanism.

In addition, to indicate the calculation accuracy compared to experimental data, we apply the DFT calculations with the same parameters for silver diffusion in PbSe as a reference system, and the results of the calculation were compared with experimental results obtained by Fedorovich for PbSe.[16,63]

6.5.3 Pre-exponential diffusion coefficient

The electron-ion interactions were modeled within the PAW[112] formalism and an increased plane-wave cutoff energy of 350 eV. The electronic iteration convergence criterion is 10^{-6} eV using the Normal (blocked Davidson) algorithm and reciprocal space projection operators. The requested *k*-spacing is 0.0956592 $Å^{-1}$ which leads to a 6×6×6 mesh using the tetrahedron method. Our calculations are performed for a 2×2×2 rocksalt PbTe supercell. A Matlab pre-exponential coefficient calculation code, with/without SOC, for the activation energies of PbTe is provided in Appendix I.

7 Results

This chapter covers the experimental and theoretical results acquired in this study and consists of three main sections. The first one reports on microstructure characterization and phase identification. The second one, in-situ TE measurements, includes electrical conductivity, Seebeck coefficient, and thermal conductivity measurements. In the last section we report on calculation of diffusion coefficients, bandgap, and lattice parameters for the Ag-doped PbTe system from first-principles.

7.1 Experimental results

7.1.1 Microstructure analysis

This section presents the microstructure analysis obtained using SEM images that were taken from the 1 at. % Ag-doped PbTe aged samples. We performed SEM analysis for several purposes related to thermal conductivity analysis, given that the latter strongly correlates with the quality of sample preparation. The SEM images show poor synthesis quality of PbTe. The powder does not appear to be fully bonded in the HP process.

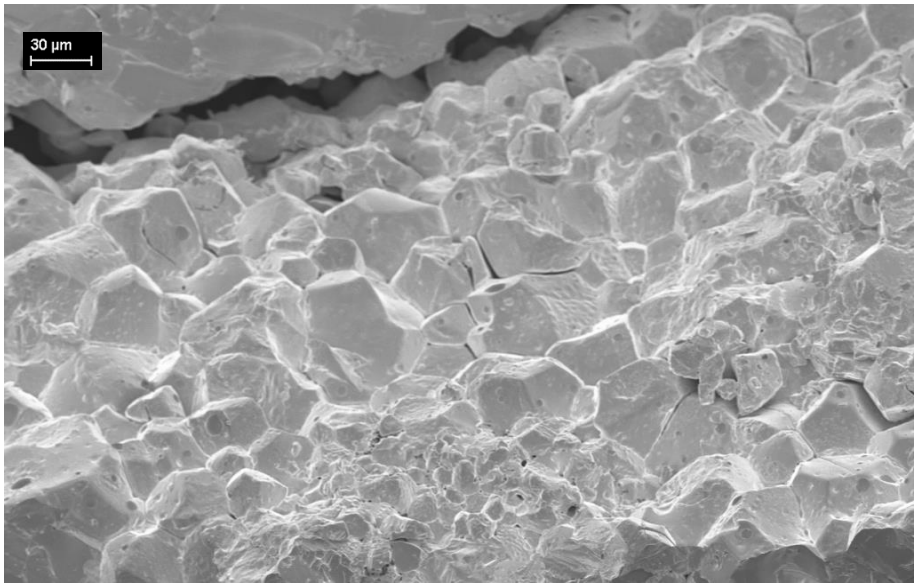

Figure 22 - An in-lens secondary electron micrograph taken from an area of the 1%Ag-doped PbTe AQ sample that was fractured, showing a brittle fracture.

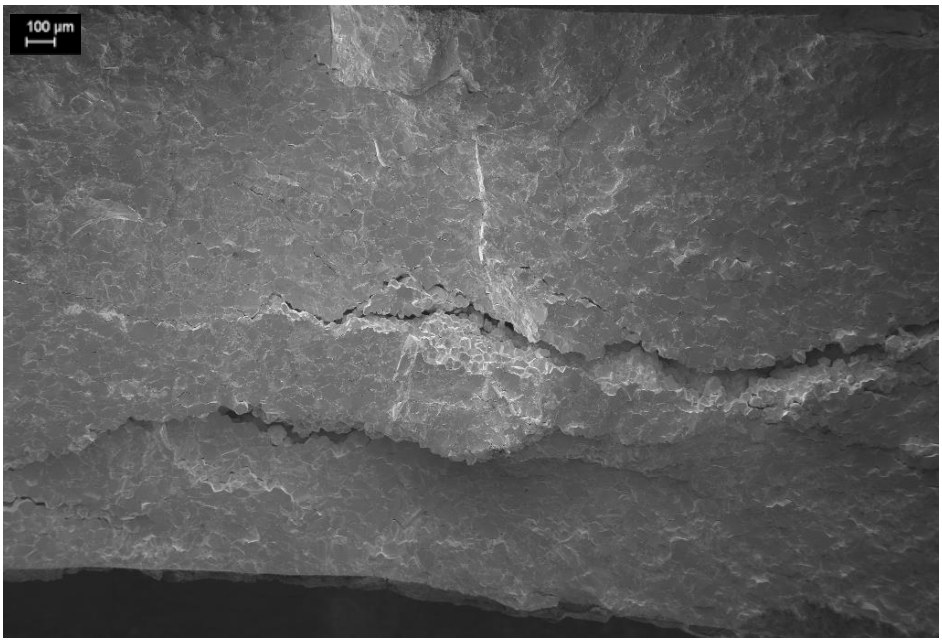

Figure 23 – An in-lens secondary electron micrograph taken from an area of the 1%Ag-doped PbTe AQ sample that was fractured showing that the particles grounded have poor connectivity after the HP process.

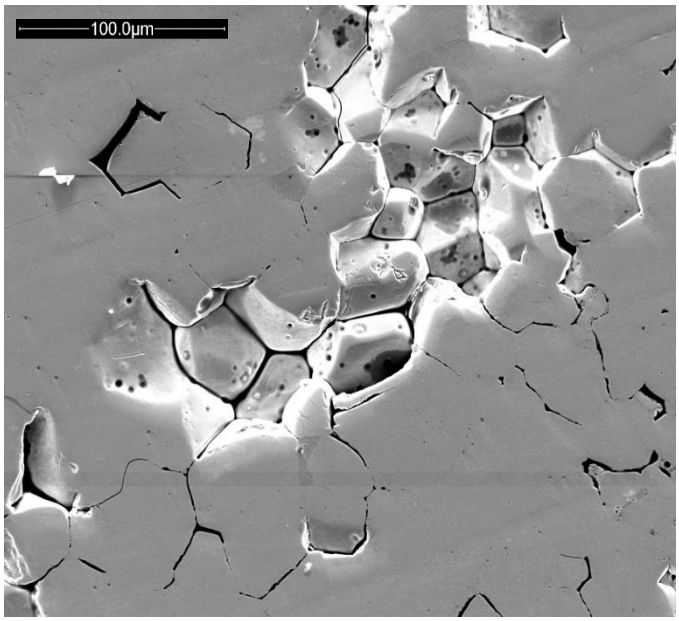

Figure 24 - An in-lens secondary electron micrograph taken from an area of the 1%Ag-doped PbTe AQ sample that was fractured showing that the particles grounded have poor connectivity after the HP process.

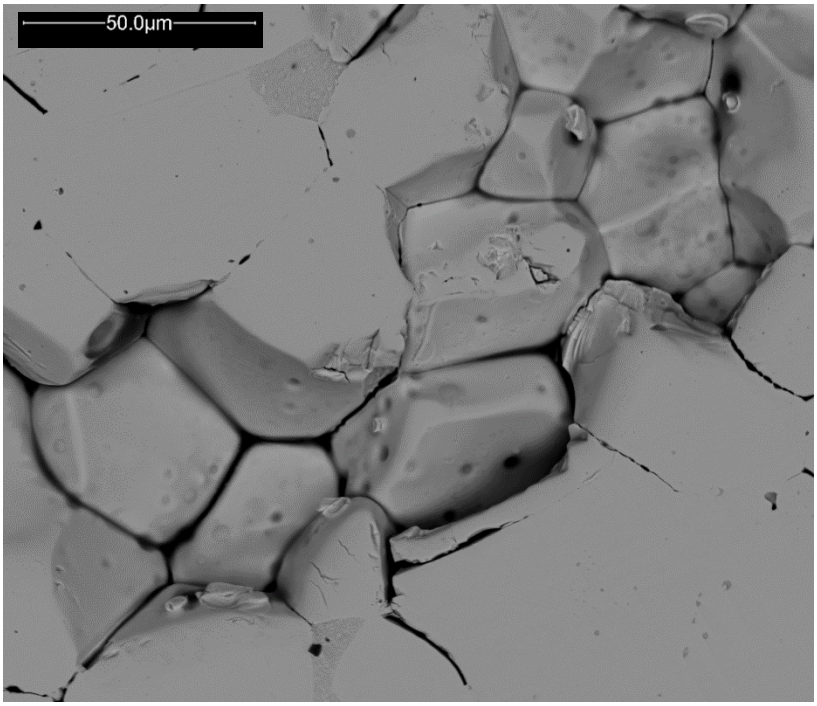

Figure 25 - A back-scattered electron micrograph taken from an area of the 1%Ag-doped PbTe AQ sample that was fractured, showing that the particles grounded have poor connectivity after the HP process with no evidence for additional phases except PbTe.

7.1.1.1 Density measurements

Electrical conductivity strongly depends on the density of the material. To make sure that the changes in electrical conductivity cannot be associated to density but to microstructure and chemistry solely, we performed density measurements for 3 samples of each Ag concentration prepared under the HP conditions discussed in chapter 6.1.2. The results are shown in Figure 26.

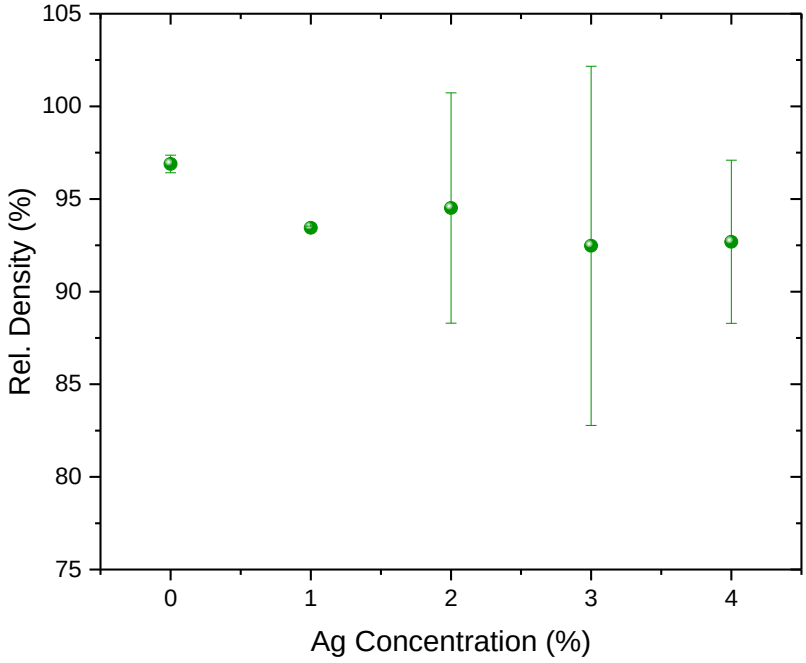

Figure 26 – The samples bulk density measured for different Ag-concentrations, showing an average value of ca. 92 % relative density.

High relative densities (over 90%) are indicated for the samples with small Ag concentrations (below 2 at. %). For the samples with the high Ag concentrations (3 at. % or higher) the density values introduce a high error range with average relative density of 80 %. This low density can be associated with the poor HP process resulting in the microstructures shown in the SEM micrographs.

7.1.2 Phase identification

We performed XRD analysis for the specimens prepared in the multi-stage process, as detailed in chapter 6.2.2, to validate that we obtain the desirable single-phase PbTe. The XRD patterns presented in Figure 27 indicate the existence of single-phase PbTe, Ni (which was added before the XRD measurement as a reference), and two peaks that are suspected to correspond to $AgTe_3$. It is important to note that these three peaks have the same behavior as will be introduced further below, so it is sufficient to focus only on one of these peaks at $\theta \approx 29.2°$, which is the most intensive one.

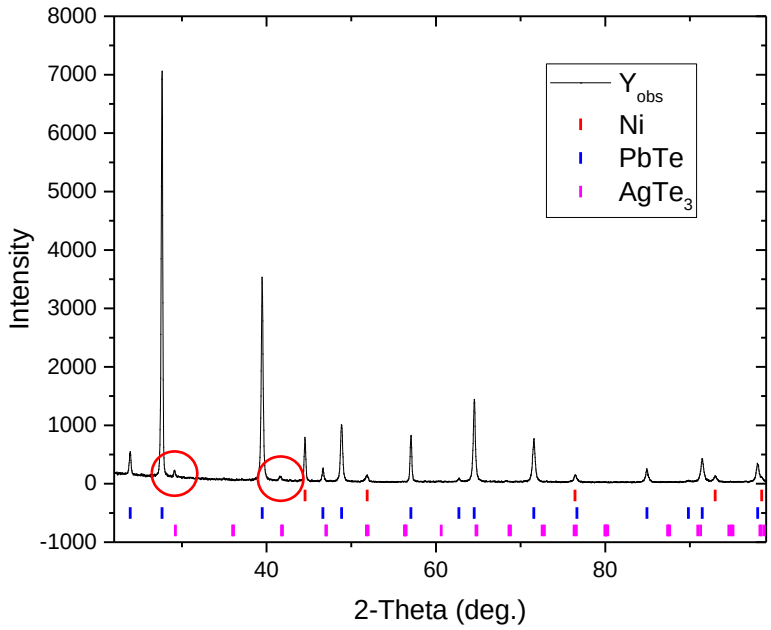

Figure 27 - XRD diffraction of 4 at. % Ag PbTe showing peaks of rock-salt PbTe, Ni (which was added as a reference), and peaks of $AgTe_3$. (Corresponding to PbTe JCPDS number 04-002-0317, Ni JCPDS number 04-010-6148, $AgTe_3$ JCPDS number 04-004-8714)

We are interested in tracking the presence of the low-intensity second-phase $AgTe_3$ peaks, which are almost undetectable in our XRD analysis, and are useful for monitoring the evolution of Ag-based phases (AgTe and Ag_2Te, etc.) in PbTe, whose growth is based on telluride consumption.

7.1.2.1 Dependence of phase evolution on Ag concentration

In this section we will present the experiments described in Chapter 6.1.1, which was divided into two sections, that will help us: (a) to monitor the effects of Ag-alloying on the phases that appear and grow in the PbTe system; and (b) to determine the rate of changes in the microstructure during aging treatments. Figure 28 through Figure 31 show one of the two low-intensity peaks discussed in chapter 7.1.2, and its evolution for different Ag concentrations (Figure 28) and different aging times (the rest of the Figures).

Figure 28 shows that the intensity of these peaks increases with increasing Ag concentration.

Figure 31 shows that for different aging times these two low-intensity peaks appear immediately after the quenching process (or the homogenization treatment) and then disappear after two hours of heat treatment at 380 °C and appear again with lower intensity after 2 h aging. The same trend is observed for 2 at. % Ag doped- PbTe powder at the same aging temperature (380 °C), Figure 29, with decrease of the rate at which this peak vanishes; eventually, it vanishes after 3 h aging. As follows from Figure 30, the peak appears after the quenching process and disappears after 1 h aging at a lower temperature of 300 °C.

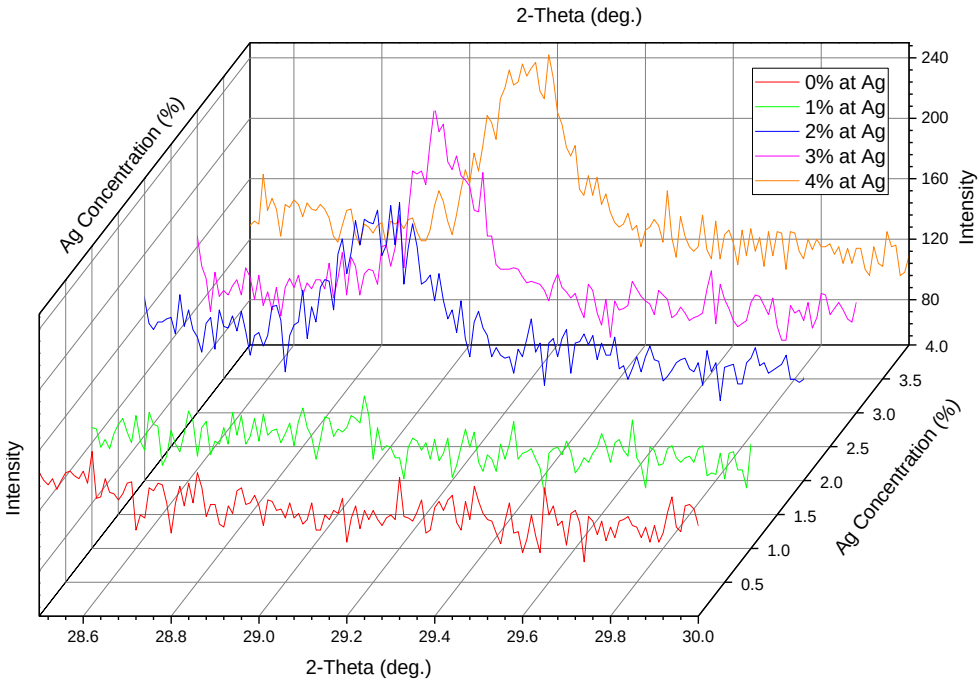

Figure 28 – X-ray diffraction (XRD) spectra collected from the vicinity of the low intensity peak at ~ 29.2° indicated in **Figure 27** of the $Ag_xPb_{0.5-x}Te_{0.5}$ system with the following compositions corresponding to x=0, 0.01, 0.02, 0.03, and 0.04.

7.1.2.2 Dependence of phase evolution on aging time

2 at. % Ag-doped PbTe

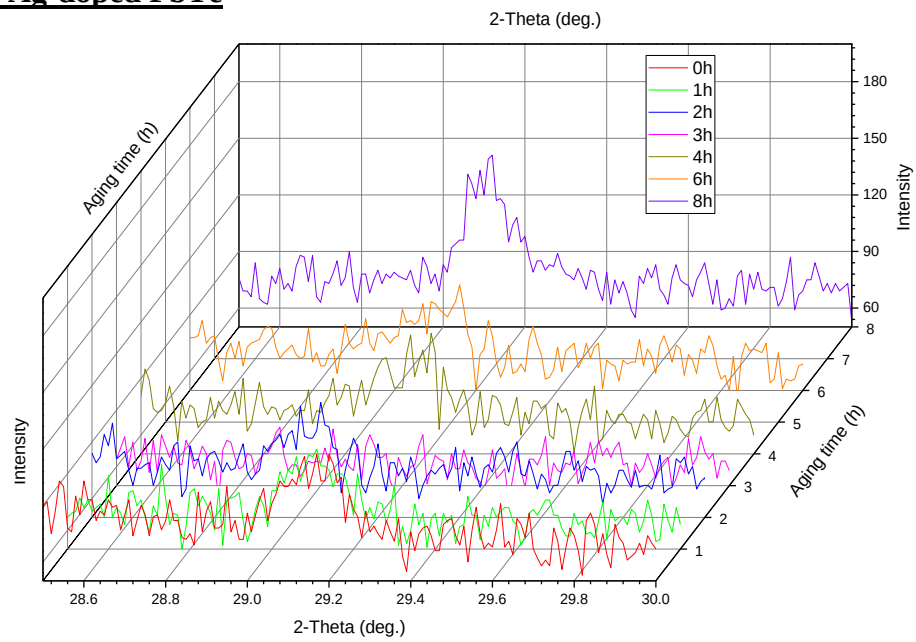

Figure 29 - X-ray diffraction (XRD) spectra collected from the vicinity of the low intensity peak at ~ 29.2° of the $Ag_{0.02}Pb_{0.48}Te_{0.5}$ system after aging at 380 °C for different times.

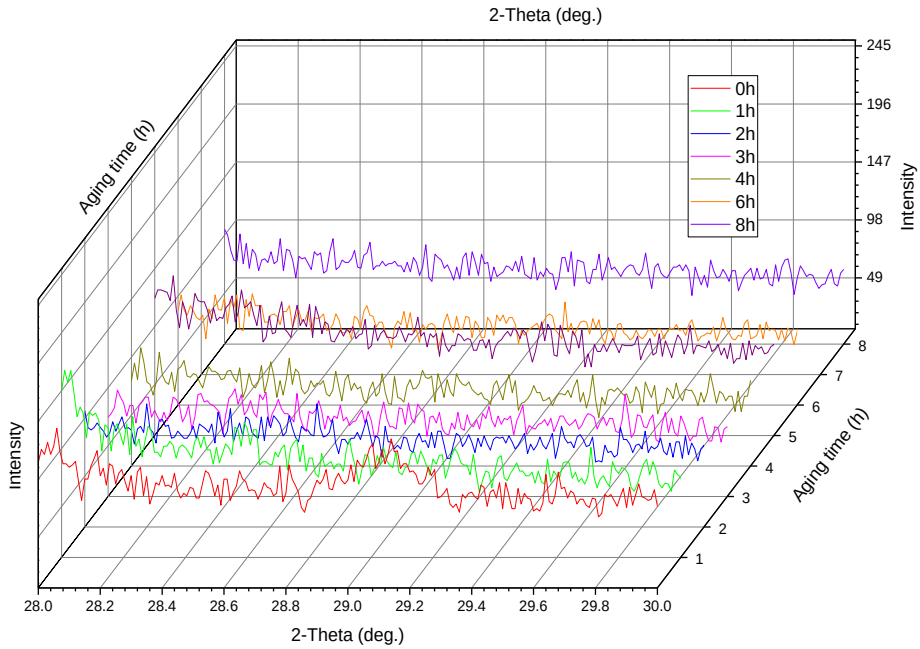

Figure 30 - X-ray diffraction (XRD) spectra collected from the vicinity of the low intensity peak at ~ 29.2° of the $Ag_{0.02}Pb_{0.48}Te_{0.5}$ system after aging at 300 °C for different times.

4%Ag-doped PbTe

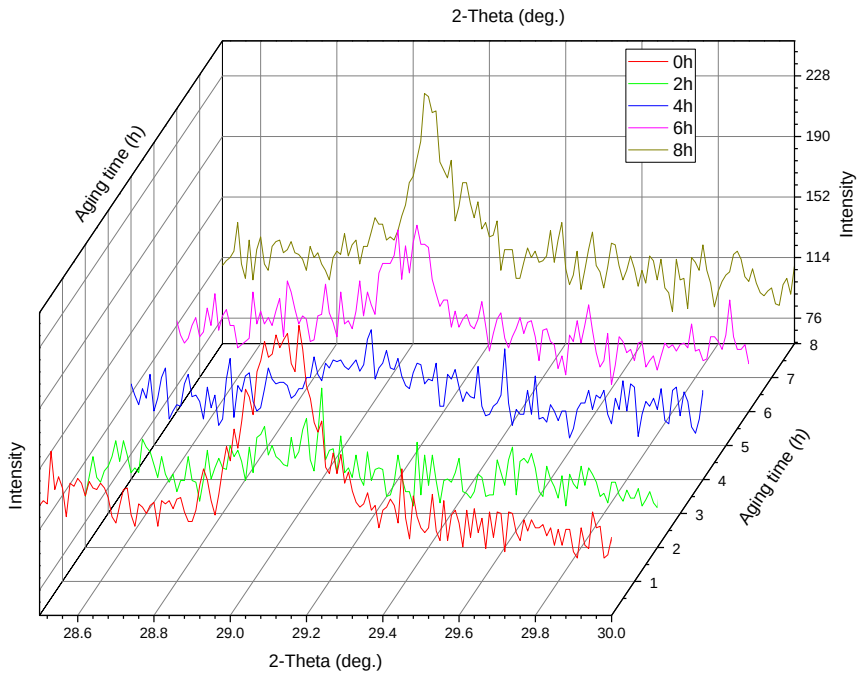

Figure 31 - X-ray diffraction (XRD) spectra collected from the vicinity of the low intensity peak at ~ 29.2° of the $Ag_{0.04}Pb_{0.46}Te_{0.5}$ system after aging at 380 °C for different times.

7.1.3 In-situ TE properties

A unique aspect of this study is the in-situ LFA and SBA measurements for Ag- supersaturated PbTe specimens that are heated at certain temperatures for different durations to track the onset of nucleation of Ag_2Te-precipitates and their influence on TE properties. We measured the TE transport properties at a constant temperature of 380 °C. Graphical representations of the aging time-dependent thermal diffusivities, electrical conductivities, and Seebeck coefficients are presented in this section for different silver concentrations.

7.1.3.1 In-situ LFA

In this section we will present the results of the in-situ LFA experiments described in chapter 6.4.2.1. In-situ samples prepared as described in chapter 6.1.2, and placed inside the LFA holder. Because the major changes took place during the first few hours of the in-situ experiment, which limited us to measuring only one

sample at a time, and based on our previous work in the group[18], we chose to ignore the heat capacity measurement using the LFA instrument. This enabled us reducing the measurement time, since no additional time is required to collect laser shots from reference samples; this is critical in such in-situ experiments. We measured the thermal diffusivity for all of the samples using LFA, for an aging temperature of 380 °C. It should be noted that the samples stayed inside the chamber during heating for about 40 min. until it reached 380 °C. Figure 32 shows the thermal diffusivity values that were probed for the AQ $Ag_xPb_{0.5-x}Te_{0.5}$ samples with the following compositions corresponding to x=0, 0.01, 0.02, 0.03, and 0.04 during aging at 380 °C.

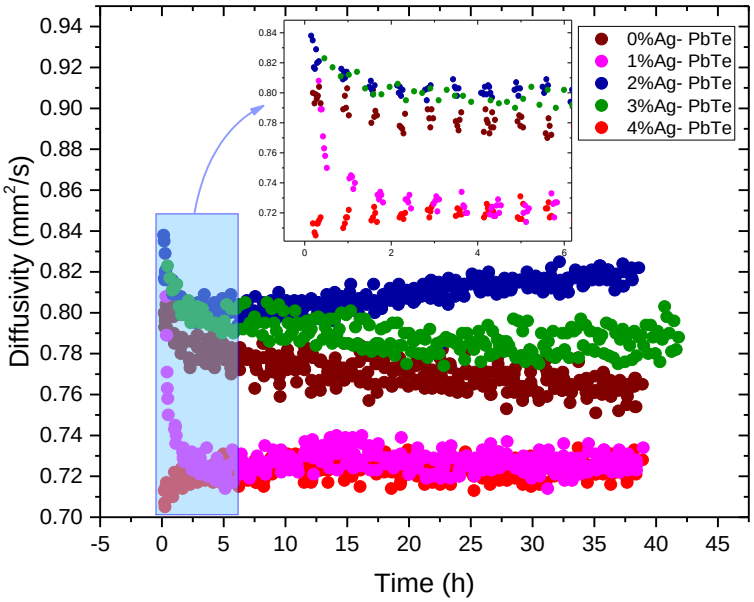

Figure 32 – In-situ measurements of the thermal diffusivity for the AQ $Ag_xPb_{0.5-x}Te_{0.5}$ samples with the following compositions corresponding to x=0, 0.01, 0.02, 0.03, and 0.04 during aging at 380 °C.

7.1.3.2 In-situ SBA

In this section we will present the results of the in-situ SBA experiments described in chapter 6.4.1.2. In-situ samples were prepared as described in chapter 6.1.2, and placed inside the SBA holder. Using the SBA we measured both the Seebeck coefficients and electrical conductivity for an aging temperature of 380 °C. Figure 33 and 34 display the Seebeck coefficients and electrical conductivity values vs. aging time at 380 °C for different Ag concentrations, respectively.

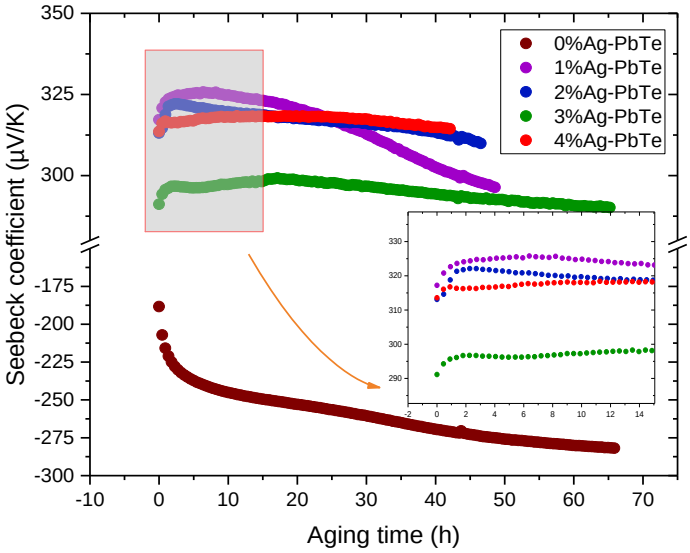

Figure 33 - In-situ measurements of the Seebeck coefficient for the AQ $Ag_xPb_{0.5-x}Te_{0.5}$ samples with the following compositions corresponding to x=0, 0.01, 0.02, 0.03, and 0.04 during aging at 380 °C.

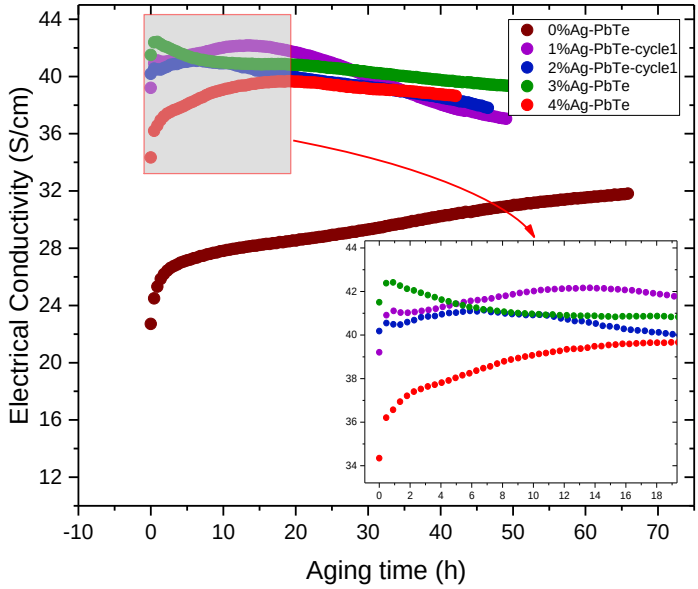

Figure 34 - In-situ measurements of the electrical conductivity for the AQ $Ag_xPb_{0.5-x}Te_{0.5}$ samples with the following compositions corresponding to x=0, 0.01, 0.02, 0.03, and 0.04 during aging at 380 °C.

In what follows, we calculated other TE coefficients that are derived from the above thermal and electrical conductivities and Seebeck coefficients; namely PF, lattice component of thermal conductivity, and the TE figure of merit.

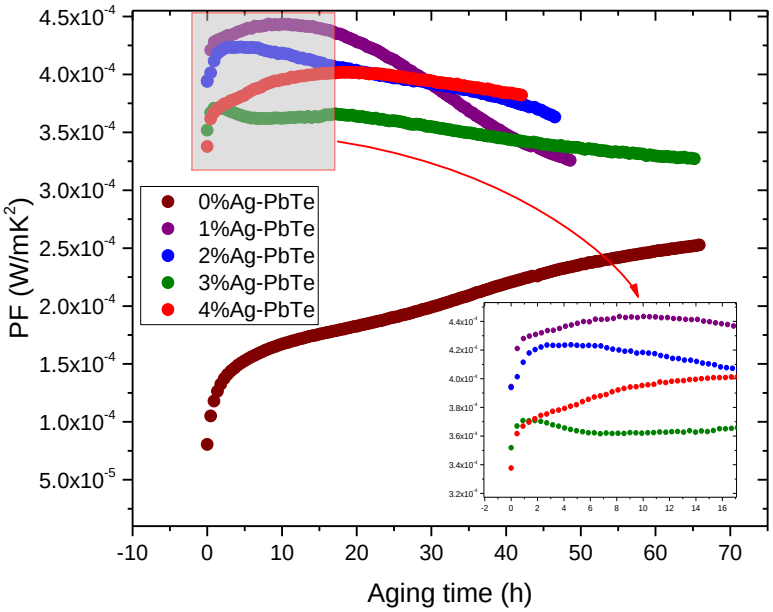

Figure 35 - In-situ measurements of the PF calculated for the AQ $Ag_xPb_{0.5-x}Te_{0.5}$ samples with the following compositions corresponding to x=0, 0.01, 0.02, 0.03, and 0.04 during aging at 380 °C.

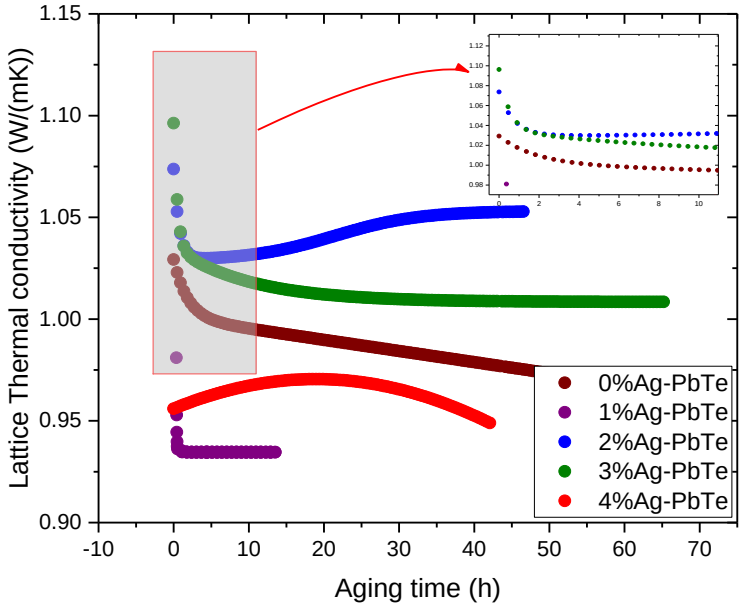

Figure 36 - In-situ measurements of the lattice thermal conductivity component calculated using Kim et al.[12] relation and Wiedemann-Franz[11] rule for the AQ $Ag_xPb_{0.5-x}Te_{0.5}$ samples with the following compositions corresponding to x=0, 0.01, 0.02, 0.03, and 0.04 during aging at 380 °C.

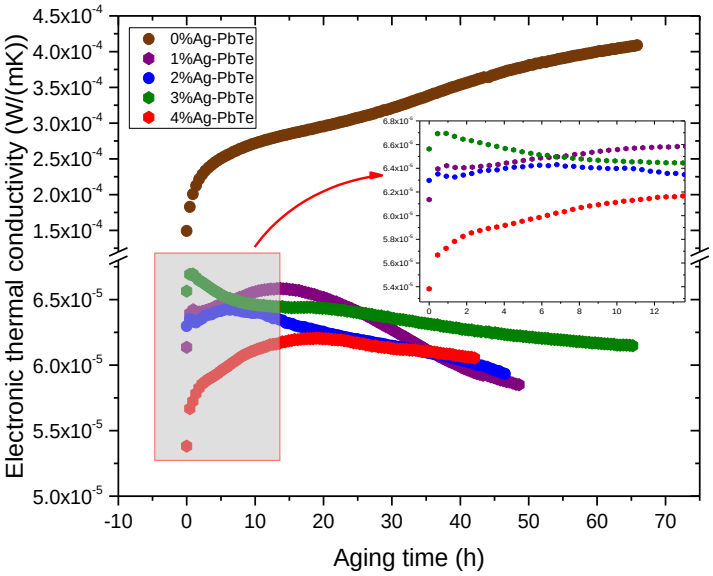

Figure 37 - In-situ measurements of the electronic thermal conductivity component calculated using Kim et al.[12] relation and Wiedemann-Franz rule[11] for the AQ $Ag_xPb_{0.5-x}Te_{0.5}$ samples with the following compositions corresponding to x=0, 0.01, 0.02, 0.03, and 0.04 during aging at 380 °C.

Calculation of zT was obtained by fitting an *ExpGro2* function to the diffusivity results ($\kappa = y_0 + A_1\exp(x/t_1) + A_2\exp(x/t_2)$) for the different Ag concentrations and the results are shown in Figure 38. These results were calculated using constant density and C_p values that were derived from a previous study made in our group. [18]

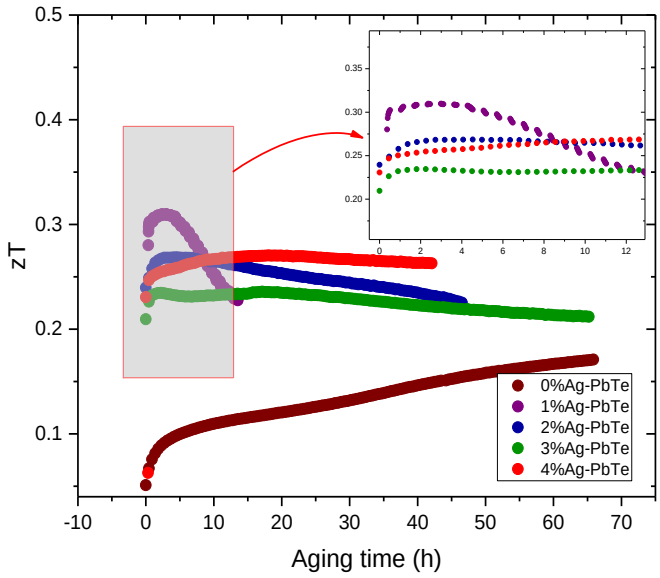

Figure 38 - In-situ measurements of the zT calculated for the AQ $Ag_xPb_{0.5-x}Te_{0.5}$ samples with the following compositions corresponding to x=0, 0.01, 0.02, 0.03, and 0.04 during aging at 380 °C.

7.2 Computational results

DFT is used to calculate point defect energies, tracer diffusion coefficients, electron bandgaps, bandstructures, and lattice parameters in the selected PbTe material. A "cif file" for the relaxed Empressite structure for DFT calculations using parameters discussed in chapter 6.5.1.2 can be found in Appendix II.

7.2.1 Electronic bandgap and bandstructure

Under the parameters and conditions described in chapter 6.5.1.2, we calculated the band structures, see Figure 39, from which we extracted the direct bandgap of PbTe obtained from the different functionals. They are listed in Table III.

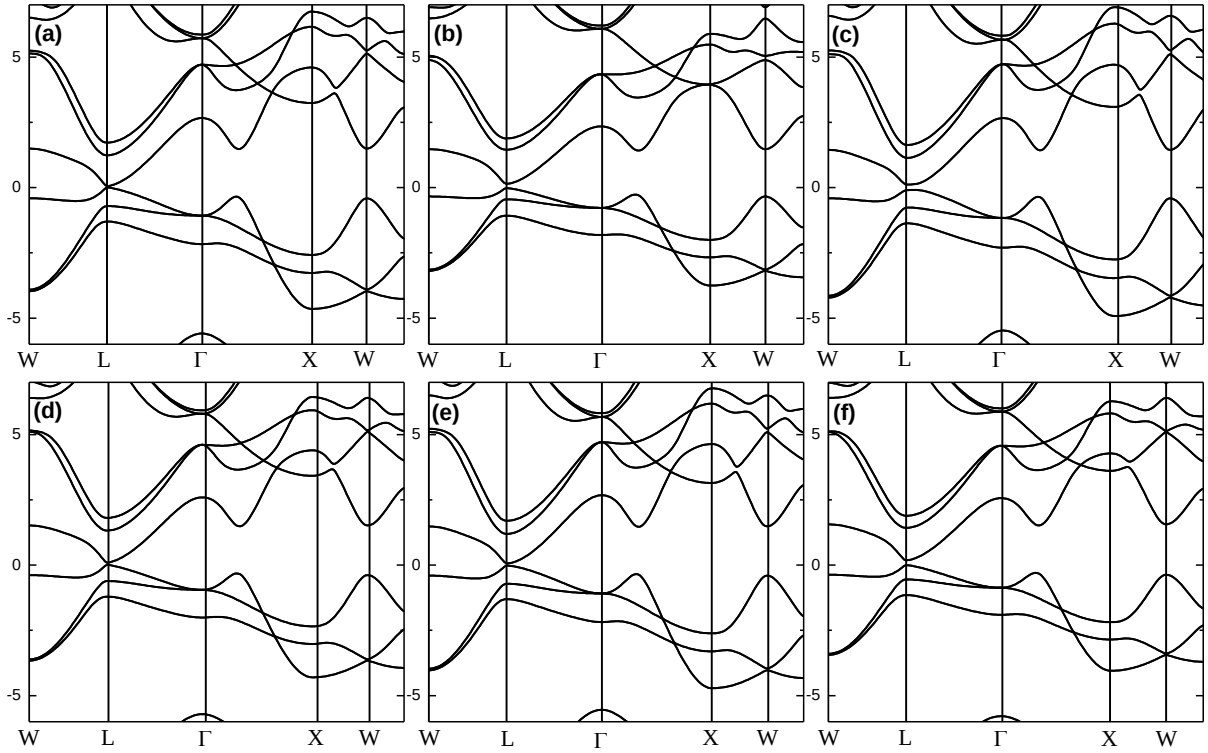

Figure 39 - Electronic band structures calculated for pure PbTe applying SOC for the following approximations of the exchange-correlation functional: (a) GGA-AM05, (b) GGA-BLYP, (c) LDA, (d) GGA-PBE, (e) GGA-PBEsol and (f) GGA-rPBE.

Table III - The values of bandgap and lattice parameter calculated using the LDA, BLYP, PBE, rPBE, AM05, and PBEsol functionals, with or without consideration of SOC, compared with experimental parameters from literature. [16,113,114]

Method		E_g [eV]	lattice parameter [Å]
Literature		0.19	6.462
LDA	w/o SOC	0.53986	6.366959
	with SOC	0.20533	6.361244
GGA-AM05	w/o SOC	0.70476	6.45
	with SOC	0.04348	6.441758
GGA-PBEsol	w/o SOC	0.6378	6.431125
	with SOC	0.08328	6.426815
GGA-PBE	w/o SOC	0.81616	6.549881

	with SOC	0.0797	6.549881
GGA-rPBE	w/o SOC	0.9543	6.634315
	with SOC	0.18956	6.625582
GGA-BLYP	w/o SOC	0.99177	6.728633
	with SOC	0.17036	6.719971

7.2.2 Gibbs formation energies

Using the parameters described in chapter 6.5.1, we calculate the point defect Gibbs formation energies for Ag atoms residing in interstitial sites in PbTe, and Pb- or Te-vacancy formation energies. This calculation takes into account only the vibrational components of entropy, which denote the uncertainty in molecular orientation.

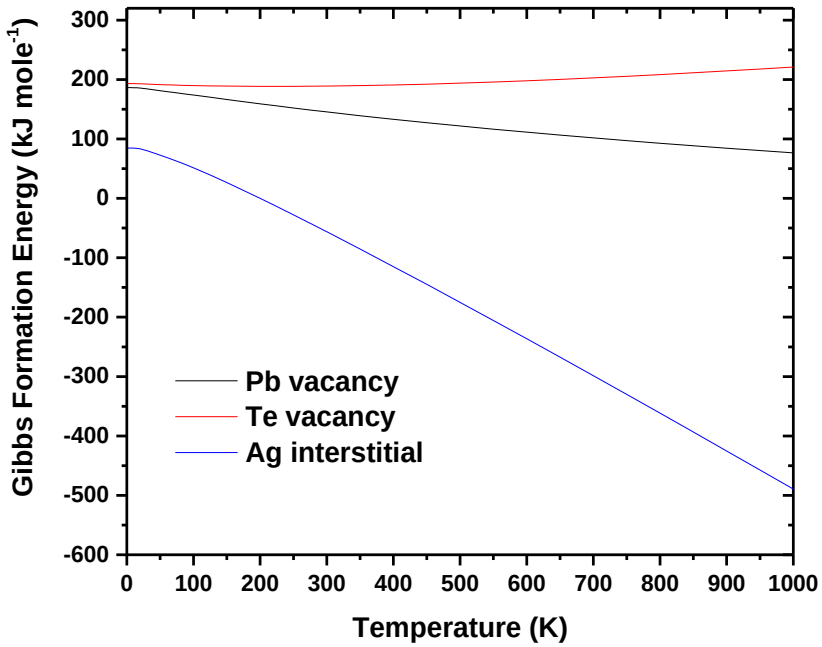

Figure 40 - The temperature-dependent Gibbs free energy change associated with formation of Te-vacancy in PbTe (red line), Pb-vacancy in PbTe (black line), and Ag-interstitial defect in PbTe (blue line) calculated from first-principles.

Our calculations indicate that minimum Gibbs free energy values are attained when Ag atoms occupy interstitial sites in the PbTe lattice. It is also indicated that the system favors Pb-vacancies more than Te-vacancies. The higher value obtained by us for Te- compared to Pb- vacancies at 0 K adheres to experimental entropy values,

which are reported to be 28.94 and 115.78 kJ·mole^{-1}, respectively.[16] These data may also explain the relatively high solubility of silver in the PbTe-matrix regardless of the temperature.[116]

7.2.3 Electronic partial density of states and electron localization function

We calculate the electronic partial density of states (p-DOS) of all atomic species to demonstrate the dominance of *p-d* hybridization in chemical bonds, and how it determines the site-substitution nature of Ag; particularly, whether it prefers substitution or interstitial sites. Incorporation of an individual Ag-atom into the PbTe lattice in either interstitial or substitutional sites is expected to affect the p-DOS diagrams differently, thereby providing deeper insight into the role of electronic structure on Ag site-substitution. The results are shown in Fig. 39.

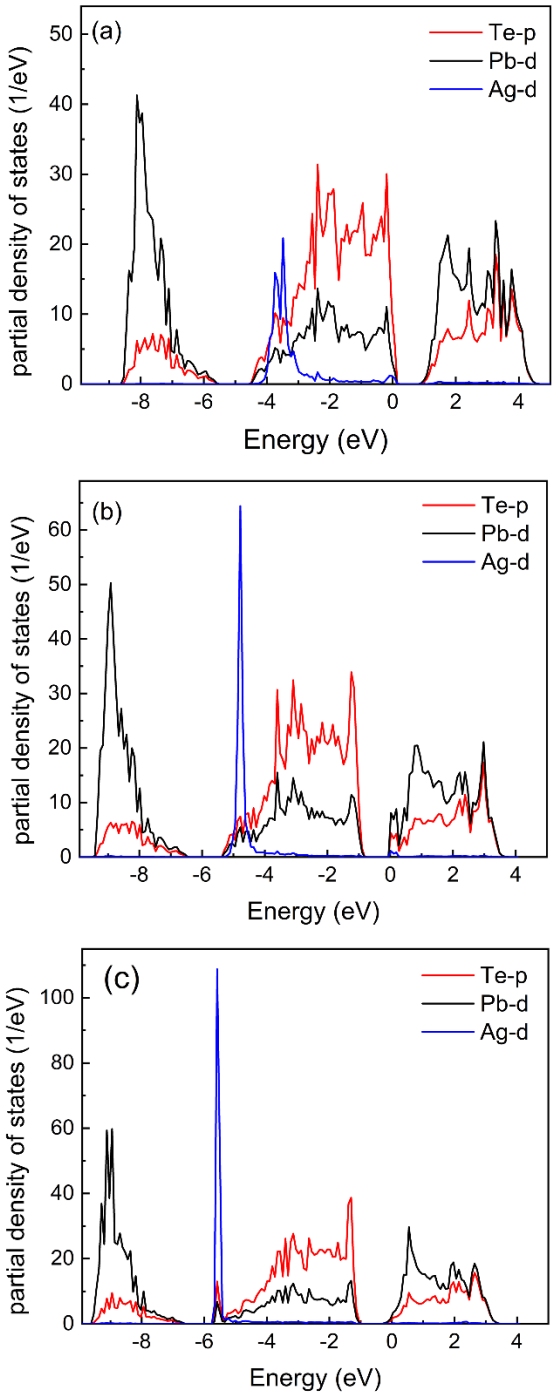

Figure 41 - The partial density of states (p-DOS) diagrams calculated for a PbTe lattice from first-principles, with an Ag-atom residing at (a) Pb- and (b) Te-substitution sites, respectively; and (c) interstitial site. Hybridization between the Pb-*d* (black line) and Te-*p* (red line) electronic bands is indicated. The presence of an Ag-atom in an interstitial site results in a sharp Ag-*d* (blue line) peak around -5.5 eV with pronounced overlap with the Te-*p* peak. In all three diagrams the Fermi level, E_F, is set to 0.

We also employ the electron localization function (ELF) algorithm to visualize the effect of Ag point defects on the local electronic distribution in the PbTe lattice. The ELF is derived from the conditional probability of finding a second electron at a position *B*, given that a first electron having the same spin is located with certainty at position *A*.[117] The ELF attains values ranging between 0 (no localization) and 1 (complete localization), and is very convenient for visualization, as opposed to the electron charge density, which reaches unbounded negative values.[118] A detailed description of the ELF algorithm and its application to identify site substitution preference can be found elsewhere.[119]

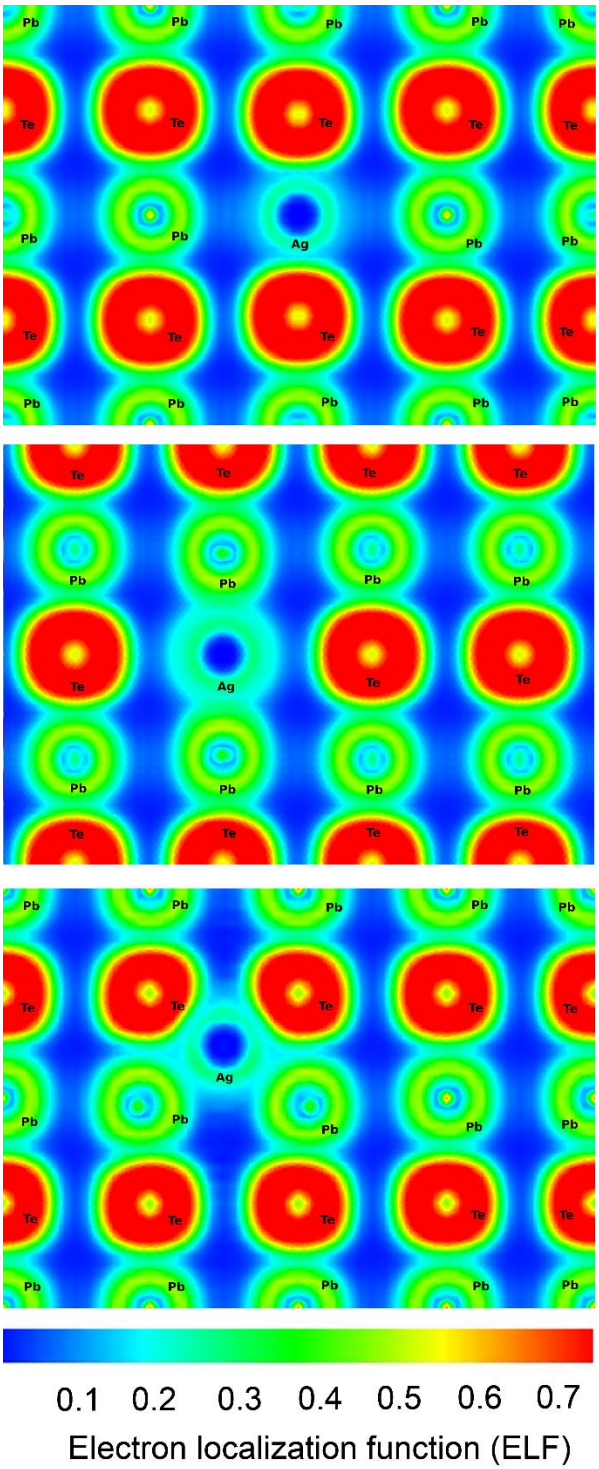

Figure 42 - Two-dimensional color-coded electron localization function (ELF) maps cross-sectioned along the (110) plans of Ag-doped PbTe lattices calculated from first-principles, for the cases where an individual Ag-atom resides at (a) Pb- or (b) Te-substitution site; and (c) interstitial site. Areas exhibiting high ELF-values in the inter-atomic regions indicate stronger tendency to interatomic bonding.

7.2.4 Calculated diffusion coefficients

We used the previous results presented in chapter 6.5.1 and determine the PBEsol functional as the most appropriate one for the present case, and set the following computational parameters: $E_{cut\text{-}off}$=270 eV, *k*-mesh density of 0.118 $Å^{-1}$, and a smearing width of 0.126563 eV to calculate the temperature dependent diffusion coefficients of Ag in PbTe. The calculated results for HTST and QQ-HTST with/without SOC, including comparison to Didik's [66] estimation, are presented in Figure 43.

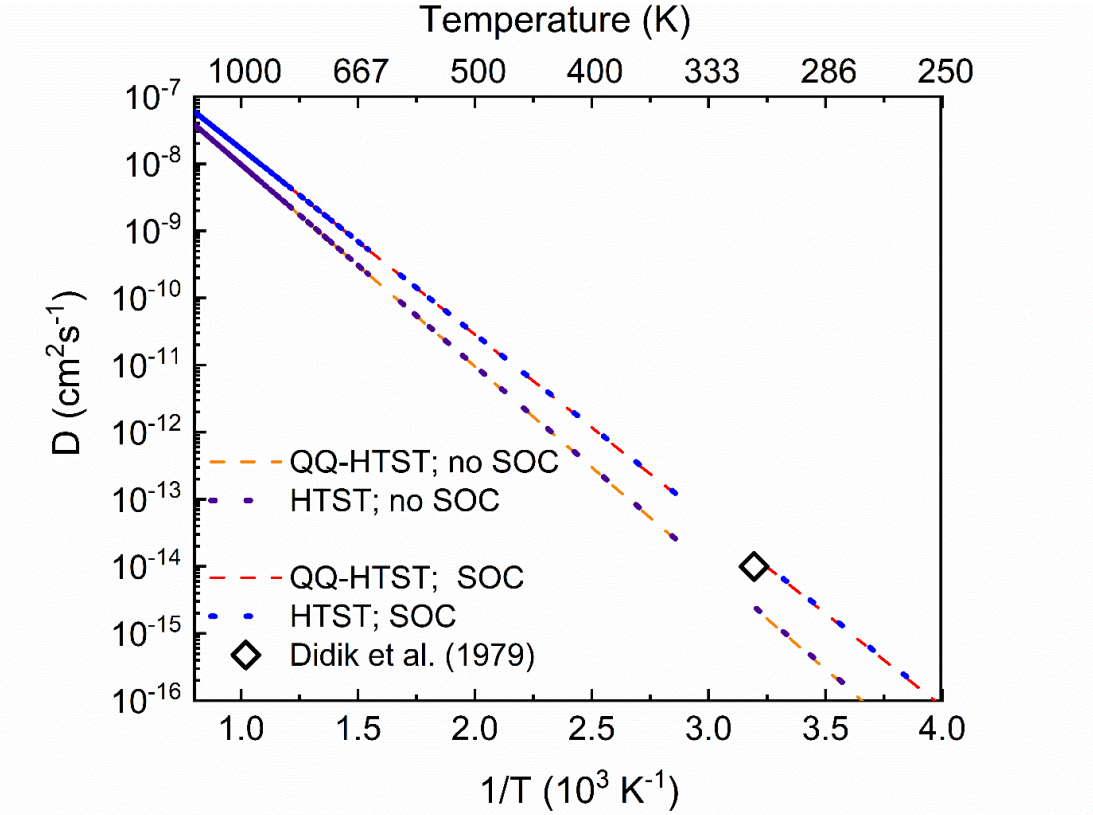

Figure 43 - The temperature dependent diffusion coefficients of Ag in PbTe, as calculated from first-principles applying the HTST approximation or the QQ-HTST either with consideration of SOC, denoted by the dotted blue or dashed red lines, respectively; or without SOC, denoted by the dotted violet or dashed orange lines, respectively. The black diamond symbol denotes an experimental measurement performed by Didik et al.[66]

8 Discussion

We will first discuss the experimental results and then the computational results; finally, we will draw the correlation between them.

8.1 Microstructure evolution

We will begin with analysis of the phases from XRD. The diffraction peaks can be attributed to the PbTe- and Ni- phases with an exception of a very low-intensity peak at $2\theta \approx 29.2°$ and very low intensity two peaks at $2\theta \approx 41.7°$ which may correspond to planes (021), (220), and (202), respectively, of the $AgTe_3$ rhombohedral phase having the space group R3m (160). It may indicate the existence of Te-excess, as expected from the $Ag_xPb_{0.5-x}Te$ stoichiometry.

Analysis of the XRD patterns collected for $Ag_xPb_{0.5-x}Te_{0.5}$ with x=0, 0.01, 0.02, 0.03, or 0.04, as well as for $Ag_{0.04}Pb_{0.46}Te_{0.5}$ aged for different times, reveals that these two low-intensity peaks emerge immediately after the quenching process or the homogenization treatment, as shown in Figure 31; then, disappear after 2 h heat treatment at 380 °C, and appear again with lower intensity after 4 h aging. Moreover, these peaks increase with increase of the Ag concentration, See Figure 28 and Figure 31. We conclude that Ag atoms are involved in formation of these peaks.

As shown in chapter 6.1, our powders underwent homogenization for 72 h in the single-phase region, see phase diagram in Figure 6. The stoichiometry of the $Ag_xPb_{0.5-x}Te_{0.5}$ indicated Te-excess. The preference of the silver atoms to reside in interstitial sites (over substitutional sites) will be discussed later in chapter 8.4. This results in excess of Te migrating outside the PbTe matrix.

As shown in chapter 6.1.1, all XRD powders underwent aging treatments at 380 and 300 °C, and were quenched. As realized in chapter 4.3.5.4, $AgTe_3$ phase usually appears after rapid cooling from an equilibrated melt above 365 °C, which explains the appearance of diffraction peaks for all powders that did not undergo aging after the first quenching from 700 °C, see Figure 29, Figure 30 and Figure 31. For our XRD powders undergoing aging treatments at 300 °C, the peak associated to $AgTe_3$ vanish after an hour of aging and does not appear anymore, as expected from the pressure and temperature-relations built by Range et al;[38] see Figure 8, and as expected for rapid

cooling from temperature lower than 365°C, see chapter 4.3.5.4. The high degree of fitting obtained in the Rietveld refinement that included the phases Ni, PbTe, and $AgTe_3$ confirms that these are peaks of $AgTe_3$. We, therefore, conclude that the peak located at $2\theta \approx 29.2°$ is associated to the $AgTe_3$ phase.

It will now be important to understand the appearance, disappearance, and re-appearance of the peak $AgTe_3$ under aging treatments at 380 °C for the $Ag_{0.02}Pb_{0.48}Te_{0.5}$ and $Ag_{0.04}Pb_{0.46}Te_{0.5}$ powders, and disappearance of the $AgTe_3$ peak in the $Ag_{0.02}Pb_{0.48}Te_{0.5}$ powders during aging treatments at 300 °C.

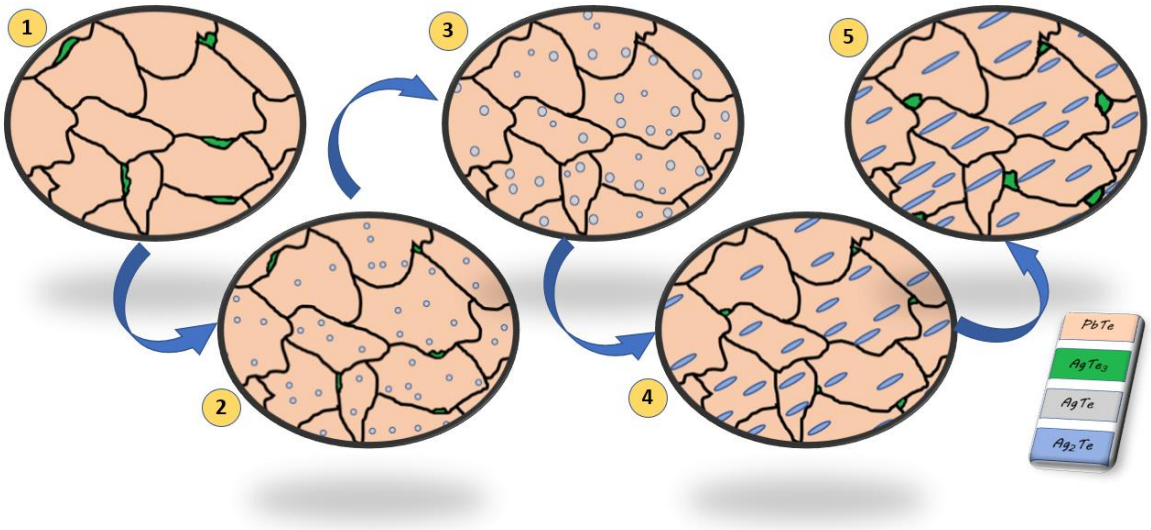

Figure 44 – An optional scenario of the microstructure evolution of Ag-alloyed PbTe under aging, based on the x-ray diffraction (XRD) analysis. (1) During the quenching process, low concentration Ag atoms are available for the excess of Te atoms that may migrate out of the PbTe matrix to form the $AgTe_3$ phase. (2) Seeds of AgTe may appear by consumption of Te from the $AgTe_3$ reservoirs. (3) This process continues until all excess Te atoms in the PbTe-matrix are consumed. (4) AgTe precipitates that reach a critical nucleus size begin transformation into the Ag_2Te-phase in the form of precipitates. Te atoms are released into the matrix, which leads to the re-appearance (5) of the $AgTe_3$ phase during aging treatment.

The reason for the absence of the peaks associated to the Ag_2Te and AgTe precipitates from the XRD patterns, though common for such concentrations of Ag, [18,27,120] is unclear to us yet. However, in the study of Sheskin et al. [28] on samples undergoing almost identical synthesis processes (48 h homogenization instead of 72 h), small precipitates of ~10 nm dia. having Ag:Te stoichiometry of 1:1 and large precipitates of ~100 nm dia. having 2:1 stoichiometry were observed immediately after quenching and prior to the aging treatment. Since the AgTe-phase is stable below 210 °C, see chapter 4.3.5.3, the growth of the AgTe phase during the homogenization treatment at 700 °C is not enabled, which led us to assume that precipitates of the AgTe-phase, which is metastable in our aging temperature (380 °C), serve as seeds for growth of Ag_2Te during the aging treatment. This scenario, illustrated in Figure 44, may explain the interesting phenomenon of appearance, disappearance, and re-appearance of the $AgTe_3$ peak during aging treatment at 380 °C in both $Ag_{0.02}Pb_{0.48}Te_{0.5}$ and $Ag_{0.04}Pb_{0.46}Te_{0.5}$ powders as follows.

During the homogenization treatment at 700 °C, Ag-atoms reside in substitution / interstitial sites in the PbTe matrix. Hence, during the quenching process, not many silver atoms are available to form a compound with Te, so that the $AgTe_3$ phase is formed with a 1:3 stoichiometry; it usually appears during rapid cooling, Figure 44.(1). At the aging temperature (380 °C), seeds AgTe appear by consumption of Ag and Te from both matrix and $AgTe_3$ precipitates, which dissolve, Figure 44.(2). This is the reason for the decrease of the $AgTe_3$ peak intensity observed during aging. This process continues until all excess Te atoms (beyond their solubility limit) in the matrix are consumed. AgTe nuclei reaching their critical size then begin to undergo phase transformation into the Ag_2Te-phase in the form of precipitates. Transition into this 2:1 stoichiometry released Te back into the matrix. These Te-atoms reform the $AgTe_3$ precipitates, which become stable at this temperature (380 °C). Alternatively, $AgTe_3$ precipitates "revive" during the rapid cooling (Figure 44.(4)-(5)). This explains the re-appearance of the peak associated to $AgTe_3$ during aging at 380 °C, as observed in the XRD patterns. It turns out that the variation of precipitates' chemistry during this process is reflected by transition between the following Ag:Te ratios: 1:3 → 1:1 → 2:1 → 1:3.

The disappearance of the $AgTe_3$ peak during the first 1 h of the aging treatment at 300 °C and the fact that it did not reappear as for the 380 °C treatment can also be explained by this assumption, since the rapid cooling for any aging process at the 300 °C experiment was from a temperature lower than 365 °C.

8.2 Thermoelectric measurements

In contrast to our expectation from the Ag-doped PbTe system based on our previous experience,[26,27] the changes that were observed in the thermal diffusivity, electrical conductivity, and Seebeck coefficient values, as well as the resulting PF and *z*T, are meager. Furthermore, the TE properties were also relatively poor in their absolute values, reaching a maximum value of $zT \approx 0.3$. Probably the main reason for these poor transport properties is the low density achieved in the HP process, see Figure 26. This is clearly evidenced from the SEM micrographs showing a fracture surface with poor connection between the particles ground in $Ag_{0.01}Pb_{0.49}Te_{0.5}$, see Figure 23. Another evidence was also observed for a polished surface of the $Ag_{0.01}Pb_{0.49}Te_{0.5}$ sample, see Figure 24 and Figure 25.

Prior to comparison between XRD and in-situ sets of experimental data, it is noteworthy that the results of the in-situ experiments are for the same synthesized materials, but with the addition of the HP process (about 15 min. at 650 °C under 47 MPa). The heating process up to 380 °C (the aging temperature) at the LFA/SBA furnace prolongs about 40 min., which should be taken into account, as well.

Evaporation of Te from the samples during the in-situ measurements should not be considered for two reasons. According to a previous report, the tellurium vapor pressure should range between 10^{-4} and 10^{-2} torr for the temperature range of 300 - 380 °C, [121] and the in-situ experiments are performed under Ar atmosphere at 1 atm. The above indicate that most of the change in the in-situ values is due to microstructure evolution.

8.2.1 In-situ LFA

The differences in heat capacity for different aging times were reported by Sheskin [18] to decrease by ~ 0.01 $Jg^{-1}K^{-1}$ after 6 h aging at 380 °C and to increase back to the starting heat capacity value after 48 h aging. We considered in this study a

constant value of 0.156 $Jg^{-1}K^{-1}$, based on Sheskin's work, provided that the samples were prepared using the same methodology and instruments. [18]

The results provided in Figure 32 show that all significant changes occur during the first 2 h, which is remarkable and shows that the microstructure evolution is fast. The main problem with in-situ experiments is the lack of a uniform reference state, i.e. t=0 is essentially not identical for all, since not all samples were in the same carousel, and measurements were not taken at the same time. We can conclude that any comparison between the behavior of the specimens containing different amounts of Ag should be done with extra care. The decrease in thermal diffusivity was much lower than expected, as shown in Figure 32. However, it is important to note that heating up to 380 °C (the aging temperature) at the LFA furnace prolongs about 40 min., which is in the same order of magnitude of the time required for significant changes in microstructure. The most significant decrease was obtained for sample $Ag_{0.01}Pb_{0.49}Te_{0.5}$, by ca. 0.1 mm^2/s. All of these results for 1-3 at. % Ag (diffusivity decreases) are due to precipitation that scatters phonons. The other samples showed decrease by about 0.01 mm^2/s. Also, the pure PbTe sample showed comparable reduction. The 4 at. % Ag sample shows an opposite trend: diffusivity increases. We can easily assume that the concentration of 4 at. % Ag is too high, and slightly surpasses the solubility limit. So, precipitation does not occur during the in-situ experiments (it has reached saturation in the former stages), and the matrix is cleaned from the supersaturated Ag-solute atoms; therefore, diffusivity increases.

8.2.2 In-situ SBA

As shown in chapter 4.3.5.5, when the silver atoms occupy interstitial sites they act as donors (n-type), and when they occupy Pb-substitution sites they act as acceptors (p-type). As discussed in chapter 4.1.1.1, positive Seebeck coefficient indicates a p-type semiconductor and negative Seebeck coefficient indicates n-type semiconductor. A common way to control the polarity of the PbTe semiconductor is to increase the concentration of one of the matrix elements: p-type conductivity under Te-rich conditions and n-type under Pb-rich conditions. As expected, [90] the Ag-doped samples (Te-rich) feature p-type polarity. Another confirmation for this behavior is the n-type polarity of the undoped PbTe, see Figure 33. What can be obtained from the in-situ

results are changes in polarity over time. For example, the sample becomes more or less p-type with the increase or decrease of the Seebeck coefficient, respectively. Figure 33 and Figure 34 show very similar trends of decrease, which can be easily related to the consumption of Ag from the matrix. Since Ag atoms are consumed by Ag-rich precipitates during their nucleation and growth, their average concentration in the PbTe matrix decreases with aging time; therefore, the polarity of the Seebeck coefficient as p-type and the electrical conductivity, decreases.

Most Ag-doped samples show increase in the first 7 h up to maximum values of electrical conductivity or Seebeck coefficient. The time to obtain maximum values of both for different Ag concentrations is given in Table IV. As discussed in chapter 8.2, heating up to 380 °C prolongs about 40 min., which is in the same order of magnitude as the time required for significant changes in microstructure. Thus, the results presented in Table IV must be considered very carefully.

Table IV – The time required to obtain maximum values of Seebeck coefficients and electrical conductivity for different Ag concentration.

	Time [h]	
Ag concentration [at. %]	**Seebeck coeff.**	**Electrical conductivity**
0	-	-
1	7	12
2	2.5	5.5
3	1.7	0.5
4	0.5	~ 0

It is indicated that increase of the Ag concentration reduces the time needed to reach the maximum value of the Seebeck coefficient and electrical conductivity. This may be related to precipitate nucleation rate, which grows with increasing Ag concentration.

For adequately longer aging times than the time presented in Table IV, the coarsening regime begins, in which N_v decreases along with the decrease of lattice strain. At that time, the average concentration of solute Ag atoms in the matrix

continues to decrease with aging time until it reaches an equilibrium value for longer aging times. We can observe these trends up to 65 h, and maybe more.

The PF, shown in Figure 35, is the product of Seebeck coeff. and electrical conductivity; hence the drastic changes observed for all the PF values.

To differentiate between the electronic and lattice components we evaluate the former applying the Wiedemann-Franz relationship,[11] equation 7, where L is evaluated for a general case of non-degenerate semiconducting behavior by applying the semiempirical expression reported by Kim et al.,[12] equation 8. Figure 36 and Figure 37 show that the electronic component is lower by approx. five orders of magnitude than the lattice component. Also, the changes in the electronic thermal conductivity component are of the order of magnitude of about $0.5 \cdot 10^{-5}$ $Wm^{-1}K^{-1}$; that is, no change with respect to the observed changes in the lattice thermal conductivity (which are also of the order of magnitude of 0.5 $Wm^{-1}K^{-1}$). This confirms our claim that all the changes in thermal conductivity are mainly due to the changes in the microstructure.

Figure 38 shows the effects of aging and microstructure evolution on the TE figure of merit, zT. Interestingly, it is indicated that zT is extremely sensitive to microstructure evolution, particularly for the undoped and 1 at. % Ag-doped PbTe samples. For higher Ag-concentrations, zT becomes less sensitive. Additionally, the undoped-PbTe material exhibits maximum zT-values that are lower than those of the doped ones. The major changes in TE transport coefficients occur for the electrical conductivity and Seebeck coefficient. The only reason for the changes in thermal diffusivity is due to development of scattering centers and, as expected, they are almost not observed for undoped PbTe. Our explanation for the changes in electrical behavior for undoped-PbTe is that these changes result mainly from evaporation of Te during the aging process. Conversely, the thermal conductivity, which appears in the zT denominator, exhibits very small changes with respect to doped samples (Figure 36 and Figure 37). For the doped-PbTe samples, significant changes in all the components of zT can be observed (i.e. electrical and thermal conductivities and the Seebeck coefficient), in contrast to the behavior of the undoped-PbTe (Figure 36, Figure 32, and Figure 37).

Since there is a lack of a uniform reference state, i.e. t = 0 is essentially not identical for all heat treatments, it is impossible to subtract the changes obtained for undoped-PbTe from the other samples and thus to isolate the behavior resulting from the different Ag components.

8.3 Electronic bandgaps and bandstructures

To determine the exchange-correlation functional that is most appropriate for the current calculation, we test the local-density approximation (LDA) as well as several GGA -based and hybrid functionals, either with or without SOC. Electronic band diagrams were calculated using the following functionals: LDA,[122] BLYP,[123] PBE,[124] rPBE,[125] AM05,[126] and PBEsol. [83] Figure 39 shows the band structures calculated for these functionals considering SOC.

It is shown that the general shape of all band structures is preserved for all different functionals. This trend applies either with or without considering SOC. Our calculated band structures correspond to those reported elsewhere. [16,114,127–130] We refer to the bandgap values of PbTe that were experimentally acquired for PbTe at different temperatures by Dalven,[16] e.g. E_g (4.2 K) = 0.19 eV, E_g (77 K) = 0.217 eV, E_g (300 K) = 0.31 eV, and E_g (373 K) = 0.34 eV as reference values, although DFT generally underestimates the bandgaps. [130,131] Extrapolation of these values to 0 K yields E_g = 0.187 eV. The electronic bandgap solely is, however, not the only magnitude to be optimized; weighting between both electronic band gaps and lattice parameters is required. In this sense, the following three GGA-based functionals: PBE, PBEsol, and AM05 well- address this combination. We, eventually, decide to apply PBEsol with SOC for our calculations, since it yields better agreement with experimental values and, most importantly, since it has been widely utilized in the past to calculate TE properties of PbTe.[17,74,75,114,132] The better accuracy achieved for all the calculations considering SOC corroborates the statement that SOC is dominant in these systems.[74,107,128,133]

8.4 Gibbs formation energies

So far, no unambiguous evidence stating that the dominant mechanism of Ag diffusion in the rocksalt PbTe system is interstitial has been reported. However, there is some evidence that this mechanism is common in comparable systems. Silver is one of the noble metals, exhibiting completely-filled *d*-orbitals, such as Cu and Au. These metals are found to diffuse dominantly via the interstitial mechanism in PbSe.[16,63] The great similarity between the binary systems Pb-Te and Pb-Se considering the pertinent sections of their phase diagrams,[116,134] their band structures,[114,128] their chemical identity, crystallographic structures, and the different phases obtained after doping with silver, is indicative that the predominating diffusion mechanism of silver in PbTe should be interstitial by nature. To corroborate this choice, we compare both substitutional and interstitial states computationally.

Figure 40 shows that minimum Gibbs free energy values are attained when Ag atoms occupy interstitial sites in the PbTe lattice, and that the system favors Pb vacancies more than Te vacancies. These data justify our choice to calculate the diffusion coefficients of Ag in PbTe in the interstitial mechanism.

8.5 Electronic partial density of states and electron localization function

Figure 41 displays the p-DOS diagrams calculated for an Ag-atom residing at (a) Pb- and (b) Te-substitution sites, respectively; and (c) interstitial site. The p-DOS diagram indicates hybridization between the Pb-*d* and Te-*p* electronic bands, forming directional bonding between the Pb- and Te- nearest neighbors along the <100>-directions. This is manifested by shifts in the Pb-*d* and Te-*p* peaks in the p-DOS diagrams towards increased level of overlap, as appear in Figure 41 (a) and (b).

The presence of Ag atoms in either Pb- or Te-substitutional sites is manifested by sharp peaks at around -3.5 and -4.5 eV, respectively, where the Fermi energy, E_F, is zero. Slight overlaps between the Ag-*d* and Te-*p* peaks are observed in Figure 41 (a) and (b). Interestingly, introduction of an Ag-atom in an interstitial site results in a sharp Ag-*d* peak around -5.5 eV with pronounced overlap with the Te-*p* peak. Furthermore,

this yields stronger overlap between the local Pb-*d* and Te-*p* peaks. This behavior clearly signifies the preference of Ag- atoms for interstitial sites in the PbTe lattice.

Moreover, Figure 42 shows two-dimensional ELF mapping of the (110) planes comprising all three elements: Pb, Te, and Ag for the cases where an individual Ag-atom resides at (a) Pb- or (b) Te-substitution site; and (c) interstitial site.

Comparison between Figure 42 (a) and (b) indicates that Ag-Pb bonding is preferred more than Ag-Te bonding. This can be elucidated by the *p-d* hybridization shown above, which is enabled when both types of Pb-Te and Ag-Te bonding are formed. For the case where an Ag atom resides at an interstitial site, Figure 42 (c), bonding between Ag and both Pb- and Te-nearest neighbors is enabled, rendering it as the preferred state. This corroborates the conclusions drawn from the p-DOS diagrams.

8.6 Diffusion coefficient calculations

To corroborate our approach stating that interstitial Ag diffusion in Pb-chalcogenide systems is probable, we select the PbSe system as a case study, and calculate the activation energy for Ag diffusion in PbSe. Then, we compare our results to experimental data, which were provided by Fedorovich, [63] who reported on diffusion of ^{110}Ag radioactive isotope in a PbSe single crystal. This technique is considered to be the most accurate one for measuring tracer diffusion coefficients due to its high sensitivity to low concentrations spanning over a range of about five orders of magnitude in radioactive intensity. The activation energy for diffusion reported by Fedorovich, 33.76 kJ·mole^{-1}, is lower than the values calculated by us for PbSe, that is, 45.7 and 48.8 kJ·mole^{-1} with or without SOC, respectively. This is reasonable considering the lattice vibrations taking place at finite temperatures in practice, which facilitate the transport of the diffusing atom. For Ag diffusion in PbSe, consideration of SOC provided values that are closer to those reported by Fedorovich, highlighting the essence of the SOC effect in such calculations. We note that Fedorovich performed the diffusion measurements for single-crystalline samples, so that no other rapid ('short-circuit') diffusion mechanisms are expected, what makes these data comparable to those calculated in this study.

We determine the pre-exponential diffusion coefficient for an interstitial mechanism using either the HTST and QQ-HTST approximations, and obtain practically the same results, namely $9.69 \cdot 10^{-6}$ and $1.08 \cdot 10^{-5}$ $cm^2 \cdot s^{-1}$ with or without SOC, respectively. Similarly, both values of the activation energy for diffusion, with and without SOC, are determined to be 52.9 and 57.4 $kJ \cdot mole^{-1}$, respectively. Based on these data, the diffusion coefficients of Ag in PbTe are plotted for the entire temperature range where the rock-salt PbTe phase is stable (250 - 1190 K),[116,134–136] Figure 43. The difference between the calculated activation energies where SOC is considered or not is estimated to be ~ 4.5 $kJ \cdot mole^{-1}$.

The differences between the void radii corresponding to the interstitial sites of both rocksalt systems should also be considered. In the rocksalt system, all interstitial sites are symmetrically-equivalent, having the same radius. The interstitial site radii are 1.327 and 1.181 Å for PbTe and PbSe, respectively; that is, the interstitial site radius of PbTe is ca. 1.4 times larger than that of PbSe. Since the ionic radius of Ag is 1.26 Å,[137] it is reasonable that Ag atoms should occupy interstitial sites in PbTe more easily than in PbSe, which may account for the lower activation energy in PbSe with respect to that in PbTe.

Estimation of Ag bulk diffusion in PbTe was performed by Didik et al.[66] They reported on a value of $\sim 10^{-14}$ $cm^2 \cdot s^{-1}$ at 313 K. For comparison, the diffusion coefficients calculated by us applying SOC are $1.44 \cdot 10^{-14}$ and $1.39 \cdot 10^{-14}$ $cm^2 \cdot s^{-1}$ at 313 K for the HTST and QQ-HTST methods, respectively.

As a final remark, we compare our predicted diffusion data with other experimental results. The diffusion coefficient of Ag in PbTe can be extracted from the thorough study of Bergum et al., [32] who measured the concentration of Ag atoms across the interface between PbTe–Ag_2Te diffusion couples applying EPMA to determine the solvus lines of the PbTe and Ag_2Te phases in the pseudo-binary PbTe-Ag_2Te system. It is noteworthy that the goal of Bergum's study was not to determine diffusion coefficients; however, they can be indirectly extracted from the concentration profiles reported therein. The diffusion coefficients of Ag in PbTe at 375, 450, 550, and 650 °C were extracted by us to be $D_0^{Bergum} = 3.58 \times 10^{-5}$ $cm^2 \cdot s^{-1}$ and Q=87.05 $kJ \cdot mole^{-1}$ by fitting the Ag-concentration profiles to the error function,

describing diffusion of solute atoms from a semi-infinite source. Interestingly, this pre-exponential factor derived from Bergum et al. is close to that calculated by us; however, the activation energy is significantly larger than ours. These values correspond to $D^{Bergum}(313K)=1\cdot10^{-19}$ $cm^2\cdot s^{-1}$, which is a much lower value compared to the estimation given by both Didik et al. [66] and our calculation. Such deviations can be associated to the extremely high sensitivity of diffusion coefficients to the material's composition and impurity level, as well as to defects, degree of crystallinity, grain size, etc.,[138,139] which are difficult to consider in DFT calculations.

9 Summary and conclusions

This study introduces a combination between experimental and computational procedures. We evaluate the temperature-dependent diffusion coefficients of Ag in the TE compound PbTe applying DFT calculations and implementing the TST, considering both SOC and ZPE corrections. Our computational findings can be summarized as follows:

1. The dominant diffusion mechanism of Ag in PbTe is interstitial. This is supported by calculations of point defect formation energies.
2. It is found that consideration of SOC is essential for appropriate evaluation of the activation energy for diffusion mostly.
3. Conversely, both HTST and QQ-HTST approximations yield practically the same values of pre-exponential factors.
4. The pre-exponential diffusion coefficient for the interstitial mechanism is evaluated to be $9.69\cdot10^{-6}$ or $1.08\cdot10^{-5}$ $cm^2\cdot s^{-1}$ applying either the HTST or QQ-HTST approximations, respectively. The activation energy for diffusion is evaluated to be 52.9 and 57.4 $kJ\cdot mole^{-1}$, with or without SOC, respectively. These values seem to well-agree with the data measured by Didik et al.[66] at 313 K. Interestingly, the trend where the calculated activation energy considering SOC is greater than that calculated disregarding SOC is preserved for Ag diffusion in PbSe, as well, that is, 45.7 and 48.8 $kJ\cdot mole^{-1}$, respectively. For both PbTe and PbSe systems, which are chemically and crystallographically similar, the difference is ca. 3-4 $kJ\cdot mole^{-1}$.

In conclusion, our study provides useful information that enables us evaluate the kinetics of phase transformations in Ag-alloyed PbTe compounds applied for TE applications. Such information is very instructive in the broader view, by providing practical tools to assess thermal stability of TE compounds and conditions of service durations or temperatures in which TE devices are prone to degrade.

The experimental procedures allowed us to reveal the metastable $AgTe_3$ phase that is possibly involved in evolution of the Ag_2Te phase. The typical time for the disappearance/formation of the Ag-rich phase obtained in the XRD measurements is between 1-2 h. In-situ measurements also show changes that are probably due to microstructure evolution on the order of several hours. Our DFT calculations, on the other hand, yield $D_0 = 1.08 \cdot 10^{-5}$ $cm^2 \cdot s^{-1}$. Both experimental and computational magnitudes can be correlated to each other. For example, we consider the free energy of the $[01\bar{1}](100)PbTe \| [010](100)$ Ag_2Te interface (calculated in our group) to be $\gamma = 0.2$ $J \cdot m^{-2}$, the concentration of Ag inside Ag_2Te precipitates to be $C_\beta = 0.6$ and at the PbTe matrix $C_\alpha = 0.03$, and precipitate size of 100 nm, as measured by Sheskin et al. [28] Combining these magnitudes in the expression describing the average precipitate growth rate, as follows: [140,141]

$$R(t)^3 = R_0^3 + \left(\frac{8}{9}\right) \cdot \frac{C_\alpha \Omega \gamma D}{C_\beta RT} t \qquad (66)$$

enables us to estimate the characteristic time for microstructure evolution at 380 °C to be 15 min. This has strong implications for thermal stability and performance degradation of TE devices, based on nanostructured compounds.

We consider the above-described research to be challenging and original. To the best of our knowledge, it combines methods that are new to the field of TE materials. We believe that the results of this research will introduce a significant contribution to understanding the effects of microstructure evolution on TE performance.

10 References

1. Biswas, K. *et al.* High-performance bulk thermoelectrics with all-scale hierarchical architectures. *Nature* **489**, 414–418 (2012).

2. Seebeck, T. J. Ueber die magnetische Polarisation der Metalle und Erze durch Temperatur-Differenz. *Ann. Phys.* **82**, 133–160 (1826).
3. Thomson, W. On the Dynamical Theory of Heat. *Trans. R. Soc. Edinburgh* **20**, 261–288 (1853).
4. Thomson, W. IX.— On the Dynamical Theory of Heat . Part V. Thermo-electric Currents . *Trans. R. Soc. Edinburgh* **21**, 123–171 (1857).
5. Altenkirch, V. E. Über den Nutzeffekt der Thermosäule. *Phys. Zeitschrift* **16**, 560–568 (1909).
6. Altenkirch, E. Elektrochemische Kälteerzeugung und reversible elektrische Heizung. *Phys. Zeitschrift* **12**, 920–924 (1911).
7. Vedernikov, M. V. & Iordanishvili, E. K. A.F. Ioffe and origin of modern semiconductor thermoelectric energy conversion. 37–42 (2002) doi:10.1109/ict.1998.740313.
8. Bennett, G. & Skrabek, E. Power performance of US space radioisotope thermoelectric generators. *Int. Conf. Thermoelectr.* 357–372 (1996).
9. Yang, J. & Caillat, T. Thermoelectric Materials for Space and Automotive Power Generation. **31**, 224–229 (2006).
10. Heremans, J. P. Low-Dimensional Thermoelectricity. **108**, 609–634 (2005).
11. Franz, R. & Wiedemann, G. Ueber die Wärme-Leitungsfähigkeit der Metalle. *Ann. Phys.* **165**, 497–531 (1853).
12. Kim, H. *et al.* Characterization of Lorenz number with Seebeck coefficient measurement Characterization of Lorenz number with Seebeck coefficient measurement. **041506**, 1–6 (2015).
13. Tom Grossfeld. Microstructure Evolution Applications, Enhancement of the Thermoelectric Conversion Efficiency of PbTe-based Compounds for Renewable Energy. (2015).
14. Lin, J. C., Hsleh, K. C., Sharma, R. C. & Chang, Y. A. The Pb-Te (lead-tellurium) system. *Bull. Alloy Phase Diagrams* **10**, 340–347 (1989).
15. Dughaish, Z. Lead telluride as a thermoelectric material for thermoelectric power generation. *Phys. B Condens. Matter* **322**, 205–223 (2002).
16. Dalven, R. A Review of the Semiconductor Properties of PbTe , PbSe , PbS and PbO. *Infrared Phys.* **9**, 141–184 (1969).

17. Zhang, Y., Ke, X., Chen, C., Yang, J. & Kent, P. R. C. Thermodynamic properties of PbTe, PbSe, and PbS: First-principles study. *Phys. Rev. B - Condens. Matter Mater. Phys.* **80**, 1–12 (2009).
18. Sheskin, A. Defects and interfaces in Ag- alloyed PbTe compounds for thermoelectric applications. (Technion, 2018).
19. Gayner, C. & Kar, K. K. Recent advances in thermoelectric materials. *Prog. Mater. Sci.* **83**, 330–382 (2016).
20. Fiss, A. L. Thermoelectric bonding study. *Nasa* 66 (1966).
21. Xie, G. Powder Metallurgy & Mining Spark Plasma Sintering : A Useful Technique to Develop Large-Sized Bulk Metallic Glasses. **2**, 2–4 (2013).
22. Li, G. & Nogami, M. Formation of Quantum-Size PbTe Microcrystals in Sol-Gel Derived Silica and Borosilicate Glasses. **83**, 79–83 (1993).
23. Ganguly, S. & Brock, S. L. Toward nanostructured thermoelectrics: Synthesis and characterization of lead telluride gels and aerogels. *J. Mater. Chem.* **21**, 8800–8806 (2011).
24. Hmood, A., Kadhim, A. & Hassan, H. A. Composition-dependent structural and electrical properties of PbSe1-xTex thin film. *Superlattices Microstruct.* 9 (2012).
25. Amouyal, Y. Reducing Lattice Thermal Conductivity of the Thermoelectric Compound AgSbTe2 (P4/mmm) by Lanthanum Substitution: Computational and Experimental Approaches. *J. Electron. Mater.* **43**, 3772–3779 (2014).
26. Sheskin, A. *et al.* Tailoring Thermoelectric Transport Properties of Ag-Alloyed PbTe: Effects of Microstructure Evolution. *ACS Appl. Mater. Interfaces* **10**, 38994–39001 (2018).
27. Grossfeld, T., Sheskin, A., Gelbstein, Y. & Amouyal, Y. Microstructure Evolution of Ag-Alloyed PbTe-Based Compounds and Implications for Thermoelectric Performance. *Crystals* **7**, 281 (2017).
28. Sheskin, A. *et al.* Tailoring Thermoelectric Transport Properties of Ag-Alloyed PbTe: Effects of Microstructure Evolution. *ACS Appl. Mater. Interfaces* **10**, 38994–39001 (2018).
29. Lensch-Falk, J. L., Sugar, J. D., Hekmaty, M. A. & Medlin, D. L. Morphological evolution of Ag2Te precipitates in thermoelectric PbTe. *J.*

Alloys Compd. **504**, 37–44 (2010).

30. Uher, C. *Materials Aspect of Thermoelectricity*. *Materials Aspect of Thermoelectricity* (2016). doi:10.1201/9781315197029.
31. Pei, Y., Lensch-Falk, J., Toberer, E. S., Medlin, D. L. & Snyder, G. J. High thermoelectric performance in PbTe due to large nanoscale Ag 2Te precipitates and la doping. *Adv. Funct. Mater.* **21**, 241–249 (2011).
32. Bergum, K., Ikeda, T. & Jeffrey Snyder, G. Solubility and microstructure in the pseudo-binary PbTeAg2Te system. *J. Solid State Chem.* **184**, 2543–2552 (2011).
33. Voronin, M. V., Osadchii, E. G. & Brichkina, E. A. Thermochemical properties of silver tellurides including empressite (AgTe) and phase diagrams for Ag–Te and Ag–Te–O. *Phys. Chem. Miner.* **44**, 639–653 (2017).
34. Karakaya, I. & Thompson, W. . T. The Ag-Te (Silver-Tellurium) System. *J. Phase Equilibria* **12**, 56–63 (1991).
35. Bradley, W. M. Empressite, a new silver-tellurium mineral from Colorado. *American Journal of Science* vols s4-38 163–165 (1914).
36. Bindi, L. Thermal expansion behavior of empressite, AgTe: A structural study by means of in situ high-temperature single-crystal X-ray diffraction. *J. Alloys Compd.* **473**, 262–264 (2009).
37. Luo, H. & Klement, W. *Metastable Simple Cubic Structures in Gold-Tellurium and Silver-Tellurium Alloys*. *The Journal of Chemical Physics* vol. 36 1870–1874 (1962).
38. Range, K. J. & Thomas, M. Pressure - temperature relations in the silver - tellurium system at 75 at-% tellurium. *Mater. Res. Bull.* **18**, 1195–1202 (1983).
39. Luo, H. L., Merriam, M. F. & Hamilton, D. C. Superconducting Metastable Compounds. *Science (80-.).* **145**, 581–583 (1964).
40. Range, K.-J. *et al.* A Novel Three-Dimensional Tellurium Array: High-Pressure Synthesis and Crystal Structure of AgTe3. *Angew. Chemie Int. Ed. English* **21**, 706–707 (1982).
41. Yu, Y. *et al.* Ag-Segregation to Dislocations in PbTe-Based Thermoelectric Materials. *ACS Appl. Mater. Interfaces* **10**, 3609–3615 (2018).
42. You, L. *et al.* Boosting the thermoelectric performance of PbSe through

dynamic doping and hierarchical phonon scattering. *Energy Environ. Sci.* **11**, 1848–1858 (2018).

43. Porter, D. A. & Easterling, K. E. *Phase Transformations in Metals and Alloys*. *Annual Review of Materials Science* (1992). doi:10.1146/annurev.ms.03.080173.001551.
44. Hale, B. N. Temperature dependence of homogeneous nucleation rates for water: Near equivalence of the empirical fit of Wölk and Strey, and the scaled nucleation model. *J. Chem. Phys.* **122**, (2005).
45. Markku Kulmala & Wagner, P. E. Nucleation and Atmospheric Aerosols 1996. *Nucleation Atmos. Aerosols 1996* (1996) doi:10.1016/b978-0-08-042030-1.x5000-8.
46. Peterson, N. L. Self-diffusion in pure metals. *J. Nucl. Mater.* **69**–**70**, 3–37 (1978).
47. Chakraborty, S. Diffusion in Solid Silicates: A Tool to Track Timescales of Processes Comes of Age. *Annu. Rev. Earth Planet. Sci.* **36**, 153–190 (2008).
48. Li, G. *et al.* Investigation of oxygen diffusion behavior in terbium using 18O<inf>2</inf> isotopic tracking by high resolution SIMS. *Mater. Lett.* **176**, 253–256 (2016).
49. Mantina, M. A first-principles methodology for diffusion coefficients in metals and dilute alloys. *Mater. Sci. Eng.* **PhD**, 252 (2008).
50. Shewmon, P. DIFFUSION IN SOLIDS. 252 (1989).
51. Hofmann, A. W., Giletti, B. J., Yoder, H. S. J. & Yund, R. A. Geochemical transport and kinetics. 362 pp. (1974).
52. Pearson, K. The problem of the random walk. *Nature* **72**, 342 (1905).
53. Blomqvist, A. Insights into Materials Properties from Ab Initio Theory: Diffusion, Adsorption, Catalysis & Structure. (2010).
54. Wimmer, E. *et al.* Temperature-dependent diffusion coefficients from ab initio computations: Hydrogen, deuterium, and tritium in nickel. *Phys. Rev. B - Condens. Matter Mater. Phys.* **77**, 1–12 (2008).
55. Eyring, H. The Activated Complex in Chemical Reactions. *J. Chem. Phys.* **3**, 107–115 (1935).
56. Wert, C. & Zener, C. Interstitial atomic diffusion coefficients. *Phys. Rev.* **76**,

1169–1175 (1949).

57. Mehrer, H. Diffusion in solids: fundamentals, methods, materials, diffusion-controlled processes. *Springer Ser. solid-state Sci.* (2007) doi:10.1007/978-3-540-71488-0.

58. Vineyard, G. H. Frequency factors and isotope effects in solid state rate processes. *J. Phys. Chem. Solids* **3**, 121–127 (1957).

59. Mantina, M., Wang, Y., Chen, L. Q., Liu, Z. K. & Wolverton, C. First principles impurity diffusion coefficients. *Acta Mater.* **57**, 4102–4108 (2009).

60. Lu, Y., Zheng, F. & Zhang, P. First-principles study of temperature-dependent diffusion coefficients for helium in α-Ti. *J. Appl. Phys.* **114**, (2013).

61. Einarsdóttir, D. Implementation of harmonic quantum transition state theory for multidimensional systems. *Reykjavík* (University of Iceland, 2010).

62. Dyson, B. F. F., Anthony, T. R. R. & Turnbull, D. Interstitial Diffusion of Copper and Silver in Lead. *J. Appl. Phys.* **38**, 3408–3408 (1967).

63. Fedorovich, N. A. Diffusion of silver and sodium in lead selenide. 1593–1594 (1965).

64. Ravich, Y. I., Efimova, B. A. & Smirnov, I. A. *Semiconducting Lead Chalcogenides*. *Monographs In Semiconductor Physics* vol. 5 (Institute of Semiconductors Academy of Sciences of the USSR, Leningrad, 1970).

65. Seltzer, M. S. & Wagner, B. J. Self-Diffusion of Lead-210 in Single Crystals of Lead Selenide. *J. Chem. Phys.* **36**, 130–134 (1962).

66. Didik, V. A., Malkovich, R. S. & Savin, E. P. Diffusion of Ag in PbTe and precipitation of solid solution of Au in Si under gamma irradiation conditions. 1427–1428 (1979).

67. Martin, R. M., Reining, L. & Ceperley, D. M. *Interacting Electrons - Theory and Computational Approaches*.

68. Hohenberg, P. & Kohn, W. Inhomogeneous electron gas. *Phys. Rev. B* **136**, (1964).

69. Burke, K. The ABC of DFT. *QMBook* 104 (2004) doi:10.1017/CBO9781107415324.004.

70. Born, M. & Oppenheimer, R. Zur Quantentheorie der Molekeln. *Ann. Phys.* (1927) doi:10.1002/andp.19273892002.

71. Capelle, K. A bird's-eye view of density-functional theory. (2002) doi:10.1590/S0103-97332006000700035.

72. Kohn, W. & Sham, L. J. Self-consistent equations including exchange and correlation effects. *Phys. Rev.* **140**, (1965).

73. Ito, A. M., Takayama, A., Oda, Y. & Nakamura, H. The First principle calculation of bulk modulus and Young's modulus for amorphous carbon material. *J. Phys. Conf. Ser.* **518**, (2014).

74. Joseph, E. & Amouyal, Y. Towards a predictive route for selection of doping elements for the thermoelectric compound PbTe from first-principles. *J. Appl. Phys.* **117**, (2015).

75. Joseph, E. & Amouyal, Y. Enhancing Thermoelectric Performance of PbTe-Based Compounds by Substituting Elements: A First Principles Study. *J. Electron. Mater.* **44**, 1460–1468 (2015).

76. Amram, D., Amouyal, Y. & Rabkin, E. Encapsulation by segregation - A multifaceted approach to gold segregation in iron particles on sapphire. *Acta Mater.* **102**, 342–351 (2016).

77. Sun, C. Q., Pan, L. K., Li, C. M. & Li, S. Size-induced acoustic hardening and optic softening of phonons in InP, CeO2, SnO2, CdS, Ag, and Si nanostructures. *Phys. Rev. B - Condens. Matter Mater. Phys.* **72**, 1–7 (2005).

78. Andrew, R. C. First principles studies of Si-C alloys. (2013).

79. Sjögren, C. IR spectroscopy for vibrational modes A semi-classical approach based on classical electrodynamics and modern quantum mechanics. (2018).

80. Tao, J., Perdew, J. P., Staroverov, V. N. & Scuseria, G. E. Climbing the density functional ladder: Nonempirical meta–generalized gradient approximation designed for molecules and solids. *Phys. Rev. Lett.* **91**, 3–6 (2003).

81. Evarestov, R. A. *Quantum Chemistry of Solids*. *Solid State Sciences* vol. 18 (2007).

82. Rappoport, D., Crawford, N. R. M., Furche, F. & Burke, K. Approximate Density Functionals: Which Should I Choose? *Encycl. Inorg. Chem.* (2009) doi:10.1002/0470862106.ia615.

83. Perdew, J. *et al.* <title>Restoring the Density-Gradient Expansion for Exchange in Solids and Surfaces</title>. *Phys. Rev. Lett.* **100**, 136406 (2008).

84. Rappoport, D., Crawford, N. R. M., Furche, F., Burke, K. & Wiley, C. Which functional should I choose? *Comput. Inorg. Bioinorg. Chem.* 159–172 (2009) doi:10.1002/0470862106.ia615.

85. Csonka, G. I. *et al.* Assessing the performance of recent density functionals for bulk solids. *Phys. Rev. B - Condens. Matter Mater. Phys.* **79**, 1–14 (2009).

86. Fu, C. L. & Ho, K. M. First-principles calculation of the equilibrium ground-state properties of transition metals: Applications to Nb and Mo. *Phys. Rev. B* **28**, 5480–5486 (1983).

87. Werner, F. G. *The foundations of quantum mechanics*. *Physics Today* vol. 17 (1964).

88. Methfessel, M. & Paxton, A. T. High-precision sampling for Brillouin-zone integration in metals. *Phys. Rev. B* **40**, 3616–3621 (1989).

89. Lee, J. G. *Computational materials science : an introduction*. *Theoretical and Computational Chemistry* vol. 15 (2004).

90. Goyal, A., Gorai, P., Toberer, E. S. & Stevanović, V. First-principles calculation of intrinsic defect chemistry and self-doping in PbTe. *npj Comput. Mater.* **3**, 1–9 (2017).

91. Kresse, G. & Furthmüller, J. Efficient iterative schemes for *ab initio* total-energy calculations using a plane-wave basis set. *Phys. Rev. B* **54**, 11169–11186 (1996).

92. Giannozzi, P. *et al.* QUANTUM ESPRESSO: A modular and open-source software project for quantum simulations of materials. *J. Phys. Condens. Matter* **21**, (2009).

93. Gonze, X. *et al.* A brief introduction to the ABINIT software package. *Zeitschrift fur Krist.* **220**, 558–562 (2005).

94. Lehtovaara, L. & Thygesen, K. S. GPAW 2016 : Users and developers meeting. (2016).

95. Aprà, E. *et al.* NWChem for materials science. *Comput. Mater. Sci.* **28**, 209–221 (2003).

96. Guest, M. F. *et al.* The GAMESS-UK electronic structure package: Algorithms, developments and applications. *Mol. Phys.* **103**, 719–747 (2005).

97. Gordon, M. S. & Schmidt, M. W. Advances in electronic structure theory:

GAMESS a decade later. *Theory Appl. Comput. Chem.* 1167–1189 (2005) doi:10.1016/B978-044451719-7/50084-6.

98. Wald, F. Constitutional investigations in the silver-lead-tellurium system. *J. Less-Common Met.* **13**, 579–590 (1967).
99. Brooks, L. S. The Vapor Pressures of Tellurium and Selenium. *J. Am. Chem. Soc.* **74**, 227–229 (1952).
100. Quick Theta/2-Theta Scan (Bragg-Brentano focusing) D/teX Package Measurement General (Bragg-Brentano focusing) D/teX Package Measurement.
101. Toby, B. H. & Von Dreele, R. B. GSAS-II : the genesis of a modern open-source all purpose crystallography software package . *J. Appl. Crystallogr.* **46**, 544–549 (2013).
102. Toby, B. H. R factors in Rietveld analysis: How good is good enough? *Powder Diffr.* **21**, 67–70 (2008).
103. ASTM. ASTM C373-14 Standard Test Method for Water Absorption, Bulk Density, Apparent Porosity, and Apparent Specific Gravity of Fired Whiteware Products. *Astm C373-88* (1999) doi:10.1520/C0373-88R06.much.
104. Diffusivity, T. & Conductivity, T. Laser Flash Apparatus LFA 457.
105. Parker, W. J., Jenkins, R. J., Butler, C. P. & Abbott, G. L. Flash method of determining thermal diffusivity, heat capacity, and thermal conductivity. *J. Appl. Phys.* **32**, 1679–1684 (1961).
106. Wimmer, E. *et al.* Computational materials engineering: Recent applications of VASP in the MedeAï¿½ software environment. *J. Korean Ceram. Soc.* **53**, 263–272 (2016).
107. Xiong, K. *et al.* Behaviour of group IIIA impurities in PbTe: Implications to improve thermoelectric efficiency. *J. Phys. D. Appl. Phys.* **43**, (2010).
108. Ahmad, S., Mahanti, S. D., Hoang, K. & Kanatzidis, M. G. *Ab initio* studies of the electronic structure of defects in PbTe. *Phys. Rev. B* **74**, 155205 (2006).
109. Hoang, K. & Mahanti, S. D. Electronic structure of Ga-, In-, and Tl-doped PbTe: A supercell study of the impurity bands. *Phys. Rev. B - Condens. Matter Mater. Phys.* **78**, 1–8 (2008).
110. Peng, H., Song, J.-H., Kanatzidis, M. G. & Freeman, A. J. Electronic structure

and transport properties of doped PbSe. *Phys. Rev. B* **84**, 125207 (2011).

111. Albanesi, E., Okoye, C., Rodriguez, C., Peltzer y Blanca, E. & Petukhov, a. Electronic structure, structural properties, and dielectric functions of IV-VI semiconductors: PbSe and PbTe. *Phys. Rev. B* **61**, 16589–16595 (2000).
112. Kresse, G. & Joubert, D. From ultrasoft pseudopotentials to the projector augmented-wave method. *Phys. Rev. B* **59**, 1758–1775 (1999).
113. Ahuja, B. L. *et al.* Electronic properties and momentum densities of tin chalcogenides: Validation of PBEsol exchange-correlation potential. *Phys. B Condens. Matter* **465**, 21–28 (2015).
114. Khan, A. A., Khan, I., Ahmad, I. & Ali, Z. Thermoelectric studies of IV-VI semiconductors for renewable energy resources. *Mater. Sci. Semicond. Process.* **48**, 85–94 (2016).
115. Kozliak, E. & Lambert, F. L. Residual entropy, the third law and latent heat. *Entropy* **10**, 274–284 (2008).
116. Brebrick, R. F. & Allgaier, R. S. Composition limits of stability of PbTe. *J. Chem. Phys.* **32**, 1826–1831 (1960).
117. Becke, A. D. & Edgecombe, K. E. A simple measure of electron localization in atomic and molecular systems. *J. Chem. Phys.* **92**, 5397–5403 (1990).
118. Savin, A., Jepsen, O., Flad, J., Ole Krogh Andersen, H. P. & Schnering, H. G. von. Electron Localization in Solid-state Structures: the Diamond Structure. **31**, 187–188 (1992).
119. Amouyal, Y., Mao, Z. & Seidman, D. N. Effects of tantalum on the partitioning of tungsten between the γ- And γ′-phases in nickel-based superalloys: Linking experimental and computational approaches. *Acta Mater.* **58**, 5898–5911 (2010).
120. Lee, M. H. & Rhyee, J. Thermoelectric properties of p-type PbTe / Ag2Te bulk composites by extrinsic phase mixing Thermoelectric properties of p -type PbTe / Ag 2 Te bulk composites by extrinsic phase mixing. **127223**, (2016).
121. Ubelis, A. P. Temperature dependence of the saturated vapor pressure of tellurium. *J. Eng. Phys.* **42**, 309–315 (1982).
122. Becke, A. D. A multicenter numerical integration scheme for polyatomic molecules. *J. Chem. Phys.* **88**, 2547–2553 (1988).

123. Lee, C. & Sosa, C. Local density component of the Lee-Yang-Parr correlation energy functional. *J. Chem. Phys.* **100**, 9018–9024 (1994).

124. Perdew, J. P., Burke, K. & Ernzerhof, M. Generalized Gradient Approximation Made Simple. *Phys. Rev. Lett.* **77**, 3865–3868 (1996).

125. Hammer, B., Hansen, L. & Nørskov, J. Improved adsorption energetics within density-functional theory using revised Perdew-Burke-Ernzerhof functionals. *Physical Review B* vol. 59 7413–7421 (1999).

126. Mattsson, A. E. & Armiento, R. Implementing and testing the AM05 spin density functional. *Phys. Rev. B - Condens. Matter Mater. Phys.* **79**, 1–13 (2009).

127. Sharma, S. & Pandey, S. K. A first principle study of electronic band structures and effective mass tensors of thermoelectric materials: PbTe, Mg2Si, FeGa3 and CoSb3. *Comput. Mater. Sci.* **85**, 340–346 (2014).

128. Zhu, H., Sun, W., Armiento, R., Lazic, P. & Ceder, G. Band structure engineering through orbital interaction for enhanced thermoelectric power factor. *Appl. Phys. Lett.* **104**, 1–5 (2014).

129. Ding, G., Li, J. & Gao, G. Band structure engineering of multiple band degeneracy for enhanced thermoelectric power factors in MTe and MSe (M = Pb, Sn, Ge). *RSC Adv.* **5**, 91974–91978 (2015).

130. Hummer, K., Grüneis, A. & Kresse, G. Structural and electronic properties of lead chalcogenides from first principles. *Phys. Rev. B* **75**, 195211 (2007).

131. Perdew, J. P. Density functional theory and the band gap problem. *Int. J. Quantum Chem.* **28**, 497–523 (1985).

132. Sharma, S. & Pandey, S. K. A first principle study of electronic band structures and effective mass tensors of thermoelectric materials: PbTe, Mg2Si, FeGa3 and CoSb3. *Comput. Mater. Sci.* **85**, 340–346 (2014).

133. Chen, X., Parker, D. & Singh, D. J. Importance of non-parabolic band effects in the thermoelectric properties of semiconductors. *Sci. Rep.* **3**, 2–7 (2013).

134. Lin, J. C., Sharma, R. C. & Chang, Y. A. The Pb-Se (lead-selenium) system. *J. Phase Equilibria* **17**, 253–260 (1996).

135. Nozato, R. & IGAKI, K. On the Equilibrium Diagram of the Lead-Selenium System (I). 125–133 (1955).

136. Bouad, N., Marin-Ayral, R. M. & Tédenac, J. C. Mechanical alloying and sintering of lead telluride. *J. Alloys Compd.* **297**, 312–318 (2000).

137. Liu, Y., Liu, C. yan, Rong, Q. hui & Zhang, Z. Characteristics of the silver-doped TiO2nanoparticles. *Appl. Surf. Sci.* **220**, 7–11 (2003).

138. Amouyal, Y., Divinski, S. V., Estrin, Y. & Rabkin, E. Short-circuit diffusion in an ultrafine-grained copper-zirconium alloy produced by equal channel angular pressing. *Acta Mater.* **55**, 5968–5979 (2007).

139. Amouyal, Y., Divinski, S. V., Klinger, L. & Rabkin, E. Grain boundary diffusion and recrystallization in ultrafine grain copper produced by equal channel angular pressing. *Acta Mater.* **56**, 5500–5513 (2008).

140. Boyd, J. D. & Nicholson, R. B. The coarsening behaviour of θ″ and θ′ precipitates in two Al-Cu alloys. *Acta Metall.* **19**, 1379–1391 (1971).

141. Baldan, A. Progress in Ostwald ripening theories and their applications to the γ′-precipitates in nickel-base superalloys Part II: Nickel-base superalloys. *J. Mater. Sci.* **37**, 2379–2405 (2002).

Appendix I A Matlab code for calculation of the diffusion coefficients

```
function [QQHTST_Ag_PbTe, HTST_Ag_PbTe, figure_Ag_PbTe] =
DiffCo_Ag_PbTe() %function diffinition line

                                                        %Ag PbTe data
clear

                                                        %Variables for
calculations
QwithoutSOC = 57.43*10^3;       %J/mole
QwithSOC = 52.891*10^3;           %J/mole
d = 3.21985E-08;                  % the jump length of the atom in
[cm]
R = 8.314;                      % gas constant -  [J/molK]
h=6.626*10^(-34);               % plank's const (m^2kg/s)
kB = 1.38*10^(-23);             % [(m^2 kg)/(s^2 K)]
uper = []; downer = [];
Tm = 1190;                      % temperature of melting in Kelvin

C0Te = 0.3333;
CbetaTe = 0.5;
C0 = 0.04;                      % the real concentration of Ag at
the matrix -  the average mole fraction of solute in thematrix
[mol/m3]
Calpha = 0;                     % equilibrium Ag concentration at
the matrix
Cbeta = 0.5;                    % equilibrium Ag concentration at
the precipitates
gamma = 0.2;                    % the Surface energy [J/m^2] from
Assaf Hadad, for Ag surface termination,
                                % for Te surface termination they
                                % obttained gamma = 0.9 [J/m^2],
for
                                % the orientetion
(100)(010)PbTe||(100)(010)Ag2Te
```

```
Omega = (6.0221*10^23)*(823.73*10^(-30))/16;  % Omega = NA*Vcall/Z
is   the   molar   volume   of   the   precipitate(m3/mol) (the mean
atomic (or molar) volume of the particle) from JCPDS - 04-014-6681
Temp380 = 380+273;                % In Kelvin
R = 8.3144598;                    % [J/Kmol]
D380C_withoutSOC = (2.32836223356355E-10)*0.0001;   % diffusion
coefficient for 380C without SOC [m^2/s]
D380C_withSOC = (5.39264780369667E-10)*0.0001;             %
diffusion coefficient for 380C with SOC [m^2/s]
R0 =100*10^(-9) ;                 % precipitate radius at t=0  at m

%import frequencies-----------------------------------------------
-------
freqFileS1 = importdata('C:\Users\Meir Haim Dahan\OneDrive -
Technion\Magister degree\jobs\job 13 DFT Pre_Exponential
Coefficients\freqeuncies_Files\interstitial Ag
PbTe\6x6x6\freq_file_6x6x6_step1','r');
freqFileS3_5 = importdata('C:\Users\Meir Haim Dahan\OneDrive -
Technion\Magister degree\jobs\job 13 DFT Pre_Exponential
Coefficients\freqeuncies_Files\interstitial Ag
PbTe\6x6x6\freq_file_6x6x6_step3_5','r');



%checking if the files of frequencies are cool---------------------
-------
if (length(freqFileS1)-1)==length(freqFileS3_5)
    %checking if the files of frequencies are cool



    %create temperature vector. we can change the temperature vector
    %following our needs and it won't destroy our calculations

    Tk=[25:5:300, 313, 350:10:600, 648, 650:10:720, 723, 730:10:800,
823, 830:10:920, 923, 930:5:1400 ];
    Tc=Tk-273;        %for celcius
    D0_HTST = (prod(freqFileS1)/prod(freqFileS3_5))*10^12*d^2;
```

```
     %calculate QQ-HTST's Diffusion Coefficients
    for i=1:length(Tk) %for every Temperature
        for f1=1:length(freqFileS1)
             uper(f1) =
2*sinh(((h)*freqFileS1(f1)*10^12)/(2*kB*Tk(i)));
            %we create a vector with cell for every frequency at
this
            %temperature for step 1
        end

        for f2=1:length(freqFileS3_5)
             downer(f2) =
2*sinh(((h)*freqFileS3_5(f2)*10^12)/(2*kB*Tk(i)));
              %we create a vector with cell for every frequency at
this
              %temperature for step 3.5
        end

        %for the temperature Tk(i) we will calculate the D(Tk(i))

        D_QQ_woSOC(i) = (kB*Tk(i)/h)*
(prod(uper)/prod(downer))*exp(-QwithoutSOC/(R*Tk(i)))*d^2;
        D_QQ_SOC(i) = (kB*Tk(i)/h)* (prod(uper)/prod(downer))*exp(-
QwithSOC/(R*Tk(i)))*d^2;

    end

else
    disp('Error with number of frequencies')
end

%definition of 1/T for the graphs
overTk = (1./Tk)*10^3;
overTc = (1./Tc)*10^3;
```

```
%Fitting for QQ-HTST model for the linear ln(D)=ln(D_0)-Q/RT--------
-----



[D_fit_QQ_SOC, D_fit_QQ_SOC_gof] =
fit((1./Tk)',log(D_QQ_SOC)','poly1');
[D_fit_QQ_woSOC , D_fit_QQ_woSOC_gof] =
fit((1./Tk)',log(D_QQ_woSOC)','poly1');




                                % extract the fitting values
calculated
D_fit_QQ_SOC=coeffvalues(D_fit_QQ_SOC);
D_fit_QQ_woSOC=coeffvalues(D_fit_QQ_woSOC);
                                %extract the activation energies
calculated
Q_fit_QQ_SOC=D_fit_QQ_SOC(1)*8.314;
Q_fit_QQ_woSOC=D_fit_QQ_woSOC(1)*8.314;
                                %extract the D0 - pre-exponential
parameter
D_fit_QQ_SOC=exp(D_fit_QQ_SOC(2));
D_fit_QQ_woSOC=exp(D_fit_QQ_woSOC(2));




%a = D_0 , b=-Q/R -> Q=b*8.314/10^3 [kJ/mole]

%Ploting-------------------------------------------------------------
----------------------------------------
% maximum and minimum for plot
overTk_min=10^3/(800+273);    % 800C as at Fedorovich exp
overTk_max=10^3/(400+273);    % 400C as at Fedorovich exp
Dmin = -Inf;
Dmax=Inf;

subplot(2,1,1)
```

```
figure_Ag_PbTe = plot(overTk,D_QQ_woSOC,overTk, D_QQ_SOC)
title('Ag in PbTe - D Vs T')
ylabel('D [cm^2/s]')
xlabel('10^3/T [10^3 K^{-1} ]')
axis( [overTk_min, overTk_max, 0, 1E-4] ) %axis limits
legend('QQ-HTST without SOC', 'QQ-HTST with SOC')



subplot(2,1,2)
semilogy(overTk,D_QQ_woSOC, overTk, D_QQ_SOC)
ylabel('log(D)')
xlabel('10^3/T [ 10^3 K^{-1} ]')
title('Ag in PbTe - logaritmic scale of D  Vs T ')
axis( [overTk_min, overTk_max, 1E-50,  1] ) %axis limits
legend('QQ-HTST without SOC', 'QQ-HTST with SOC')

% Second - T Celsius axis definition
%ax1 = gca;
%ax1.XColor = 'k';
%ax1.YColor = 'k';
%ax1_pos = ax1.Position; %Adding position of the first (overTk) axis
to ax1_pos
%ax2 = axes('Position', ax1_pos, 'XAxisLocation', 'top', 'Color',
'none')

%line(Tc,D_QQ_woSOC, ax2)

%Export tables of contents-----------------------------------------
---------


TitleNames_QQHTST =
{'one_over_T','T','D_QQ_without_SOC','D_QQ_with_SOC'};
%units : 1/K , K, cm^2/s , cm^2,s
QQHTST_Ag_PbTe = table(overTk',Tk',D_QQ_woSOC', D_QQ_SOC' );
TitleNames_HTST = {'D0_HTST','QwithoutSOC','QwithSOC', 'Tm',
'd','D_fit_QQ_SOC', 'Rsquare_fit_QQ_SOC_gof', 'Q_fit_QQ_SOC' ,
'D_fit_QQ_woSOC', 'Rsquare_fit_QQ_woSOC_gof', 'Q_fit_QQ_woSOC'};
```

```
%units cm^2/s, j/mole, j/mole, K, cm, cm^2/s, cm^2/s, cm^2/s, cm^2/s
HTST_Ag_PbTe = table(D0_HTST',QwithoutSOC',QwithSOC', Tm',
d',D_fit_QQ_SOC', D_fit_QQ_SOC_gof', Q_fit_QQ_SOC' ,
D_fit_QQ_woSOC', D_fit_QQ_woSOC_gof', Q_fit_QQ_woSOC');

%changing the Variables for the titles columns of the table
QQHTST_Ag_PbTe.Properties.VariableNames(1,:)=TitleNames_QQHTST(:);
HTST_Ag_PbTe.Properties.VariableNames(1,:)=TitleNames_HTST(:);



%create files of tables for the material

writetable(QQHTST_Ag_PbTe,'DiffusionDataQQ_Ag_PbTe.csv');
writetable(HTST_Ag_PbTe,'DiffusionDataHTST_Ag_PbTe.csv');

t_QQ=-R0^2/(2*D380C_withoutSOC*((C0-Calpha)/(Cbeta-Calpha)))
t_QQ_withSOC=-R0^2/(2*5.15655944684357e-10*((C0-Calpha)/(Cbeta-
Calpha)))



tR3_QQ =
R0^3/((8*gamma*C0*D380C_withoutSOC*Omega)/(9*R*Cbeta*Temp380))
tR3_QQwithSOC =
R0^3/((8*gamma*C0*D380C_withoutSOC*Omega)/(9*R*Cbeta*Temp380))

thours_withoutSOC = tR3_QQ/(60*60)
thours_withSOC = tR3_QQwithSOC/(60*60)

D_Te_380=(2.7*10^(-6))*exp(-(0.75)/((8.6*10^(-5))*(380+273)))*0.0001
% diffusion coefficient of Te in PbTe for 380C  [m^2/s]
tR3_Te = R0^3/((8*gamma*C0Te*D_Te_380*Omega)/(9*R*CbetaTe*Temp380))
thours_Te = tR3_Te/(60*60)
end
```

Appendix II AgTe (Empressite) cif file

```
data_3D\Atomistic
_audit_creation_date                2019-02-24
_audit_creation_method              'Materials Studio'
_symmetry_space_group_name_H-M      'PNMA'
_symmetry_Int_Tables_number         62
_symmetry_cell_setting              orthorhombic
loop_
_symmetry_equiv_pos_as_xyz
  x,y,z
  -x+1/2,-y,z+1/2
  -x,y+1/2,-z
  x+1/2,-y+1/2,-z+1/2
  -x,-y,-z
  x+1/2,y,-z+1/2
  x,-y+1/2,z
  -x+1/2,y+1/2,z+1/2
_cell_length_a                      8.8820
_cell_length_b                      20.1000
_cell_length_c                      4.6140
_cell_angle_alpha                   90.0000
_cell_angle_beta                    90.0000
_cell_angle_gamma                   90.0000
loop_
_atom_site_label
_atom_site_type_symbol
_atom_site_fract_x
_atom_site_fract_y
_atom_site_fract_z
_atom_site_U_iso_or_equiv
_atom_site_adp_type
_atom_site_occupancy
Ag1    Ag    0.75000   0.05130   0.16690   0.00000  Uiso
1.00
Ag2    Ag    0.25000   0.15582   0.74330   0.00000  Uiso
1.00
Ag3    Ag    0.52010   0.06565   0.64990   0.00000  Uiso
1.00
Te4    Te    0.52280   0.15783   0.09990   0.00000  Uiso
1.00
Te5    Te    0.25000   0.26324   0.35100   0.00000  Uiso
1.00
Te6    Te    0.25000   0.03365   0.34170   0.00000  Uiso
1.00
loop_
_geom_bond_atom_site_label_1
_geom_bond_atom_site_label_2
_geom_bond_distance
_geom_bond_site_symmetry_2
_ccdc_geom_bond_type
Ag1    Ag1     3.094   2_655 S
Ag1    Ag1     3.094   2_654 S
```

Ag1	Ag2	2.828	6	S
Ag1	Ag3	3.036	.	S
Ag1	Ag3	2.824	6	S
Ag1	Ag3	3.115	2_654	S
Ag1	Ag3	3.153	1_554	S
Ag1	Te4	2.959	.	S
Ag1	Te6	2.902	5_655	S
Ag1	Te6	2.838	5_656	S
Ag2	Ag1	2.828	6_455	S
Ag2	Ag3	2.774	6_456	S
Ag2	Te4	2.929	1_556	S
Ag2	Te4	2.565	6_455	S
Ag2	Te5	3.242	7_556	S
Ag2	Te5	2.434	7	S
Ag2	Te6	3.076	.	S
Ag3	Ag1	2.824	6_455	S
Ag3	Ag1	3.115	2_655	S
Ag3	Ag3	3.001	5_656	S
Ag3	Ag1	3.153	1_556	S
Ag3	Ag2	2.774	6_556	S
Ag3	Te4	3.142	.	S
Ag3	Te4	2.783	1_556	S
Ag3	Te6	2.862	.	S
Ag3	Te6	3.244	2	S
Ag3	Te6	2.856	5_656	S
Ag3	Te6	3.119	6	S
Ag3	Te6	3.176	6_556	S
Te4	Ag3	2.783	1_554	S
Te4	Ag2	2.929	1_554	S
Te4	Ag2	2.565	6	S
Te4	Te5	2.577	4	S
Te4	Te5	3.119	7	S
Te4	Te5	2.935	6	S
Te5	Te4	2.577	4_455	S
Te5	Te4	3.119	7	S
Te5	Te4	2.935	6_455	S
Te5	Ag2	3.242	7_554	S
Te5	Ag2	2.434	7	S
Te6	Ag3	3.244	2_554	S
Te6	Ag3	2.856	5_656	S
Te6	Ag3	3.119	6_455	S
Te6	Te6	2.674	2_554	S
Te6	Te6	2.674	2	S
Te6	Ag1	2.902	5_655	S
Te6	Ag3	3.176	6_456	S
Te6	Ag1	2.838	5_656	S

תקציר

חומרים תרמואלקטריים מסוגלים להמיר הפרשי טמפרטורה ושטף חום להספק חשמלי, ולהיפך. המחקר בתחום זה התפתח מאוד בשני העשורים האחרונים, ובפרט בנושא שיפור יעילות ההמרה התרמואלקטרית באמצעות יצירה של ננו-מבנים ופאזות משניות. אחד מהיתרונות של חומרים תרמואלקטריים הוא יכולתם להמיר אנרגית חום לאנרגיה חשמלית בצורה נקייה ולא מזהמת. אחת השיטות לשיפור יעילות חומרים כאלה היא גידול פאזות משניות בתוך החומר. פאזות אלה עוזרות בהנחתת מעבר החום בחומר באמצעות פיזור פונונים, ובכך עוזרות בשימור של הפרש הטמפרטורה שבאמצעותו ניתן להפיק חשמל, וכן בהשפעה על מאזן המטען החשמלי החופשי בחומר. חומר נפוץ מאוד להמרת אנרגיה כזו הוא עופרת-טלוריד (PbTe). אלמנט ידוע המסייע בגידול פאזות משניות ב PbTe הוא כסף (Ag), המהוה מרכיב עיקרי ביצירת פאזת ה Ag_2Te.

בקבוצתנו חקרנו במהלך העשור האחרון וריאציות שונות של אילוח עופרת-טלוריד בכסף וזיקון בטמפרטורות שונות, וכן אילוח משולב של כסף וביסמוט. נוכחנו לראות כי גידול הפאזות מתרחש בקצב מהיר, ובחנו דרכים לשלוט במהירות הגידול. במחקרנו זה אנו מיישמים גישה משולבת של שיטות חישוביות וניתוח תיאורטי עם ביצוע ניסויים לחקר הדיפוזיה של כסף בעופרת-טלוריד. מחקר כזה יעזור בשיפור השליטה שלנו בגידול הפאזות הללו, ובכך יכול לסייע בהשגת שיפור משמעותי ביעילות המרת האנרגיה של עופרת-טלוריד.

במחקר זה אנו עקבנו אחרי השינויים במיקרומבנה של עופרת-טלוריד ופאזות עשירות בכסף באמצעות דיפרקציית קרני X (XRD) תחת טיפולים תרמיים ב 380 מ״צ, טמפרטורה שנמצאה אצלנו בקבוצה כתנאי מספיק ויעיל לקידום תהליכי זיקון. כמו כן אנו בוחנים את ההשפעה של טמפרטורה זו על התכונות התרמואלקטריות של עופרת-טלוריד. בנוסף, המוליכות התרמית והחשמלית וכן מקדם Seebeck נמדדו באמצעות ניסויי in-situ תוך שימוש ב Laser flash analysis (LFA) וב- Seebeck Analysis (SBA) . צורת אפיון זו מהוה חידוש ביחס לפרוצדורות המקובלות כיום בתחום.

הכנת דגמים לניסויי ה XRD וה in-situ כללה התכה בואקום, הומוגניזציה בזמן ארוך, וכתישה. האבקה נלקחה למדידות XRD בתנאים שונים. כמו כן, חלק מהאבקות עברו כבישה חמה לצורך הכנת דגמים צפופים – דגמים אלו נלקחו לצורך מדידות הin-situ של הגדלים התרמואלקטריים, ז״א מקדם Seebeck, המוליכות התרמית והמוליכות החשמלית – מהם הצלחנו לחלץ את ההתפתחות של היעילות התרמואקלטרית בזמן.

מצאנו כי ישנם שינויים משמעותיים במאפיינים האלקטרוניים של החומר, בעיקר בשעות הראשונות של הזיקון, שתלויים באופן ניכר באחוזי האילוח של הכסף. מצאנו הנחתה בהולכה התרמית עם זמן הזיקון, אותה ניתן לשייך לקצב נוקליאציה גבוה של מתבדלים עשירים בכסף. כמו כן נראתה הופעה והיעלמות לא צפויה של פאזה עשירה בכסף, אותה הצלחנו לקשר לפאזה

המטא-סטבילית $AgTe_3$. תצפית על ההופעה וההיעלמות של הפאזה $AgTe_3$ עזרה לנו לקבל אינדיקציה והערכה לגבי התפקיד של האילוח בכסף בתהליכים השונים.

בנוסף, שילבנו שיטות חישוביות כדי לחזות את מקדמי הדיפוזיה של כסף בעופרת טלוריד. לשם כך, השתמשנו בתורת פונקציונל הצפיפות DFT (density functional theory) המבוססת על עקרונות ראשוניים, שיושמה על תיאוריית מצב המעבר (Transition state theory). יכולת הניבוי של מקדמי הדיפוזיה בשיטה זו מאפשרת לנו לנטר את קצב ההתפתחות של הפאזות העשירות בכסף. שימוש בתורת פונקציונאל הצפיפות איפשר לנו לבודד ולבחון וריאציות שונות של אילוח כסף בעופרת טלוריד, כגון בדיקת העדיפות האנרגטית לאיכלוס הכסף בעופרת-טלוריד באתרים השונים: חדירה, החלפה של עופרת, או החלפה של טלור במטריצה.

מצאנו כי קיימת עדיפות אנרגטית לאיכלוס כסף באתרי חדירה בעופרת-טלוריד. מקדם הדיפוזיה הקדם-אקספוננציאלי של כסף בעופרת-טלויד דרך אתרי חדירה שחושב הינו $D_0 = 1.08\cdot10^{-5}\ cm^2\cdot s^{-1}$ ואנרגיית האקטיבציה, ז"א האנרגיה הדרושה לאטומים המבצעים דיפוזיה להתגבר על המחסום האנרגטי השריגי לדיפוזיה, שחושבה הינה $52.9\ kJ\cdot mole^{-1}$ תוך התחשבות בצימוד ספין-מסילה (spin-orbit coupling). בהסתמך על גדלים אלה וגדלים נוספים שהתקבלו במחקרים קודמים שנעשו בקבוצה הערכנו זמן אופייני של כ 15 דקות ב- 380 מ"צ, הנדרש למתבדלים להגיע לצפיפות מתבדלים גבוהה מספיק ע"מ להשפיע על תכונות הטרנספורט התרמואלקטריות. לתוצאות אלה השלכות משמעותיות בחיזוי התפקוד של התקנים תרמואלקטריים תחת תנאי עבודה סטנדרטיים ובקביעת תנאי יציבות העבודה שלהם מבחינת כושר המרת האנרגיה.

המחקר נעשה בהנחייתו של פרופ' ח' ירון אמויאל בפקולטה למדע והנדסה של חומרים בטכניון – מכון טכנולוגי לישראל. אני מודה לבית הספר לתארים מתקדמים על שם אירווין וג'ואן ג'ייקובס בטכניון ולפקולטה למדע והנדסה של חומרים בטכניון על התמיכה הנדיבה בהשתלמותי. ברצוני להודות גם למכון לחקר החלל ע"ש אשר ולמכון לננוטכנולוגיה ע"ש ראסל ברי בטכניון על מימון משלים לביצוע המחקר.

מעבר מסה בתרכובות עופרת-טלוריד מסוגסגות בכסף ליישומים תרמואלקטריים

חיבור על מחקר

לשם מילוי חלקי של הדרישות לקבלת התואר מגיסטר למדעים בהנדסת חומרים

מאיר-חיים דהאן

הוגש לסנט הטכניון – מכון טכנולוגי לישראל

איירר, ה'תש"פ חיפה מאי, 2020